Nanostructured catalyst design to improve ultrafine Pt nanoparticle utilization and stability for PEMFCs

by

Mohd Altamash Jauhar

A thesis

presented to the University of Waterloo

in fulfillment of the

thesis requirement for the degree of

Doctor of Philosophy

in

Chemical Engineering

Waterloo, Ontario, Canada, 2020

Examining Committee Membership

The following served on the Examining Committee for this thesis. The decision of the Examining Committee is by majority vote.

External Examiner	Dr. Yang Yang Professor
Supervisor	Dr. Zhongwei Chen Professor
Internal Member	Dr. Eric Croiset Professor
Internal Member	Dr. Ali Elkamel Professor
Internal-external Member	Dr. Vivek Maheshwari Professor

Author's Declaration

This thesis consists of material all of which I authored or co-authored: see Statement of Contributions included in the thesis. This is a true copy of the thesis, including any required final revisions, as accepted by my examiners.

I understand that my thesis may be made electronically available to the public.

Statement of Contributions

The body of this thesis is based upon a combination of published and unpublished works.

Chapter 4 of this thesis is adapted from published work.

Jauhar, A.M.; Hassan, F.M.; Cano, Z.P.; Hoque, M.A.; Chen, Z. Platinum-Palladium Core–Shell Nanoflower Catalyst with Improved Activity and Excellent Durability for the Oxygen Reduction Reaction. Advanced Materials Interfaces 2018, 5, 1701508, DOI: 10.1002/admi.201701508.

Chapter 5 was adapter from submitted paper in Journal of Power Sources.

Space-confined catalyst design toward ultrafine Pt nanoparticles with enhanced oxygen reduction activity and durability Corresponding Author: Zhongwei Chen

Co-Authors: **Altamash M Jauhar**; Zhong Ma; Meiling Xiao; Gaopeng Jiang; Serubbabel Sy; Shuang Li; Aiping Yu; **Submission POWER-D-20-01151.**

Chapter 6 presented last project and manuscript "Sulfur enrichment within carbon nanopore to improve oxygen reduction stability" is ready for submission as it is in this thesis. This project is co-authored by myself, my supervisor Dr Zhongwei Chen, one collaborator Dr Aiping Yu, and three pos-doc Dr Meiling Xiao, Dr Zhong Ma and Dr Gaopeng Jiang.

Hoque, M.A.; Hassan, F.M.; **Jauhar, A.M**.; Jiang, G.; Pritzker, M.D.; Choi, J.; Knights, S.; Ye, S.; Chen, Z. Web-like 3D architecture of Pt nanowires and sulfur-doped CNT with superior electrocatalytic performance. ACS Sustainable Chemistry & Engineering 2018, 6, 93–98, DOI: 10.1021/acssuschemeng.7b03580.

Kaliyappan, K.; **Jauhar, M.A**.; Y, Lin.; Yu, A.; Bai, Z.; Chen, Z. Constructing a stable 3 V high-energy sodium ion capacitor using environmentally benign Na2FeSiO4 anode and activated carbon cathode. Electrochemical Acta, 2019, 327, 134959-134969, DOI: https://doi.org/10.1016/j.electacta.2019.134959.

Zarshenas, K.; Jiang, G.; Zhang, J.; **Jauhar, M**.; Chen, Z. Atomic scale manipulation of sublayer with functional TiO2 nanofilm toward high-performance reverse osmosis membrane **Desalination**, 2020.

Ren, D.; Ying, J.; Xiao, M.; Deng, Y. P.; Ou, J.; Zhu, J.; Liu, G.; Pei, Y.; Li, S.; **Jauhar, A. M**.; Jin, H.; Wang, S.; Su, D.; Yu, A.; Chen, Z. Hierarchically Porous Multimetal-Based Carbon Nanorod Hybrid as an Efficient Oxygen Catalyst for Rechargeable Zinc–Air Batteries. **Advanced Functional Materials**, 2019, 1908167, DOI: 10.1002/adfm.201908167

Abstract

Polymer electrolyte membrane fuel cells (PEMFCs) is an electrochemical device which efficiently converts chemical energy stored in hydrogen and oxygen into electricity and water. Widely regarded as promising alternative clean and sustainable energy source due zero emission and fast refueling time. Nevertheless, large scale commercialization of PEMFCs is plagued due insufficient long-term stability of precious metal catalyzing oxygen reduction reaction (ORR). The increasing demand of high performance and operationally stable electrocatalyst materials for PEMFCs requires significant research and development in designing and studying new electrocatalysts. Hitherto, Pt is best available material to catalyze ORR, and state-of-art commercial Pt/C cannot meet the crucial targets set by the U.S. Department of Energy (DOE) in terms of activity and stability, and moreover, the excessive use of precious metal platinum is not economically feasible for the widespread application of PEMFCs.

Pt based catalyst suffers dramatic loss in terms of activity and stability due particle agglomeration, Ostwald ripening and dissociations from support material in addition to the loss of precious metal. The technical challenges associated with Pt electrocatalysts need to be addressed by studying and designing new electrocatalysts with advanced technologies. Therefore, development of commercial Pt/C or replacement with novel and more effective electrocatalysts is desirable.

In this thesis two approaches have been investigated for the development of new electrocatalyst material to catalyze ORR in PEMFCs. First study consists of designing sulfur doped graphene (SG) as a unique support material with goal to investigate replacement of carbon support

to reduce carbon corrosion and then deposit Platinum-palladium core-shell structure to improve activity and stability towards ORR. Second study involved the designing and developing new type of electrocatalyst where catalytically active nanoparticle was deposited inside pore of model carbon support material and this study was further extended for the doping of sulfur and Pt deposition inside pore of carbon support.

First study involves synthesis of SG material by Flash heat treatment followed with quenching. Platinum-palladium core-shell structure was deposited on SG support using solvothermal methods. Pt-Pd core-shell structure was interacted with sulfur incorporated in graphene as -C-S-C strengthen the metal support interaction. The core-shell structure exhibits improvement in ECSA and long-term stability of the catalyst due to lower oxidation potential of Pd (0.92 V vs RHE) than Pt (1.19 V vs RHE), therefore prevents active material Pt oxidation. $Pt_{0.9}Pd_{0.1}$/SG exhibits an improved ECSA of 78 $m^2\ g^{-1}$ compared to 65 $m^2\ g^{-1}$ of commercial Pt/C, while mass activity of 0.371 A mg^{-1} (@0.9V vs RHE) compared to 119 A mg^{-1} for Pt/C catalyst. Moreover, after 10K cycles, $Pt_{0.9}Pd_{0.1}$/SG exhibits mass activity of 0.271 A mg^{-1} which is 80 percent of its initial activity, while Pt/C retains only 19 percent of its initial activity.

Due to large size of core-shell structure around 15-20 nm, where Pt as a shell was around 5-10 nm in size, lack of technology to synthesize graphene at large scale, to decrease particle size as to increase active site density and to reduce Pt content, we focused on development of smaller Pt nanoparticle (< 2nm) on commercially available carbon support to improve activity and durability. In second study, we have developed a facile catalyst design to embed ultrafine Pt nanoparticles inside the nanopores of the carbon support towards increased Pt utilization and suppress Pt

agglomeration/Ostwald ripening through pore-confinement effect. The novel strategy endows the resultant Pt nanoparticle with optimized electronic structure, which further accelerates the ORR kinetics and results in excellent activity. Due to these attributes, the as-prepared Pt nanoparticle inside pore (Pt_{inside}/KJ600) catalyst have shown larger ECSA (113.4 m^2 g^{-1}) and initial mass activity of 0.558 A mg^{-1}_{Pt} (@0.9V vs RHE), which is 3.30 times higher than commercial Pt/C and outperforms most of the reported solo Pt catalysts. Beyond that, the catalyst also exhibits significantly improved durability with 9 mV negative shift (0.373 A mg^{-1}) in half-wave potential after 20K cycles, while commercial Pt/C benchmark displays a 52 mV negative shift (0.0619 A mg^{-1}). The structure characterization shows negligible increase in particle size distribution when conducted on the tested catalyst after 20K cycle confirmed that pore-confinement design can effectively inhibit the particle agglomeration.

Higher activity before and after durability test confirmed there was no mass transfer or reaction kinetics limitations due to Pt nanoparticle embedded inside the carbon nanopore, in fact improved stability. In order to further improve activity and stability of the catalyst we further investigated sulfur doping inside pore of KJ600 (S_{in}/KJ600), followed with Pt deposition inside nanopore (Pt@S_{in}/KJ600). First study has proved that sulfur doping improve activity by altering d-band center and improve stability by strengthening metal support interaction. We have first time synthesized and reported synthesis of Pt@S_{in}/KJ600 catalyst where both Sulfur doping and Pt embedded inside pore of carbon support. Pt@S_{in}/KJ600 demonstrated an excellent mass and specific activity of 0.654 A mg^{-1} and 5.26 A m^{-2} compared to Pt/C 0.169 A mg^{-1} and 2.45 A m^{-2} respectively. Moreover, catalyst lost merely 1 mV of half-wave potential compared to 52 mV loss

in Pt/C after 20K cycles. Mass activity of Pt@S_{in}/KJ600 catalyst after 20K cycles was more than 10 times higher than Pt/C catalyst. The structural characterization after durability test also confirmed insignificant changes in catalyst morphology. Spatial pore-confinement and metal-support interaction kept the Pt nanoparticles intact and optimized electronic structure to imparts excellent ORR activity and stability. We believe this catalyst design is not limited to Pt based catalyst but can easily applicable to the synthesis of Pt based alloy (with transition metal) to further improve activity and different catalysis applications.

Acknowledgements

First and foremost, I would like to thank my supervisor, Dr. Zhongwei Chen who gave me an opportunity, provide valuable research and technical knowledge, and for the guidance and support during my PhD work. I also thank the University of Waterloo and the Department of chemical engineering for giving me chance to be part of school and support for doing my graduate work.

I would also like to extend my thanks to my entire PhD examining committee, including Dr. Eric Croiset, Dr. Ali Elkamel, Dr. Vivek Maheshwari and my external examiner Dr. Yang Yang to take time read my thesis and give valuable feedback.

I would also like to thank my present and past group members in the Dr. Z. Chen's Lab for helping me during research, suggestions, feedback on my results, writing and most importantly their friendship and kindness. In particularly, Dr Meiling Xiao, Dr. Gaopeng Jiang, Dr. Zhong Ma, Dr Fathy Hassan helped me greatly in my research work. I would also like to thank Dr Ali Ghorbani, Sahar Hemmati and Kiyoumars Zarshenas for their friendship, constant support and feedback.

I thank the graduate administrative and support at the Department of Chemical Engineering: Judy, Liz, Bert, Ralph and Ravindra for their support and help whenever I needed it.

I would like to express my deepest gratitude to my Parents, Subi, Ayesha, Shakir Bhai, Kamran, Dilshad, Shadab, Akmal, Faizan, Raihan, Aaliya, Ashfaque Karim, Shahzad Karim and

Family members who have always been there for me. Irem, Aayan and Musa to share fun time with me. My beautiful Nanna “Bismillah Fatima” with purest soul to share and cherished one of most beautiful memory I have. My dearest Nana “Afzal Karim” and Dadi “Khairunisha” will always remember you. As I move on to the next chapter of my life, it is comforting to know that, regardless of wherever life takes me, I will always have a loving family to lean on.

And finally, by no means the least, my friends who have helped keep me balanced and sane. I would like to thank Mohamad Shoaib, Shaihroz khan, Omar Bashir Wani, Adil Tariq and Shahrukh Humayun for their constant support and encouragement. I would also like to extend my thank to my friend from AMU, Ibrat, Akhlaq, Atif, Abu Affan, Naushad, ShahKamal, Nausherwan, Tariq and Sarwer for their lifelong friendship.

Dedication

Dedicated to my beloved Parents

Table of Contents

List of Figures

List of Tables

List of Abbreviations

AFC – Alkaline fuel cell

CE – Counter Electrode

DOE – Department of energy

EV – Electric vehicle

FCEV – Fuel cell electric vehicle

GDL – Gas diffusion layer

HOR – Hydrogen oxidation reaction

ICEV – Internal combustion engine vehicle

MCFC – Molten carbonate fuel cell

ORR – Oxygen reduction reaction

PEMFCs – Polymer electrolyte membrane fuel cells

PTFE - Polytetrafluoroethylene

RE – Reference electrode

SOFC – Solid oxide fuel cell

SEM – Scanning electron microscopy

WE – Working electrode

XPS – X-ray photoelectron spectroscopy

XRD – X-ray diffraction

Chapter 1: Introduction

1.1 Motivation and Challenges

Increasing energy demand, depleting fossil fuels and deteriorating environmental conditions due to use of fossil fuels have propelled the research and development towards sustainable clean energy technologies.[1–3] This has led to the development of alternative clean energy technologies instead of nonrenewable energy sources. Hydrogen is a highly efficient, clean energy source with potential to replace or reduce dependence on hydrocarbon fuel sources.[3,4] Hydrogen can be produced from both non-renewable feed stocks and renewable energy sources such as wind, solar, hydro and biomass. For example, hydrogen produced by electrolysis of water using electricity generated from renewable sources of energy is free from carbon dioxide or any impurities. Due to these advantages, hydrogen has potential in development of clean and sustainable energy technology Fuel cells.[4,5]

Polymer electrolyte membrane fuel cell (PEMFC) is a type of fuel cell which efficiently converts chemical energy stored in the reactants (generally hydrogen and oxygen) into electrical energy. PEMFCs uses hydrogen as a fuel, which oxidizes at the anode to form two protons and two electrons, protons are transported across polymer membrane (Nafion) to cathode where they participate in the oxygen reduction reaction (ORR) and form energy and pure water as the only byproducts. PEMFCs due to zero emission, higher energy density and fast refueling time considered promising in area of transportation, portables and even power backups. Hydrogen fueled PEMFCs could cut greenhouse gas (CO_2) emission especially produced by automobiles

sector each year.[6–9] However, other than hydrogen infrastructure, widespread commercialization of PEMFCs is plagued due higher system cost and inadequate durability. According to the U.S. Department of Energy (DOE) guidelines, the cost reduction is being targeted to $40/kW by 2020, and $30/kW as an ultimate cost target.[1] The higher cost of PEMFCs are mostly due to use of precious platinum metal as an active material to catalyze hydrogen oxidation reaction (HOR) and oxygen reduction reaction (ORR) at anode and cathode respectively.[10] Platinum based electrocatalyst comply for the 40 percent of total PEMFCs stack cost.[2,3] In spite of both anode and cathode rely on platinum to catalyze HOR and ORR, majority of platinum is used at cathode due to inherently six order slower reaction rates of ORR compared to HOR.[11,12] Furthermore, reaction kinetics at cathode are negatively affected due to harsh transient potentiodynamic environment, acidic, humidified, oxidative and corrosive environment at high temperature.[13–19] Therefore, to accomplish fuel cell technology roadmap of 5000 hours (which is equivalent of 150000 miles of driving) with less than 10% loss in performance and ever compete with internal combustion engine require extensive development of ORR catalyst technology to (i) lower in Pt loading, (ii) Increase ORR activity and (iii) improved long-term stability in harsh operative conditions.[1]

Till date, platinum is the best available catalyst to catalyze ORR and commercial Pt/C catalysts (2-5 nm Pt nanoparticles dispersed on carbon black support) used in PEMFCs have not met the technical milestone. In addition, Pt based catalyst undergoes physical, chemical and structural degradation due to harsh conditions at PEMFCs operating conditions.[18,20–24] Catalyst degradation are due to active metal nanoparticles dissolution,[17,20,21,24] catalyst particle growth and agglomeration,[21] carbon support corrosion,[16,19,25] potential loss due to contact resistance in

individual component, membrane degradation due to mechanical stress, chemical and contamination in catalyst and membrane.[26,27] It is significant to note that out of seven major factors four of them are associated with the catalyst which negatively affect PEMFCs performance.

Therefore, current electrocatalyst need improvement and deeper insight into new promising materials to accelerates large scale commercialization of PEMFCs. Main objective is to improve activity and stability while reducing Pt loading to be cost effective. Some of the specific targets set for PEMFCs, based on cost and durability at the stack level, set by the US department of Energy (DOE) is shown in Table 1-1 below.

Table 1-1: US Department of energy specified status and targets for PEMFCs.[1]

Characteristics	Units	Targets 2020
Power density	W L^{-1}	850
Specific power	W kg^{-1}	650
Cost	\$ kW^{-1}	30
Durability	hours	5000
Pt group metal total loading	mg cm^{-2}-electrode area	0.125
Mass activity	A mg^{-1} Pt at 0.9 $V_{iR\ free}$	0.44

There is an urge to overcome these challenges for the development of widespread commercialization of PEMFC. Therefore, current electrocatalyst need improvement and deeper insight into some new promising materials and technologies, which is the motivation behind this research.

1.2 Thesis Objectives

The main objective of this thesis is to develop facile catalyst design to improve electrocatalytic activity and durability of ORR in PEMFCs and reduce Pt loading. Pt loading can be decreased by increasing Pt atom (smaller particle size has surface atom ratio) utilization, however, smaller nanoparticles are more susceptible to Sintering (Ostwald ripening, agglomeration and particle migration) and dissociation due to higher surface energy.[28–32] Pt nanoparticles stability is also depends on physiochemical properties of support material and metal-support interactions.[33–35] Graphene as a support material for ORR has gained attention due to excellent physiochemical and electrical properties, corrosion resistance, fast charge transport and high surface area (theoretically 2630 m^2 g^{-1} for a single atomic layer).[35–43] Hydrophobic nature of graphitized surface pose challenges for uniform dispersion and weak metal support interaction led to irreversible agglomeration, results in loss of actives sites and hence induces resistance towards mass transfer and diffusion of reactant molecules. First approach involves synthesis of sulfur doped graphene (SG) to improve metal support interaction and deposit stable Pt-Pd core-shell nanostructure to improve both activity and stability of the catalyst towards ORR. Core-shell structure realized to reduce Pt loading, while addition Pd acts as sacrificial element due to low reduction potential between two. Secondly, a new approach involves synthesis of ultrafine Pt nanoparticles inside

carbon support nanopores to increase number active sites due to large ECSA and optimized electronic configuration. Pt nanoparticles growth inside nanopore can effectively control particles size and uniform particle size distribution, while it can inherently reduce particle migration, agglomeration by restricting spatial movement due to pore-confinement effect.[44–51] For this work, commercial carbon support (KJ600) was selected due to high conductivity, large surface area, and higher porosity with interconnected pore network to accommodate high density of active sites. This project will be extended to heteroatom doping inside carbon support to further improve catalyst activity and durability. The main objective of this thesis includes.

(a) Design and synthesis of unique sulfur doped graphene (SG) materials to support core-shell Pt-Pd nanostructure (PtPd/SG) to improve activity and stability of ORR.

(b) Evaluate pore-confinement effect on ultrafine Pt nanoparticle to reduce agglomeration and dissolution and investigate impact on ORR activity and performance.

(c) Develop and investigate unique strategy to dope sulfur inside nanopore of carbon support to improve metal-support interaction inside pore to further strengthen catalyst stability.

1.3 Thesis Outline

As thesis progress, **Chapter 1** consist of introduction laying foundation for overall thesis work. It includes background information and challenges associated with development of PEMFCs with project objectives to address those challenges. **Chapter 2** consist of detailed research background, principle and working, challenges associated with performance loss, Catalyst limitations and likely technology development to overcome those limitations. **Chapter 3** of this thesis will elaborate on

all the major synthesis methods, physiochemical and electrochemical characterization used for the study and development of Pt based ORR catalyst. **Chapter 4** highlights the development of PtPd core-shell structure on SG (PtPd/SG) to improve ORR activity and stability. Physiochemical and electrochemical property of the catalyst was thoroughly investigated. **Chapter 5** focused on the development of facile catalyst synthesis to deposit ultrafine Pt nanoparticle inside carbon support nanopore (Pt_{inside}/KJ600). Synthesized catalyst was compared to catalyst where Pt was deposited on the carbon surface with similar methods and commercial Pt/C. Thorough study was performed to elucidate confined nanoparticles effects on the ORR performance and stability of Pt nanoparticles in long-term stability test. **Chapter 6** derived from the results of chapter 4 and 5, where sulfur doping improved metal support interaction. In this project, sulfur was doped inside pore of KJ600 (S_{in}/KJ600), followed with Pt deposition inside doped carbon support (Pt@S_{in}/KJ600). This is the first study where both doping, and catalyst nanoparticle deposition was done inside pore of carbon support to improve ORR activity and stability for PEMFCs application. Finally, **Chapter 7** includes summary and conclusions of all the results reported in this thesis. This chapter final section directs recommendations for future projects which can be done for the further development of these catalyst in PEMFCs application.

Chapter 2: Literature Review

2.1 History of Fuel Cell

Fuel cells converts chemical energy stored in reactants into electrical energy through electrochemical energy conversion. The fuel cell concept had been effectively demonstrated in the early nineteenth century by Humphry Davy as ‘gas battery’ and was followed by pioneering work of scientist Christian Friedrich Schönbein in 1838, which later were to become fuel cells. In 1839, William Grove, a chemist, physicist and a lawyer were credited for the invention of fuel cell. Grove demonstrated that electric current can be produced by placing two platinum strips in separate bottles containing hydrogen and oxygen in the presence of sulfuric acid. The term “Fuel Cell” was first used by Charles Langer in 1889 and with Ludwig Mond they constructed first practical fuel cell device using industrial coal gas as the fuel and air as oxidant. However, due to poor understanding of their principles, unreliable fuel sources, and expensive catalysts their practical implementation was a challenge. In 1932, Cambridge engineering professor Francis Bacon modified Mond's and Langer's model to develop the first alkaline fuel cell (AFC). Bacon demonstrated a practical 5 kW fuel cell system in 1959. NASA in collaboration with General Electric (GE) start designing fuel cell generators for manned space missions, which was later used for Gemini and Apollo space project in late 1950-60s. After this, many companies had researched and started developing interest in this technology; however, most recently PEMFCs for sustainable and clean energy production has drawn dramatic attention as a replacement for fossil fuels.

2.2 Types of fuel cells and their application

Fuel cells are classified based on electrolyte used in their system. The different types of fuel cells are as follows: (i) Polymer electrolyte membrane fuel cell (PEMFC), (ii) Phosphoric acid fuel cell (PAFC), (iii) Alkaline fuel cell (AFC), (iv) Molten carbonate fuel cell (MCFC), and (v) Solid oxide fuel cell (SOFC). Fuel cells and their intrinsic property are presented in following Table 2-1.

Table 2-1: Different type of fuel cell property

Characteristics	PEMFC	PAFC	AFC	MCFC	SOFC
Temperature class	Low Temperature (LT)			High Temperature (HT)	
Charge carrier	H^+	H^+	OH^-	CO_3^{2-}	O^{2-}
Operating temperature	80 ºC	200 ºC	60-220 ºC	650 ºC	600-1000 ºC
Catalysts	Platinum	Platinum	Platinum	Nickel	Perovskites (ceramics)
Cell components	Carbon based	Carbon based	Carbon based	Stainless based	Ceramic based
Electrolyte	Polymer membrane	Liquid H_3PO_4	Liquid KOH	Molten carbonate	Ceramics
Fuel compatibility	H_2, Methanol	H_2	H_2	H_2, CH_4	H_2, CH_4, CO
Applications	Electric utility,	Electric utility,	Military,	Electric	Electric

	portable power, transportation	transportation	space	utility	utility, auxiliary power

2.3 Polymer electrolyte membrane Fuel cell (PEMFC)

2.3.1 Operations Principles

PEMFCs are a type of low temperature fuel cell, consisting of two electrodes (an anode and cathode) separated by an electrolyte. In PEMFCs, hydrogen gas (H_2) oxidation takes place at the anode (Hydrogen oxidation reaction, HOR) and produces H^+ ion and an electron. Polymer membrane only allow the transport of hydrogen ions (protons) from anode to cathode. Electron transport take place through external circuit and together with protons reacts with oxygen and allow oxygen reduction reaction at cathode to produce water and energy. The schematic diagram in **Figure 2-1** shows the basic fuel cell components and operation. The polymer membrane used in PEMFCs are ionomers of thickness around 20 μm and plays a critical role in achieving high power density. The polymer membrane is impermeable to the electron flow. The operating temperature of PEMFCs has a major effect on durability of polymer membranes due to thermal degradation at high temperature. Most common membrane, Nafion, can sustain temperature below 100 ºC and is made up of perfluorinated sulfonic acid (PFSA) with an excellent proton transport characteristic. PEMFCs are the most common type of fuel cell due to their high energy density, low operating temperature, quick start-up time, and rapid response to varying loads. These

properties make PEMFCs most popular for manufacturers and can be used in wide range of stationary, portable and transport applications.

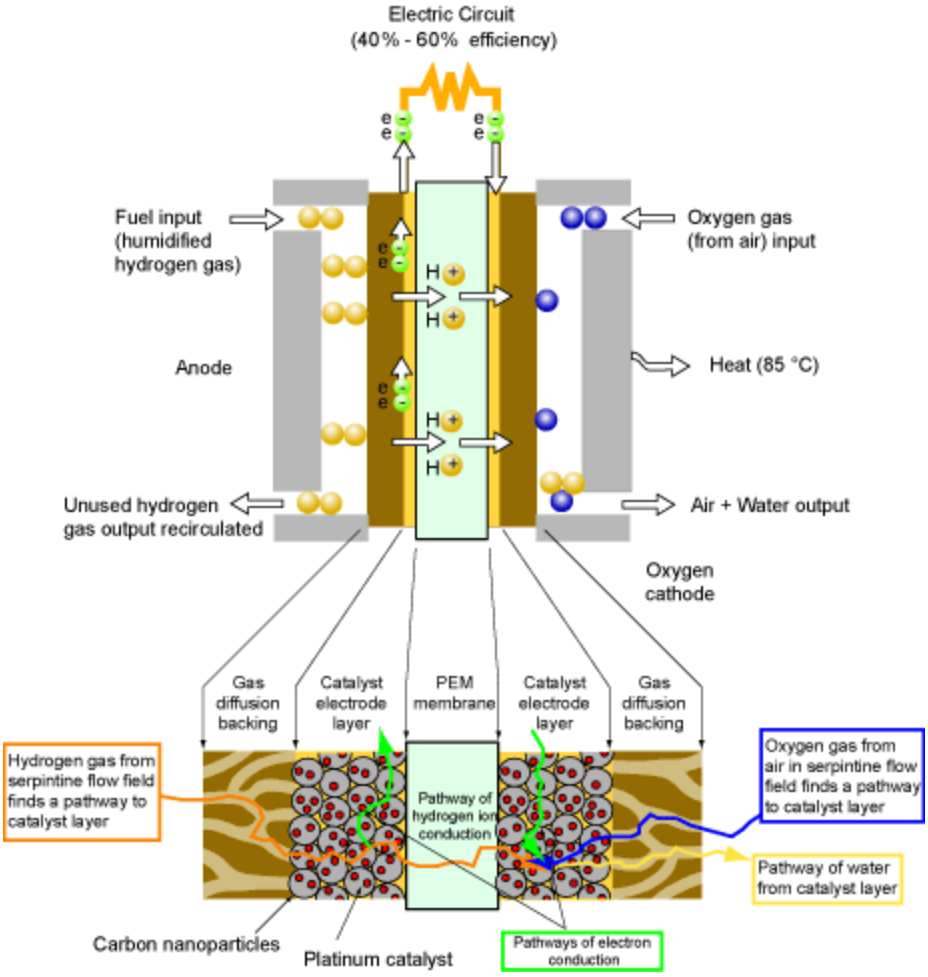

Figure 2-1: Schematic diagram of PEM Fuel cell.[52]

The reactions involved in a PEMFC are as follows:

Anode:	$H_2 \rightarrow 2H^+ + 2e^-$	$E^\circ = 0$ V vs RHE
Anode:	$\frac{1}{2} O_2 + 2H^+ + 2e^- \rightarrow H_2O$	$E^\circ = 1.229$ V vs RHE
Overall reaction	$H_2 + \frac{1}{2} O_2 \rightarrow H_2O$	$E^\circ = 1.229$ V vs RHE

Despite of boasting theoretical open circuit voltage of 1.229 V, voltage observed during real PEMFC operation are significantly lower than theoretical value. This can be attributed to overpotential and irreversible voltage losses. In general, most of the potential loss is due to slow ORR kinetics at cathode. The HOR reaction at anode are inherently faster due to comparatively higher exchange current density (0.1 A cm^{-2}) and cause a minor loss (< 10 mV) of voltage. However, the exchange current density due to ORR is extremely low (6 μA cm^{-2}) and responsible for a significant activation loss of ~300 mV. **Figure 2-2** presents a typical polarization curve showing the different losses in PEMFCs. As shown in **Figure 2-2**, the losses in the PEMFC performance can be divided into four major regions with increasing operating current: (i) mixed-potential losses, (ii) activation loss primarily due to cathode reaction kinetics, (ii) ohmic resistance and (iv) mass transport limitations.

Mixed potential losses: The first thing to notice is open-circuit voltage is lower than theoretical value of 1.229 V vs RHE at 80 ºC. These mixed potential losses are related to fuel cross over across the membrane, short circuiting and oxidation of the catalyst materials at cathode.[8] Possibility of secondary reactions at the cathode can also be responsible for lower OCV value, including: (i) cathodic oxidation due to any permeability of PEM electrolyte to H_2 gas. Hydrogen gas crossover to the cathode and oxidize due to high potential and can decrease cell potential by ~25-30 mV.[17,53,54] (ii) Reversible adsorption of the oxygen species at the surface of Pt catalyst at the cathode can form Pt/PtO and reduces about 90-190 mV.

Activation loss: This is due to activation overpotential and are due to limitation of electrochemical reactions kinetics of the electrodes. Sluggish ORR kinetics are mostly responsible for majority of

voltage losses. The exchange current density of ORR is only 0.5 to 1.5 mA cm^{-2} compared to HOR (3-10 mA cm^{-2}), as a result can exhibit a large overpotential in range of ~ 300 mV, even in the presence of most active Pt-based catalyst. As magnitude of exchange current density determines rate of electrochemical reactions, and it depends upon reaction and the electrode surface where it takes place. This is most detrimental loss in PEMFC and thus there is a considerable scope to improve existence nanostructured catalyst to improve exchange current density and reduce voltage losses. This is one of the primary focus of researchers and scientist working in the field of PEMFC.

Ohmic loss: This region displays a linear loss in cell voltage with increase in currents density in the polarization curve. The ohmic loss in PEMFCs are due to bulk electrical resistance of the cell materials, cell concentrations (bipolar plates, catalyst layers, current collector cables etc.) and the resistance to hydrogen ions transport in polymer electrolyte. Appropriate choice of materials and electrode structure with high conductivity can mitigate ohmic losses.

Mass transport limitation: This is associated with mass transport of reactants to the electrode. At high current densities, the voltage of PEMFCs drops dramatically. This is due to fact that reactant consumption rate at electrode are faster than the reactant supplied to the catalyst surface. When reactant supply becomes zero current density reaches the limiting value. Reactant concentration, feed flow rates, cell temperature, structure of the gas diffusion layer and catalyst layers architecture are the primary factors that influence mass transport limitations and determine the limiting current density of a PEMFC.

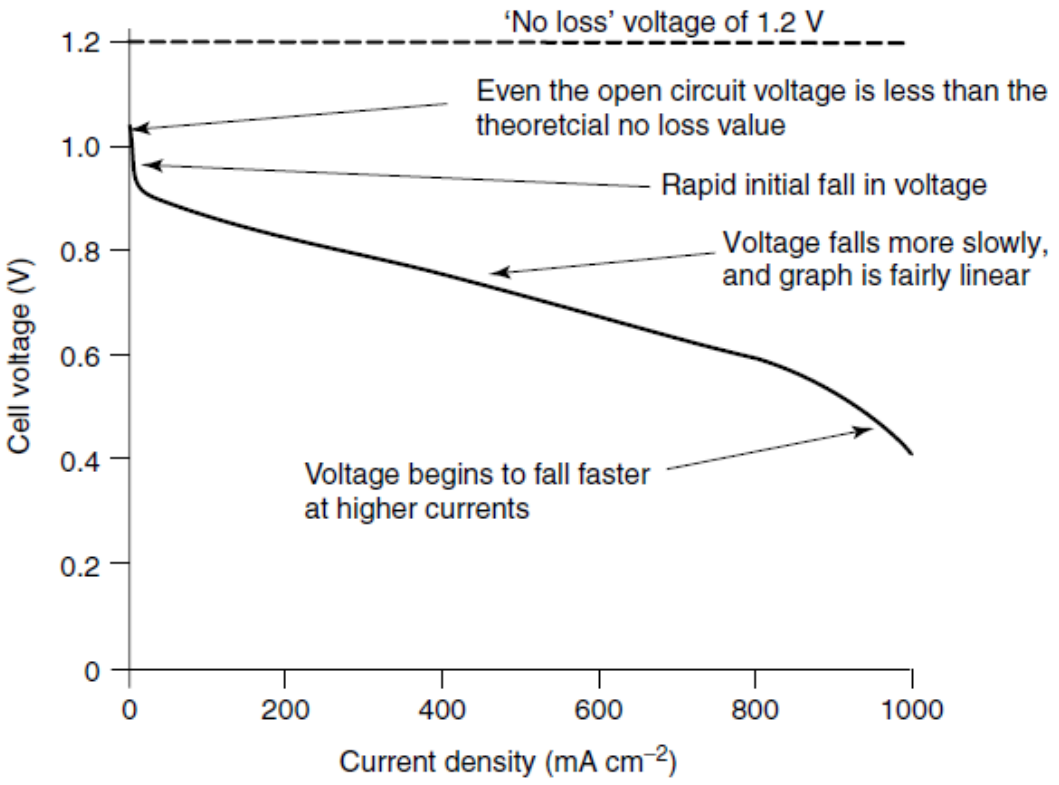

Figure 2-2: A typical PEMFC polarization curve showing different regions of potential losses.[8]

2.4 Catalyst stability limitations

Fuel cell operation exposes the cathode to harsh potentiodynamic conditions which persist during drive cycles, through start up and shut down procedures and during fuel cell starvations. The acidic nature of the polymeric membrane, oxidative, humidified cell condition and elevated temperature create a harsh environment that led to catalyst degradation and loss of fuel cell performance over time.[15,17,19,21,24,55–57] The specific reason for the Pt/C catalyst degradation are (i) carbon corrosion, (ii) platinum nanoparticle dissolution and/or agglomeration, (iii) Sintering (Ostwald ripening, coalescence) and (iv) catalyst contamination and/or poisoning.[16,28–32,58,59]

Carbon support corrosion/oxidation is thermodynamically favored under the normal operating conditions with the standard equilibrium potential of 0.207 V vs RHE.[21]

$$C + H_2O \rightarrow CO_2 + 4H^+ + 4e^-$$

Although high electrode potential of cathode is large enough to drive direct oxidation/ corrosion of carbon support material.[19] Platinum has been found to catalyze the carbon oxidation. Several other factors such as humidity, temperature and amount of carbon also influence carbon corrosion.[14,60] Carbon corrosion is very detrimental towards the long term fuel cell operation and need to be reduced. The most common approach researchers are looking into to mitigate this problem is replacement of traditional carbon with highly graphitized graphene and carbon nanotubes.[42,61–63]

Platinum nanoparticles dissolution and/or aggregation is also very common and play a key role in reducing PEMFCs performance. Due to higher surface energy of smaller size Pt nanoparticle (2-3 nm) migration and agglomeration into large nanoparticle happens due sintering and Ostwald ripening effects. Ostwald ripening follows two major pathways: (i) Pt ion migration through the ionomer layer in the catalyst and (ii) Pt dissolution and subsequent adhere to the adjacent particle. Pt/C catalyst before and after use in PEMFCs have been shown in **Figure 2-3**, which shows a clear evidence of Pt agglomeration before and after 200 hours of operations in 10 cell PEMFC stack. Different technique have been investigated to overcome this deteriorating phenomena such as: (i) designing and development of novel support materials, where Pt nanoparticles can strongly adhere to support and inhibit their dissolution and agglomeration, (ii)

synthesis of more stable nanostructures such as nanowires, alloy and core-shell structures due to reduced surface energy of Pt in these morphologies compared with the nanoparticle form.

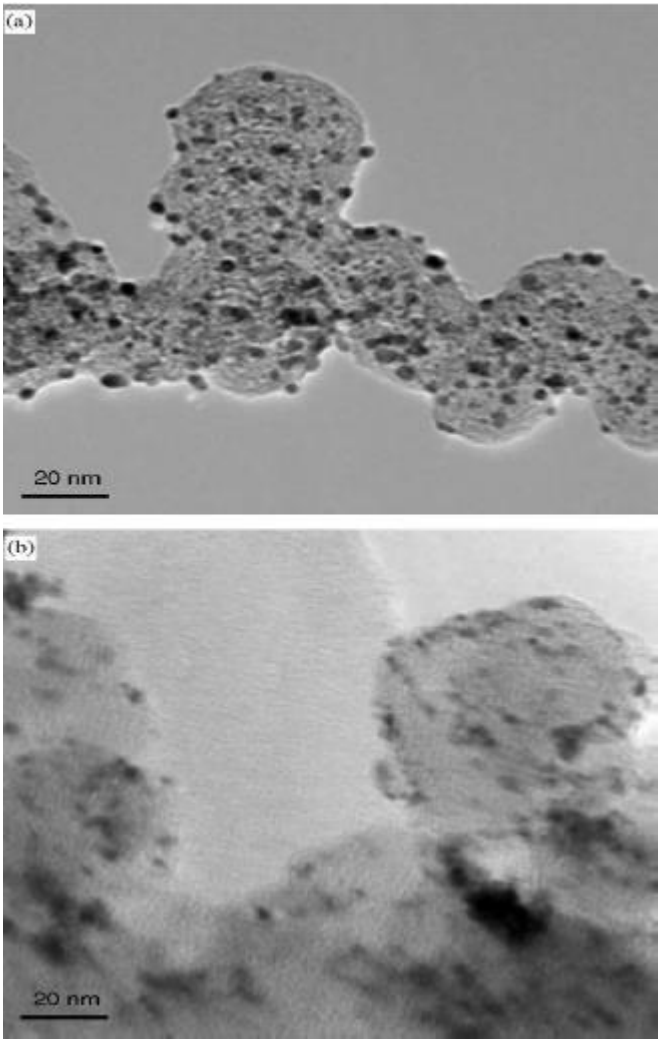

Figure 2-3: TEM micrographs of the (a) original Pt/C catalyst (b) and the degraded catalyst after 200 hours.[64]

2.5 Nanostructure carbon support materials

The main objective of PEMFC development is to improve the performance and durability, and simultaneously reduce the cost. One strategy is to improve carbonaceous support material to

improve performance and durability. It is already established that supported catalysts exhibit superior quality to unsupported catalysts. An ideal support material should possess high electron conductivity, large surface area, high corrosion resistance, tight metal catalyst support interaction, ability to maximize the triple phase boundary, and good water handling capability to avoid flooding.[65] Therefore, the selection of support material plays an important role in determining performance, durability and cost effectiveness of the catalyst. Traditionally, carbon black with high surface area such as Vulcan XC-72R (Cabot corp., 250 m2/g), Shawinigan (Chevron, 80 m2/g), Black pearl 2000 (BP2000, Cabot corp., 1500 m2/g), Ketjen Black (KBEC600JD & Ketjen International, 1270 m2/g and 800 m2/g, respectively) and Denka Black (DB, Denka, 65 m2/g) have been used to support Pt nanoparticles for PEMFC applications. Among these carbon black, especially Vulcan XC-72R are most commonly used material to support Pt and Pt-alloy catalyst in PEMFCs. These are produced from the pyrolysis of hydrocarbons. Carbon black (CB) particles are less than 50 nm, spherical shape and can grow up to 250 nm particle on aggregation. CB consists of several turbostratic layers, with polycrystalline structure and have interplanar spacing of 0.35-0.38 nm. The morphology and particle size distribution of CB can be greatly affected by a variety of thermal decomposition methods and different synthesis materials.[66] In spite of being widely used, CB have several drawbacks: (i) carbon corrosion at high potential, which cause detachment of Pt catalyst from the surface and loss of activity, (ii) the presence of organometallic impurities, (iii) thermochemical instability, (iv) trapping of catalyst nanoparticles in deep pores, leading to inaccessible reactant molecules. Interaction between ionomer and nanoparticle is affected by CB pore size and distribution. As the typical size of Nafion micelles (> 40 nm) is much

larger than CB micropores, many catalyst particles trap in these pores and can be inaccessible to the reactants and lead to loss of expensive metal catalyst as make no contribution in catalyzing electrochemical reaction. Therefore, development of Carbon-Pt system is crucial for the growth of fuel cell applications.

Several other support materials have been investigated over the last few years, and some of them are discussed here. Mesoporous carbon materials are a class of porous materials having high surface area and a pore size of 2-50 nm. Mesoporous carbons are divided into two types; ordered mesoporous carbon (OMC)[67–71], and disordered mesoporous carbon (DOMC) comprised of irregular interconnected structure, and thus lower conductivity and larger pore size than OMC. Mesoporous silica or triblock copolymer templates are used to synthesize OMC.[72] The carbon structure in the support material is responsible for access of reactant to the catalytic active sites and the removal of products. OMC functionalized with oxygen group on their surface improves interaction between the catalyst and support material and allow better catalyst dispersion. Pt nanoparticle supported on OMC such as CMK-3 exhibit higher ORR activity, due to uniform dispersion of nanoparticle which instigate more electrochemically active sites and ECSA.[70] The improvement of ORR activity in CMK-3 can be attributed to highly ordered structure, and 3-D interconnection of the hexagonally arranged carbon nanorods. The 3D morphology, pore volume, pore structure and surface chemistry plays an important role in improving ORR activity.[70] Pt supported CMK-3 have shown promising results for alcohol oxidation in DMGCs.[73] Nanostructure modification, surface functionalization and doping of OMCs can significantly improve electrocatalyst activity, stability and fuel cell cross over.

Graphene is another alternative carbon support material driving great interest to use as support material. Graphene is a flat monolayer with hexagonally arranged carbon atoms tightly packed in a two-dimensional lattice arrangement like a honey comb.[74] Graphene has been researched for fuel cell application due to high electron transfer rate, large surface area and high conductivity.[75] Edge and basal plane of 2D planar carbon sheets create a platform for catalyst nanoparticle interaction. Surface anchoring sites are important for ions interaction, followed by Pt nanoparticle nucleation and subsequent growth. It has been addressed that π electrons dense region can serve as these anchoring sites for metal catalyst.[76] Graphene sheets are rippled in nature and have very high surface area to attach catalyst nanoparticle. Graphene possesses remarkable electron transport that is required for ORR in fuel cell operation[77] and a band gap equal or close to zero.[78] Higher quality graphene is required to catalyze the ORR reaction, and can be synthesized by micromechanical exfoliation, epitaxial growth and CVD. Among various procedures, CVD has distinct advantages over other techniques to obtain highly exfoliated large surface area graphene from graphene oxide. The graphene oxide (GO) can be prepared by modified hummer's method and is used throughout this work.[79] The GO is annealed at high temperature of 800-1000 ºC in the presence of argon gas to produce graphene. The catalytic property of graphene can be further improved by doping with heteroatoms to provide more active sites and to tune their band gaps.[36]

Carbon nanotubes (CNTs) are 1D nanostructures tubes like structure formed by rolled up single sheets of hexagonally arranged carbon atoms. CNTs are commonly classified as a single-walled (SWCNT) or multi-walled (MWCNT), which may be produced from various synthesis routes.[80–85] Based on nanostructure property and application, SWCNT or MWCNT as a support material

can be used in fuel cell catalyst application.[86] MWCNT have a diameter of a few nanometers with the spacing between each wall of 0.34 nm. SWCNT generally possess more surface area than MWCNT, while the latter exceeds in conductivity. CNT are generally chemically inert in nature, which makes it difficult for catalyst nanoparticle to attach on them. This can be avoided by functionalization of the CNT surface. Strong oxidizing agent can be used to add hydrophilic nature to the surface and different oxygen containing functional group, which would eventually elevate catalyst support interaction.[87] The use of CNT as a support material can channelize better catalyst nanoparticle dispersion, control size and morphologies. CNT has very high electron conductivity and corrosion resistant which allow better catalyst activity in fuel cell for long duration than carbon black.[88] CNT can also be doped with heteroatoms to alter and improve intrinsic property for electrocatalytic application.[85,89–92]

2.6 Heteroatom doping in nanostructure carbon material

Strengthening the cohesive interaction between Pt and the support material delays and obstruct the Pt dissolution, migration and agglomeration.[93–100] It has been found that doping strongly increases the interaction (tethering effect) in doped support materials compared to undoped one. Intrinsic properties of carbon materials can also be altered by introduction of heteroatoms. Heteroatoms such as B, P, N and S have been successfully introduced into carbon nanostructured and are effective in modifying the electrical and chemical property of carbon support.[101–105] Recent studies have shown higher catalytic activity, long-term durability and methanol tolerance in nitrogen doped graphene, CNTs and mesoporous graphitic array.[104,106] The improvement in ORR activity can be attributed to development of positive charge density on the adjacent carbon atom

due electronegativity of N (N electronegativity: 3.04) which is favorable for O_2 adsorption. Moreover, carbon material doped with B (2.04) and P (2.19) have also showed improved catalytic activity. Sulfur is the newest addition in the doping of carbon material, but not many researchers have looked into this.[107,108] The Electronegativity of sulfur (2.58) is close to that of carbon (2.55); therefore, introduction of S atoms into the carbon nanostructure stabilizes their structure and improves their electrical property. In addition, formation energy of S doped CNT is 0.7 eV higher than N doped CNT, thus thermodynamically more feasible, and can be increased up to 1 eV in graphene due to substitutional defect.[101] These materials have a positive effect on electrocatalytic activity and heteroatom doping will be extensively studied for novel graphene and carbon (KJ600) support material.

Chapter 3: Experimental methods and characterization techniques

The purpose of this section is to provide general details and fundamental principles of experimental techniques (consisting of synthesis, characterization and electrochemical evaluations) used throughout this thesis.

3.1 Fabrication Techniques:

3.1.1 Chemical vapor deposition

In chemical vapor deposition (CVD), solid material is deposited on the surface of heated substrate material in vapor phase. CVD is used to obtain materials with different properties by changing experimental condition in terms of substrate material, reaction gas mixture ratios, gas flow rate, and precursor ratios. CVD is an excellent technique which enables the material synthesis and treatment at high temperature. High surface area material such as sulfur doped graphene, Nitrogen and sulfur doped inside pore of support material can be synthesized using this technique.

3.2.2 Solvothermal techniques

Solvothermal techniques involves the material synthesis by using an organic solvent for precursors at high temperature and pressure. Size, shape, distribution and crystallinity of nanomaterials can be precisely controlled by varying experimental parameters such as reaction temperature, reaction time, precursors, surfactant and solvents. Precursor solutions are loaded in a Teflon-lined sealed autoclave vessel and fastened tight and securely before placing in an oven at a

desired temperature for a specific time period. Solvothermal techniques are a proven method to synthesize a variety of materials.[109]

3.2 Physiochemical Characterization

3.2.1 Scanning Electron Microscopy & Energy Dispersive X-Ray:

Scanning electron microscopy (SEM) is a powerful imaging technique use to study topography, morphology and anatomical structure of micro and nanomaterials. It is one of the most authentic and used technique to characterize solid materials[110]. Electron microscopy uses high-energy beams of electrons to captures image of sample by scanning surface of samples. Due to smaller wavelength of electron in comparison with light, it can achieve higher magnification and resolution. The spatial image resolution depends on the spot size and electron interaction volume. While performing electron microscopy, samples are placed inside ultra-high vacuum to avoid any deflection of the electrons beam. Electrons beam collides with sample atoms and produce different types of signals based on collison including: secondary electron, back scattered electron, characteristics x-rays and electron beam induced current (EBIC)[111]. These splitting of electrons happens due to deviations of energy between incident and reflected electron energy. All these reflective beams give some form of useful information; secondary electron (topology and morphology of sample), back scattered electron and characteristic x-rays (elemental composition) while EBIC gives electrical characteristic of semiconductor. In this thesis, SEM was used used to study morphology and structure of synthesized catalyst. To perform microscopy, the sample was prepared by spreading powder/material on carbon tape that is fixed on a sample holder stub. This

stub is placed inside the SEM chamber, followed by evacuation of sample chamber and subsequently imaging was performed.

3.2.2 Transmission electron microscopy

Transmission electron microscopy (TEM) is one of the most powerful imaging tools available today. TEM can produce high resolution images up to nanometer or atomic scale level. Samples are illuminated with high energy electron beam (200 to 400 kV), which passes through several condensers and is then transmitted through the samples. When the electron collides with the sample, it scatters elastically or in-elastically and gets collected to further analyzed. Based on electron diffraction theory, the signal of diffracted electrons is processed to produce the image. The beams of electrons are transmitted through ultra-thin specimen, magnified and focused by an objective lens.[112] The electrons are produced from tungsten filaments by a thermionic emission process, while are aligned and accelerated as they pass through numerous intermediate and projector lenses.[112] Due to higher resolution than any other technique, TEM is an effective technique in determining nanostructures, atomic arrangements, exposed crystals facets and defects in the materials. The main difference between SEM and TEM is structural difference that can be obtained for materials. In SEM, surface topography and morphology can be obtained, while TEM can deliver underlying inner structures of the material.

3.2.3 Energy dispersive x-ray spectroscopy

Energy dispersive x-ray spectroscopy (EDX) techniques are commonly coupled with TEM and SEM devices and can be performed in parallel with these imaging techniques. EDX technique is based on bombardments of electron onto a material which results in the emission of x-rays and

then collected by a detector. The energy of an emitted x-ray is a characteristic of a certain elements, which allows the identification and quantification of elements present in the samples. EDX can be performed on a localized area or large area of the samples and called elemental mapping. Variations in intensities of the characteristics x-ray from a localized area are used to identify variations and concentrations of different elements. In a typical EDX spectrum, X-ray emissions energy is plotted on the x-axis and intensities on the y-axis.

3.2.4 X-ray diffraction

X-ray diffraction (XRD) is non-destructive characterization technique in material science and engineering to identify materials, their crystal arrangements upon comparison with diffraction pattern databases. In addition, XRD also provide information about composition and grain size. There are several types of XRD techniques, such as single x-ray diffraction, powder diffraction, and high-resolution diffraction. Monochromatic x-rays of known wavelength are generated from a source (Cu in this case) and interact with atoms of the material being characterized. According to Bragg's law, the diffracted x-ray beam from the samples are related to interplanar spacing of the powder and relate to crystal phase of the samples. In this study, XRD diffraction patterns are used to study crystal phase, lattice spacing and average Pt nanoparticle sizes. The average Pt nanoparticle size is calculated through diffraction pattern obtained at Pt (220) diffraction peaks observed at 2-theta value of 67 degree. The Scherrer equation used to calculate particle size are provided in the following equation.

$$d = \frac{K\lambda}{B\cos\theta}$$

Where, d is particle diameter (nm), κ is the shape factor, λ is wavelength of wavelength of the x-rays (0.154 nm for Cu-Kα), B is the full width at half maximum (FWHM) of the diffracted peak in radian and θ is the Bragg angle of the same peak in degrees. In addition, Vergard's law can be used to calculate the lattice parameters "a".

$$a = \frac{\sqrt{2}\lambda\kappa}{sin\theta}$$

3.2.5 X-ray photoelectron spectroscopy

X-ray photoelectron spectroscopy (XPS) is a characterization technique used to investigate chemical states, electronic states and surface elemental composition of the sample material. It is also used to identify binding states of the element. XPS uses x-ray photons known energy to irradiate the sample, emitted electrons from the surface (top 1 to 10 nm) follows photoelectric effect. The emitted electrons kinetic energy and intensities are measured. Difference in emitted and initial x-rays energy are used to calculate electron binding energy which is characteristic of individual elements and their oxidation state. Electron binding energies are characteristics of several factors, which include type of atom, the chemical state and the empirical state which are related to obtained spectra.[113] The overall spectra is deconvoluted into distinct spectra, and various distinct spectra can be quantified which is specific to different structures, bonding, oxidation states and atomic arrangements. In this study, XPS is used to study heteroatom doping on the Graphene and other carbon support material and their interaction with platinum atom.

3.2.6 Brunauer, Emmet, Teller Adsorption Isotherm

Brunauer, Emmet, Teller Adsorption Isotherm (BET) analysis is used to measure surface area, pore size, pore volume distribution of the material. The gas (nitrogen) absorption analysis is based on a number of assumptions: adsorption is limited to well defined sites of samples; no interaction between the adsorption layers, and layer number can go up to infinity at saturation pressure.[114] Gas sorption is very important in obtaining structural information when material is porous. Surface area play an important role in catalyst development as high surface area to volume ratio is critical to the active sites and performance. In a typical procedure, a known weight of samples are vacuumed at a temperature range of 60-200 ºC to remove moisture and impurities (known as degassing). For analysis, the sample tube temperature is reduced to liquid nitrogen temperature and exposed to nitrogen gas to determine nitrogen absorption isotherm. BET surface area and porosity is determined through BET adsorption isotherm was used to characterize support material and catalyst in this thesis work.

3.3 Electrochemical Characterization and performance evaluation

To evaluate electrochemical properties and activity of synthesized catalysts, different electrochemical characterization techniques are employed in this project. This section provides an introduction and background information about different electrochemical characterization techniques.

3.3.1 Cyclic voltammetry

Cyclic voltammetry (CV) is an electrochemical technique use to examine the electrochemical property of electrodes by controlling potential. In CV test, the potential of the

working electrode is varied linearly between two assigned potential limits with time or certain scan rate (mV s^{-1}) and corresponding currents are measured. **Figure 3-1** shows a typical potential cycle for Pt/C catalyst which was performed at a scan rate of 50 mV/s in N_2-saturated 0.1 M $HClO_4$ solution between 0.05 to 1.3 V vs RHE. Herein, positive and negative current corresponds to anodic and cathodic current respectively. The CV plot can be divided into three major regions: (i) H underpotential deposition region (~0.05 to 0.4 V vs RHE), (ii) double layer region (0.4 to 0.7 V vs RHE) and (iii) Pt oxide formation region (above 0.7 vs RHE). In the 0.05 to 0.4 V vs RHE region during the forward scan, the pre-absorbed H atoms on the Pt atom oxidized to H^+ ion and desorb from Pt surface and diffuses in electrolyte. Above 0.7 V vs RHE, Pt is oxidized to form Pt-OH then further to Pt-O by the adsorption or dissociation of H_2O molecules. After cycling when potential comes back at 0.7 V vs RHE in backward scan, Pt-O are reduced. Further decrease in potential below 0.4 V vs RHE, the proton in the electrolyte will be adsorb on the Pt surface and will reduced according to known H under potential deposition. In capacitance region of ~0.4-0.7 V vs RHE, Pt surface is freed from H or OH/H and is known as the double layer region. The measured current in this region is due to capacitive effects of large surface area of carbon support and anionic adsorption of electrolyte. The capacitive current in this region is not due faradaic process and subtracted from faradaic currents before estimating electrochemical active surface area (ECSA) of the Pt catalyst. In general, charge associated with H adsorption and desorption peak is integrated to determine the number of H atoms absorbed on a monolayer on electrode surface. The electric charge density C due to covered H atoms is 0.21 mC/cm^2_{Pt}. The specific ECSA of Pt (m^2 gm^{-1}_{Pt}) can determined as follows:

$$ECSA = \frac{Q}{mC}$$

Where, Q is the total integrated charge for H adsorption/desorption (mC/cm^2 electrode) obtained from CV plot and m is the mass of the platinum loading (mg/cm^2 electrode).

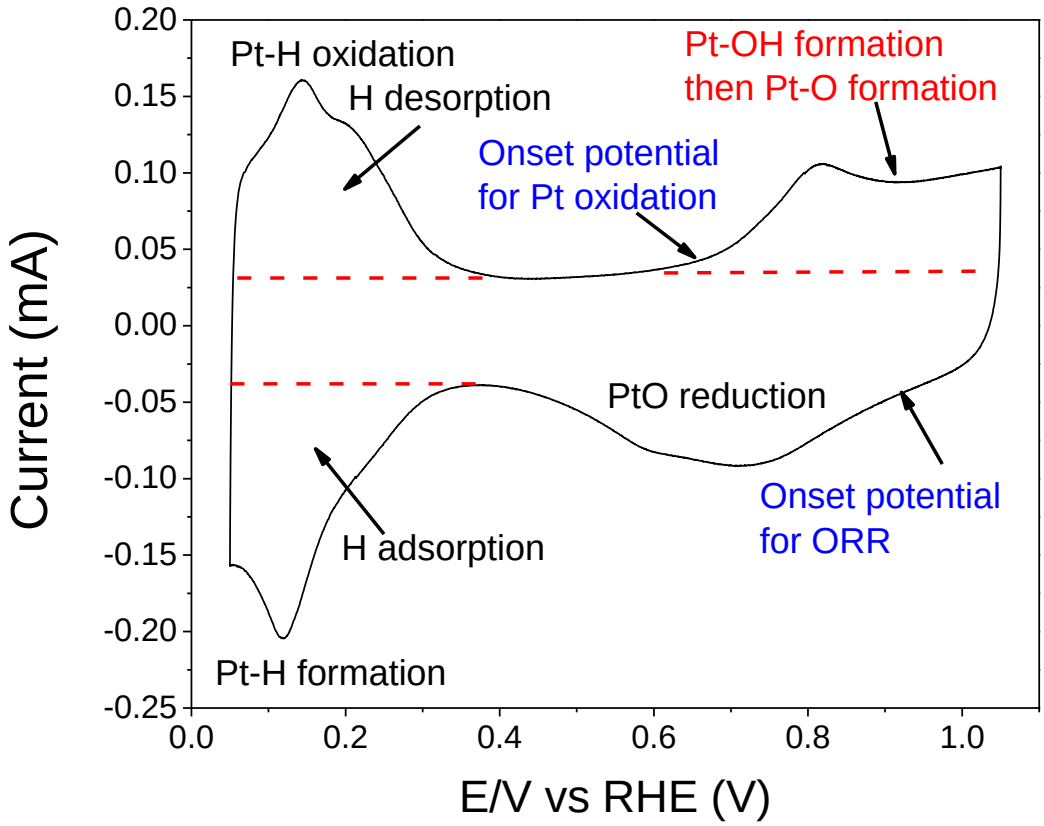

Figure 3-1: Typical CV of the commercial Pt/C catalyst.

3.3.2 Rotating disc electrode testing

For Half-cell testing, rotating disc electrode (RDE) testing is a well-known technique to screen the electrochemical activity of the catalyst material. Due to simplicity and less time

consuming RDE is a highly effective method for screening high throughput catalyst activity for various reactions. Half-cell testing system is a three-electrode system, where there is working electrode, reference electrode, counter electrode and electrochemical cell filled with electrolyte solution. For current projects, 0.1 M $HClO_4$ will be used as the electrolyte in order to simulate the acidic conditions prevailing at the cathode of PEMFCs. The working electrode is a glassy carbon disc on which catalyst materials is deposited for investigation, reversible hydrogen electrode (RHE) as reference and platinum disc/wire as counter electrode. Catalyst material was deposited in the form of catalyst ink, prepared by mixing catalyst material in ethanol/isopropanol/DDI and 5 % Nafion solution and sonicating in water bath for half an hour to achieve uniform dispersion. Known quantity of catalyst ink was deposited on glassy surface and allowed to dry. During testing condition, working electrode is immersed in oxygen saturated electrolyte solution, and current is recorded at sweeping potential to evaluate ORR kinetics of the material. The rotation of the working electrode was to avoid any mass transfer resistance and induce convective mass transport of oxygen to the electrode by maintaining laminar flow in the cell.

RDE techniques can precisely measure electrocatalytic activity by differentiating between limited catalyst activity and mass transfer limitation of reactant gas. The intrinsic property of the electrolyte and rotation of electrode determines the gas flux to the electrode surface. Relation between measured current 'i', kinetic current i_k due to kinetic limitations and diffusion current i_d due to mass transport limitation is explained with Koutechy-Levich equation as follows:

$$\frac{1}{i} = \frac{1}{nFkC_{\circ}} + \left(\frac{1}{0.620nFAD^{\frac{2}{3}}v^{-\frac{1}{6}}C}\right)\omega^{2/3}$$

$$\frac{1}{i} = \frac{1}{i_k} + \frac{1}{i_d}$$

$i_k = nFkC_o$

$i_d = 0.62nFD_0^{2/3}\,\upsilon^{-1/6}C_o\omega^{1/2}$

In the above equations, i_k and i_d is the kinetic and limiting current density, respectively, F is the Faraday constant (96 485 C mol-1), k is the rate constant for ORR, D_0 is the diffusion coefficient of O_2 (1.9 x 10-5 $cm^2\ s^{-1}$ in 0.1 M KOH and 1.67 x 10^{-5} $cm^2\ s^{-1}$ in 0.1 M $HClO_4$), υ is the kinematic viscosity of electrolyte (0.01 $cm^2\ s^{-1}$), C_o is the concentration of O_2 in the electrolyte (1.1 x 10^{-6} mol cm^{-3} in 0.1 M KOH and 1.36 x 10^{-6} mol cm^{-3} in 0.1 M $HClO_4$) and ω is the angular frequency of the rotation (rad s^{-1}). Koutecky-Levich (K-L) plot can be obtained by plotting between $\frac{1}{i}\ vs\ \omega^{-1/2}$, while y-intercepts is $1/i_k$ and slope equals to the number of electrons transferred during reaction at electrode. Typically, kinetic current for ORR is measured at 0.9V vs RHE to calculate specific and mass activity for Pt based catalyst. Number of electrons transferred measured for an ORR in K-L plot use to calculate efficiency of the synthesized catalyst. The ORR polarization curve can be divided into three regions: (i) At potential above 0.9V vs RHE minimal current flow due to insufficient overpotential to drive the oxygen reduction reaction in forward direction, (ii) Between 0.7-0.9 V vs RHE, mixed-controlled region where overall rate is affected by both ORR kinetics and O_2 mass transport (iii) Below 0.7 V vs RHE, diffusion-controlled region due to rate-limitation of O_2 transport to the catalyst surface. (Figure 3-2).

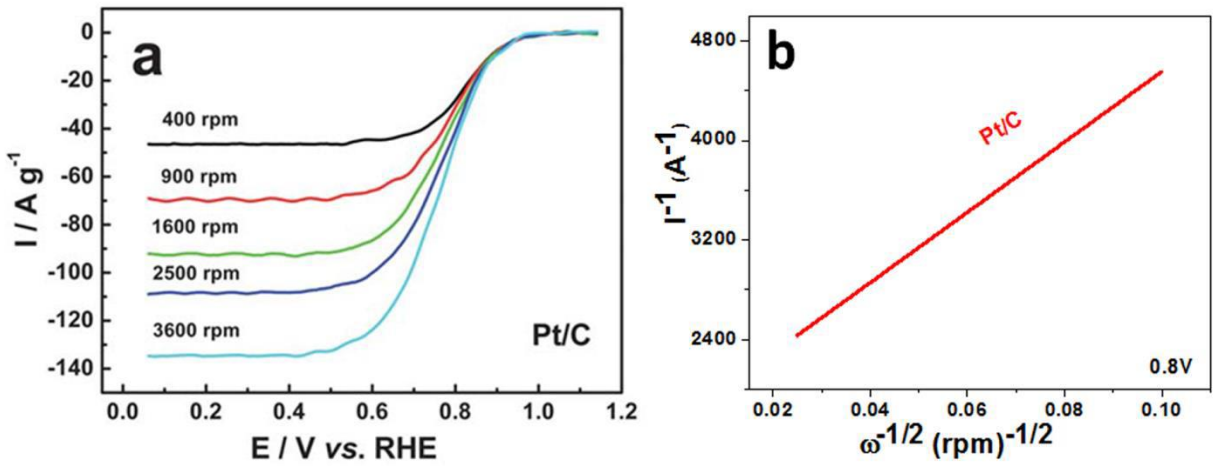

Figure 3-2: (a) ORR polarization curve of commercial Pt/C and (b) and corresponding K-L plot at 0.8 V vs RHE.

3.3.3 Rotating ring disc electrode

Rotating ring disc electrode (RRDE) is an extension of RDE technique, consist of an extra ring-type working electrode made up of platinum surrounding glassy carbon disc (**Figure 3-3**). This arrangement helps the system to determine hydrogen peroxide generation, therefore, selectivity of the catalyst. The electrode is designed to measure two current readings; current from disc and current from platinum ring. Current from platinum ring is used to calculate the hydrogen peroxide formation during the potential scanning.

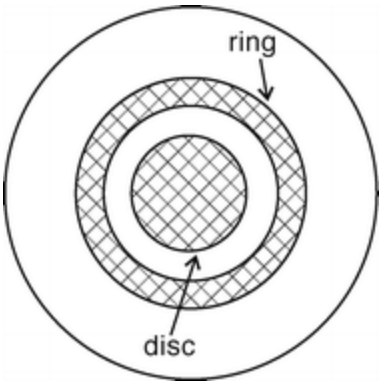

Figure 3-3: Schematic representation of a RRDE head from a top view. Reproduced with permissions from.[115] Copyright © 2010 Springer.

Oxygen reduction with two different pathways produced H_2O and H_2O_2 simultaneously at the working electrode, while due to laminar flow all the product will be pushed away from disc towards the ring. At certain voltage H_2O_2 can reduce to H_2O, while current change can be monitored at the second working electrode. The following equation can be used to estimate between the 2-electron and 4-electron pathway reaction.

$$n = 4|I_D|/\left(|I_D| + (|I_R|/N)\right)$$

$$\%H_2O_2 = 100(4 - n)/2$$

$$\%H_2O = 100 - \%H_2O_2$$

Where n is the number of electrons transferred, I_D is the current from the disc electrode, I_R is the current from the ring electrode, N is the collection efficiency which is provided by manufacture of instruments. $\%H_2O_2$ is the selectivity of H_2O_2 and $\%H_2O$ is the selectivity of H_2O. Based on this information it is possible to analyze the number of electrons transferred during ORR and the percentage of 2-electron pathway over 4-electron pathway reaction.

3.3.4 Half-cell accelerated degradation testing

Accelerated durability test is used to investigate the durability of the catalyst in a short period of time. The CV test procedure is applied with large potential range based on need in an N_2-saturated solution. The catalyst is subject to different potential cycle ranges (e.g. 0.6-1.1 V, 0.05 – 1.2 or 1.3 or 1.5 V vs RHE) for thousands of cycles. These transient conditions will provide information about catalyst stability and degradation. Catalyst performance can be determined by comparing ORR activities before and after potential cycles. Different ADT protocol has been available in literature and can be used based on projects objective to determine catalyst stability.

3.3.5 Membrane electrode assembly testing

Membrane electrode assembly (MEA) is simply a single cell PEMFC, consisting of a polymer membrane assembled between an anode and a cathode sandwiched between gas diffusion layer (GDL). MEA simulate an actual PEMFCs setup and provide real assessment of catalyst and electrode performance. The electrode is fabricated by depositing catalyst on a GDL, which can be done by spraying, painting, filtering or electrodepositing.[116] The catalyst coated GDL is hot pressed together with electrolyte membrane in order to achieve MEA assembly and ensuring uniform contact and adhesion. Catalyst can also be coated on membrane called catalyst coated membrane (CCM). Different electrode and MEA fabrication methods can result in variable electrode architect and affect catalyst performance and stability. MEA is very sensitive to membrane preparation and assembly process and every step in doing so can affect catalyst MEA testing results.

The performance and evaluation of catalyst will be done by cycling the cell from open circuit conditions (no current being drawn) to very high current densities. The cell voltage will be recorded against current density leads to MEA polarization curve. Several cycles will be performed to ensure adequate hydration of electrolyte membrane and catalyst activation before performance evaluations. Electrode durability can also be measured by a variety of different techniques, such as repeating cycle of electrode potential, or can be more complex drive cycle simulation as suggested by DOE.[1]

Chapter 4: Platinum-palladium core-shell nanoflower catalyst with improved activity and excellent durability for oxygen reduction reaction

4.1 Introduction

Platinum (Pt) is the most critical component of the catalysts used to facilitate the oxygen reduction reaction (ORR) in polymer electrolyte membrane fuel cells (PEMFCs). While it offers a higher catalytic activity for ORR than any other metal, the sluggish ORR kinetics, low durability, and persistently high price of Pt limits large scale commercialization of PEMFCs. At present, desired fuel cell performance and stability under simulated drive cycles requires significantly higher Pt loading compared to the Department of Energy (DOE) guidelines.[1] Therefore, reducing Pt loading and improving durability is a central focus of industrial and academic research. At cathode in PEMFCs, in the first step oxygen gas is adsorbed at the active sites, where it reacts with an electron and proton to form OOH species. This oxygen group further reacts with protons and electrons and leads to the formation of H_2O. If oxygen species are strongly adsorbed, this reduces the availability of active sites and negatively affects ORR activity. The addition of secondary metals such as palladium (Pd) to Pt can change the d-band center, surface atomic arrangement and decrease chemisorption of oxygen-containing species (mostly hydroxyl ions), thus positively impacting the ORR kinetics.[117] However, the binding energy of oxygen on Pd is 0.4 eV higher than Pt, which results in lower ORR activity of Pd and highlights the importance of limiting surface exposure of pure Pd in Pt-Pd catalysts. It has also been recognized that strain development in Pt-

based materials can decrease the binding affinity of oxygen groups. Therefore, core-shell nanostructure catalysts such as Pt-Pd structures can be engineered to create internal strain to improve ORR activity.[118] Pt-Pd catalysts can also exhibit better durability than pure Pt, as addition of Pd could prevent the corrosion of Pt by sacrificing itself to provide cathodic protection.[119]

Careful design of Pt nanostructures is another effective way to modulate the activity and protect against loss of electrochemically active surface area (ECSA).[120–122] Pt-based catalysts currently used in PEMFCs consist of 2-5 nm nanoparticles having ill-defined shapes and facet structures.[123] Zero-dimensional (0D) Pt/C nanoparticles, while offering high surface area, have diminished electrocatalytic activity due to their significant number of defect sites, lattice boundaries and low atomic coordination on the surface. During PEMFC operation, which is typically in the voltage range of 0.8-0.9 V or above, Pt nanoparticles are also susceptible to agglomeration, dissolution and Ostwald ripening due to their high surface energy and carbon support corrosion, which ultimately results in detachment of Pt nanoparticles from the support and an ensuing decline in performance.[124–126] Therefore, Pt particle properties and the interaction between Pt and the support material play an important role in the catalyst's activity and stability. Two-dimensional (2D) Pt nanostructures such as plate or flower-like structures can be engineered to improve durability by growing onto stable nanostructured support materials such as graphene or carbon nanotubes.[63,126,127] When compared with commercial carbon black, graphene possesses an incredible improvement in chemical, mechanical and electrical properties due to its unique 2D sp^2 hybridized carbon structure[63,126,127]. Traditional carbon can be heated to high temperatures (~1000 ºC), leading to lattice rearrangement and an increase in graphitic nature of the material.

Graphitization produces a highly resistant material to oxidation and carbon corrosion. To further improve performance, several studies have incorporated heteroatoms doping of graphene as an efficient way to tune intrinsic properties, which is helpful in improving electrocatalyst activity and stability.[127,128]

Recent research efforts have been focused on the development of less expensive and improved electrochemically active catalysts such as advanced Pt alloys, non-precious metal catalysts, and core-shell catalysts. Among these, core-shell structure catalysts consisting of a thin layer of Pt deposited on low cost seed material has attracted considerable attention.[119,121,129,130] Deposition of an ultrathin Pt shell on Pd offers a great opportunity to enhance catalytic activity and durability while reducing its loading.[129,131] However, non-uniform deposition of the Pt shell and long-term durability at high potential range is still a problem with core-shell structures. This motivated us to carefully design a Pt-Pd electrocatalyst and integrated uniquely carbon support to improve durability and achieve the DOE targets. To improve Pt-based ORR activity and more importantly long-term durability, herein, we report a Pt-Pd core-shell nanoflower supported on sulfur-doped graphene (SG) with improved activity and excellent durability. The 2D nano-architecture of the core-shell nanoflowers provides enhanced surface activity and improved electron kinetics, while sulfur atoms doped on graphene support provide a strong anchor for the nanoflowers through tethering behavior, leading to excellent durability under very aggressive test conditions.[108] The electrochemical activity and stability of the prepared electrocatalyst was investigated. Enhancement in electrochemical activity can be attributed to the nanoflower core-shell Pt-Pd nanostructure and weak –OH binding to Pt in comparison to Pd. The morphology of

the catalyst was responsible for high ECSA, while its core-shell structure and the interaction between the catalyst and highly robust SG play facilitate long-term stability to high potential cycling.

4.2 Experimental Section

4.2.1 Graphene oxide synthesis:

Graphene oxide was synthesized using a modified Hummer's method. Graphite powder (Alfa Aesar, natural, microcrystal grade, APS 2-15 micron, 99.9995%) was oxidized to graphene oxide. In brief, 2 g of graphite powder was added to a mixture of 360 and 40 ml of H_2SO_4 and H_3PO_4 respectively. The solution was stirred for 30 minutes. Then, 18 g of $KMnO_4$ was added slowly and the reaction proceeded at 50 ºC for 18 hours. After completion, the temperature was cooled down to 10 ºC with addition of 400 ml of DDI water to the solution. The oxidation reaction was completed with addition of 15 ml of 30% H_2O_2. The final solution was centrifuged and then washed with ethanol and 30% HCl once followed by DDI 4-5 times, and then freeze dried for approximately 96 hours.

4.2.2 Sulphur-doped Graphene Synthesis:

Sulphur-doped graphene was prepared by using a thermal shock/annealing process. Typically, 150 mg of graphene oxide was mixed together with same mass of Phenyl disulfide (PDS, Sigma Aldrich). The mixture was transferred to a quartz tube and annealing at 1000ºC for 30 minutes in the presence of argon gas.[108] This was performed by keeping mixture away from the heating zone while furnace reached the required temperature, followed by moving the sample

inside for flash heating. The sample was removed from the heating zone after 30 minutes to cool rapidly under argon gas.

4.2.3 Palladium seeds synthesis:

The Pd seeds were synthesized using 480 mg of PVP dissolved in 12 ml DEG, which was heated at 130 ºC in an oil bath under vigorous magnetic stirring for 10 minutes. 15.5 mg Na_2PdCl_4 was dissolved in 6 ml of DEG and the solution was quickly injected in the preheated PVP solution, with the reaction proceeding at 130 ºC for 3 hours and 30 minutes. The product was collected using centrifugation and washed using acetone and ethanol.

4.2.4 Palladium seeds attachment on Sulphur doped graphene:

In a standard experiment, 1.0 mg of Pd seeds (from the previous Pd seed solution) were placed in a mixture of 29 ml EG, 91 mg KBr, 54 mg Ascorbic acid, 110 mg PVP (MW= 55000) and SG. Uniform dispersion of SG in the solution was achieved after 30 minutes of sonication. The solution was then heated at 110 ºC for one hour, and then raised to 200 ºC in 15 minutes.

4.2.5 Palladium @ Platinum synthesis:

A Pt solution was prepared with 48 mg of Chloroplatinic acid hexahydrate dissolved in 104 mL of EG. 48 mg of Chloroplatinic acid hexahydrate per mg of Pd was used to achieve a 9:1 Pt to Pd ratio. The deposition of Pt was initiated by pumping Pt solution at a rate of 16.0 ml per hour into the Pd/SG solution after its temperature reached 200 ºC. After pumping of Pt solution was completed, the reaction solution was maintained at same condition for an hour.

4.2.6 Material characterization:

The morphology and structure of the synthesized materials were imaged by transmission electron microscopy (TEM; JEOL, JEM-2010, 200 kV) with built-in energy dispersive x-ray spectroscopy (EDX). Electron energy loss spectroscopy (EELS) was performed on a FEI Titan 80-300 HB operated at 200 kV. X-ray photoelectron spectroscopy (XPS; Thermal scientific K-Alpha XPS spectrometer) and powder X-ray diffraction (XRD; Bruker AXS D8 Advance) patterns were recorded to analyze surface chemistry and crystal structure, respectively.

4.2.7 Electrochemical measurements:

The electrocatalytic performance for oxygen reduction was investigated with a rotating disc electrode in a three-electrode cell at room temperature. The electrode system contained a glassy carbon electrode (GC; 5 mm in diameter), Pt wire and reversible hydrogen electrode (RHE) as the working, counter and reference electrode respectively. Each catalyst ink was prepared by mixing 1 mg of the catalyst in 490 μL of ethanol and 10 μL of 5 wt% Nafion^{TM}; 0.35 g of carbon black was also added to achieve better dispersion. The catalyst solution was ultrasonicated for 30 minutes to obtain a homogenous ink. 10 μL of prepared ink was dropped onto the GC surface for all catalysts. Commercial Pt/C (28.8 wt. % Pt) was used as the benchmark catalyst. All measurements were carried out in 0.1 M $HClO_4$ solution at room temperature, with N_2 gas saturation used for CV/ECSA measurements and O_2 gas saturation used for ORR polarization measurements. The ORR activity was measured at a potential scan rate of 10 mV s^{-1} and the CV curves were obtained at 50 mV s^{-1} to calculate the ECSA of each catalyst. Accelerated degradation testing (ADT) was carried out at by cycling the electrode potential between 0.05 and 1.2 V vs RHE at a scan rate of 50 mVs^{-1} up to 10,000 cycles under N_2 gas saturation.

4.3 Result and discussion

The catalyst synthesis procedure is demonstrated in **Figure 4-1**, and the detailed synthesis route and reaction mechanism is provided in **Figure 4-2**. Pd nanoparticle seeds were selectively synthesized through manipulation of the reduction kinetics of the polyol process,[132,133] by reducing Pd salt ($PdCl_4^{2-}$) with diethylene glycol (DEG) and polyvinyl pyrrolidone (PVP) (**Figure 4-1a-b**). Generally, metallic particles are thermodynamically favored to form into bulk shapes to lower surface free energies. The addition of PVP reduced the reduction rate and allowed the nucleation and growth to be kinetically controlled,[134] which prevented the nanoparticles from growing too large and agglomerating. Separately, graphene oxide (GO) and phenyl disulfide (PDS) were mixed and subjected to a thermal shock (1000 ºC) and quenching process to synthesize SG, which exhibits a multilayer sheet-like structure (**Figure 4-1c**). The Pd seeds, which served as a template for Pt deposition, were well dispersed and attached onto SG (**Figure 4-1c**) in a solution of ethylene glycol, PVP, potassium bromide (KBr) and ascorbic acid and heated at 110 ºC for an hour. The final product, Pt-Pd core-shell nanoflowers on SG (Pt-PdNF/SG) (**Figure 4-1d**), was synthesized by an in-situ continuous feeding method. A syringe pump was used to introduce a solution of $Na_2PtCl_6 \cdot 6H_2O$ and ethylene glycol (EG) into the growth solution used for attaching Pd seeds on SG. Addition of the Pt precursor into the growth solution caused immediate reduction to metallic Pt by ascorbic acid and EG. A low injection rate was used to maintain low concentrations of Pt,

thus preventing self-nucleation and agglomeration while promoting highly dispersed Pt deposition.

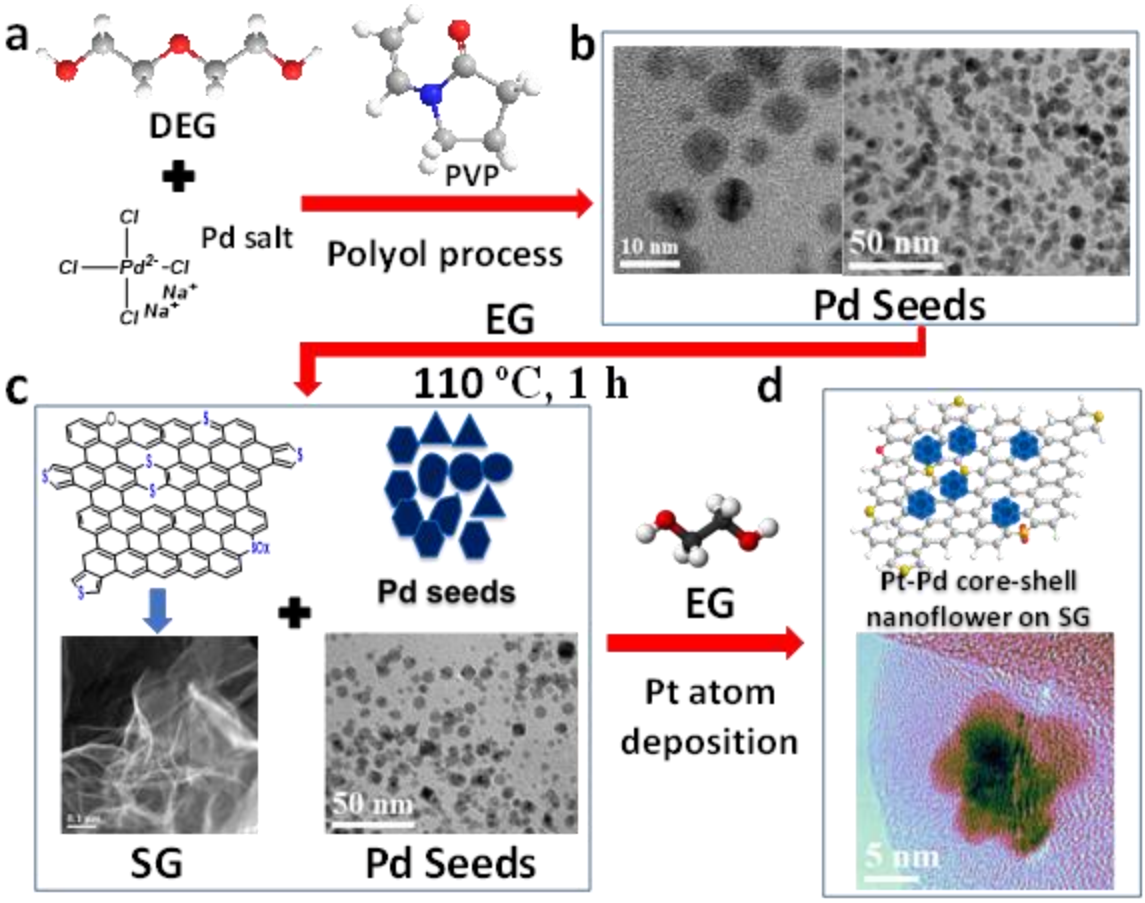

Figure 4-1: Schematic illustrations of synthesis of Pt_xPd_y-NF/SG core-shell nanoflower (here x, y subscript represents atomic percentage) synthesis. Synthesis followed as Pd seed synthesis, Pd deposition on SG, with in-situ Pt deposition on Pd seed. Here light blue (Pt), dark blue (Pd) and yellow (S) in Pt-Pd core-shell nanoflower.

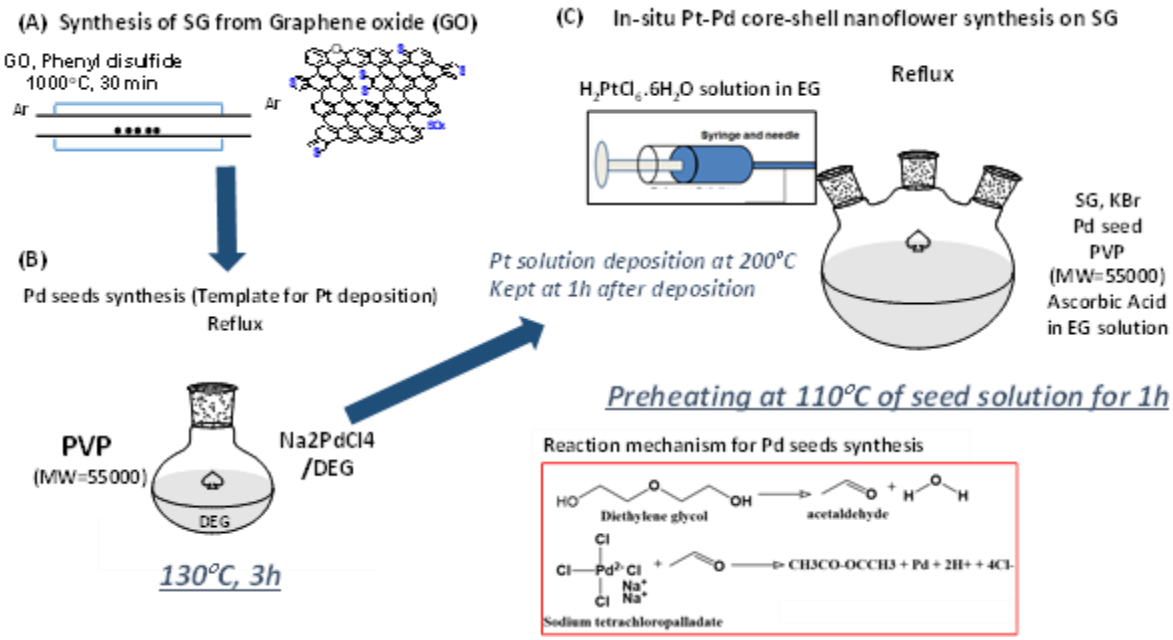

Figure 4-2: An overall step by step synthesis route and reaction mechanism.

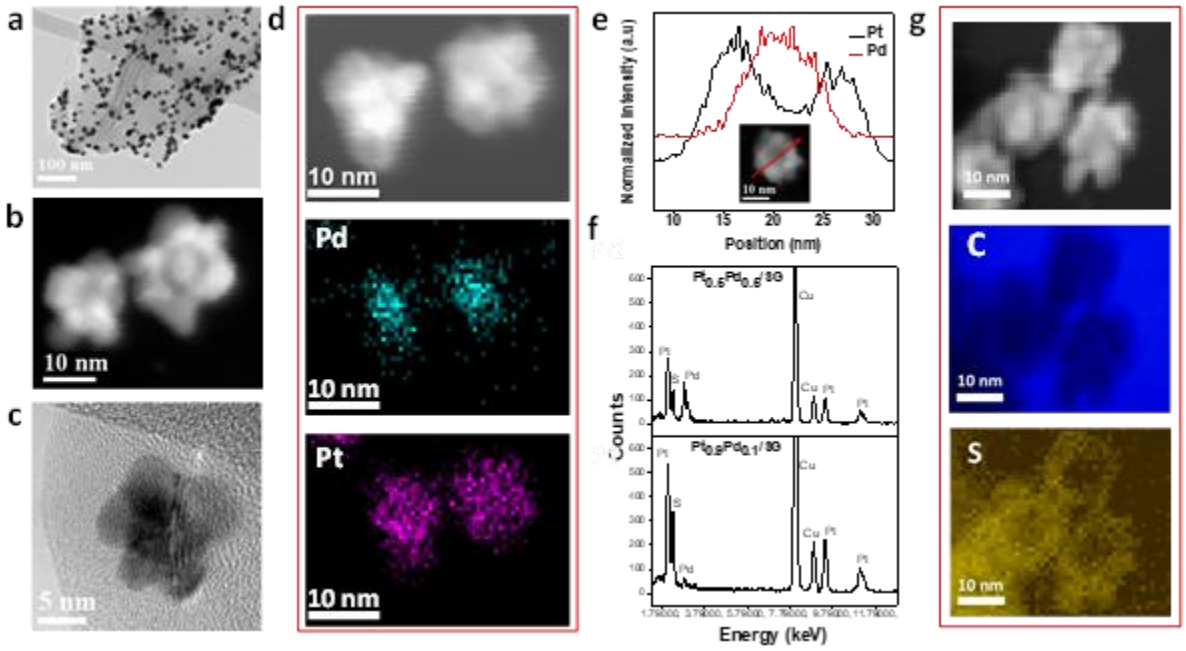

Figure 4-3: (a) TEM image of $Pt_{0.9}Pd_{0.1}$/SG (Pt-Pd core-shell nanoflower). (b) HAADF-STEM image of $Pt_{0.9}Pd_{0.1}$/SG Pt-Pd core-shell nanoflower. (c) HR-TEM image of Pt-Pd core-shell nanoflower. (d) HAADF-STEM image of two Pt-Pd core-shell nanoflower particle and their corresponding EDX maps of Pd and Pt. (e) EDX line scan of profiles of Pt (black) and Pd (red) of a single Pt-Pd core shell nanoflower particle. (f) EDX spectra comparison of $Pt_{0.5}Pd_{0.5}$/SG and $Pt_{0.9}Pd_{0.1}$/SG with Pt, Pd and S peaks (Cu peaks are attributed to the TEM grid). HAADF-STEM image of Pt-Pd cores-shell nanoflowers and corresponding EELS spectra of sulfur (S) and carbon (C).

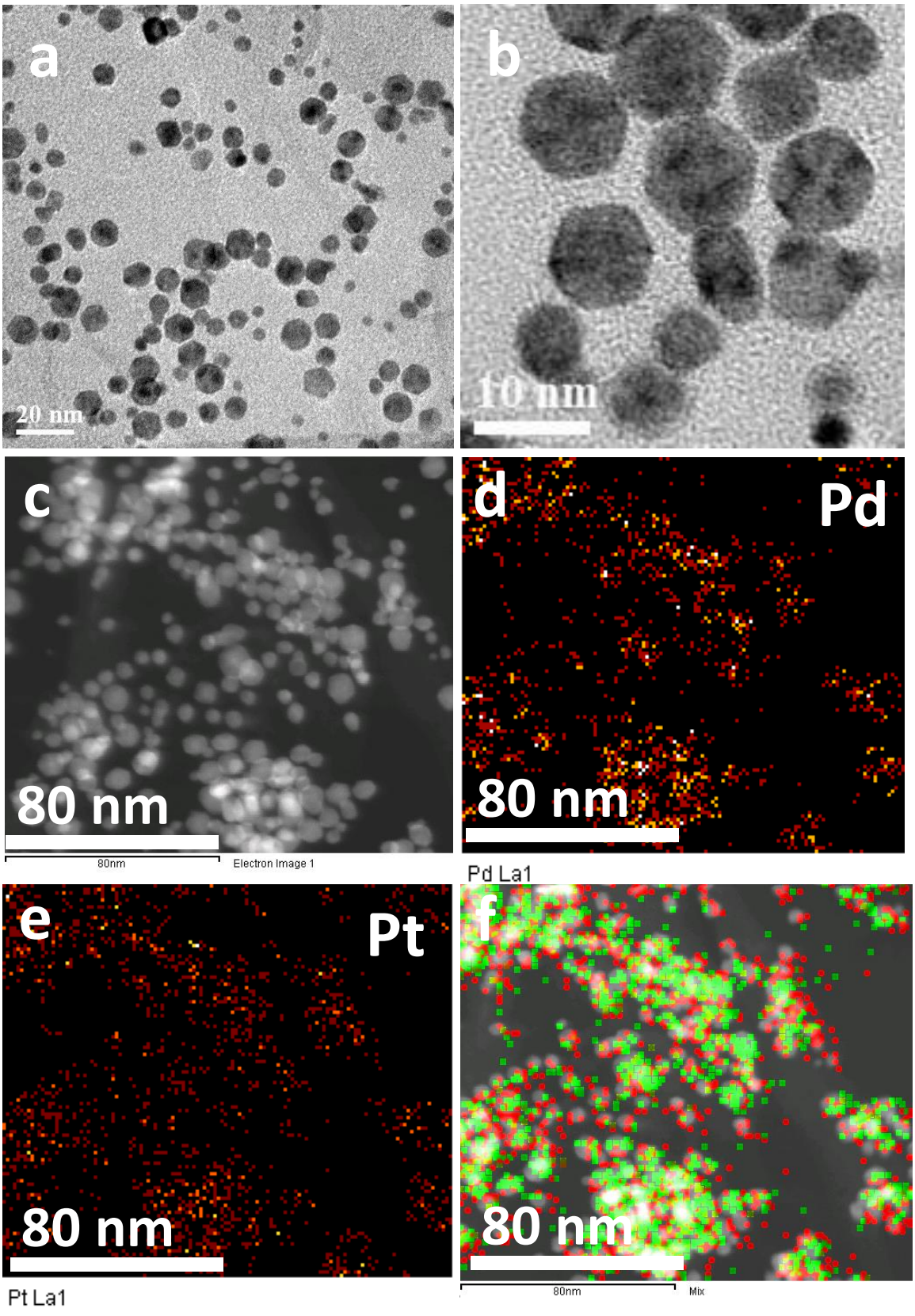
a
20 nm
b
10 nm
c
80 nm
80nm
Electron Image 1
d
Pd
80 nm
Pd La1
e
Pt
80 nm
Pt La1
f
80 nm
80nm
Mix

Figure 4-4: TEM images of $Pt_{0.5}Pd_{0.5}$/SG (a) low magnification, (b) high magnification, (c) STEM image, (d) corresponding EDX elemental mapping of Pd, (e) corresponding EDX elemental mapping of Pt and (f) RGB mix of Pt (red) and Pd (green).

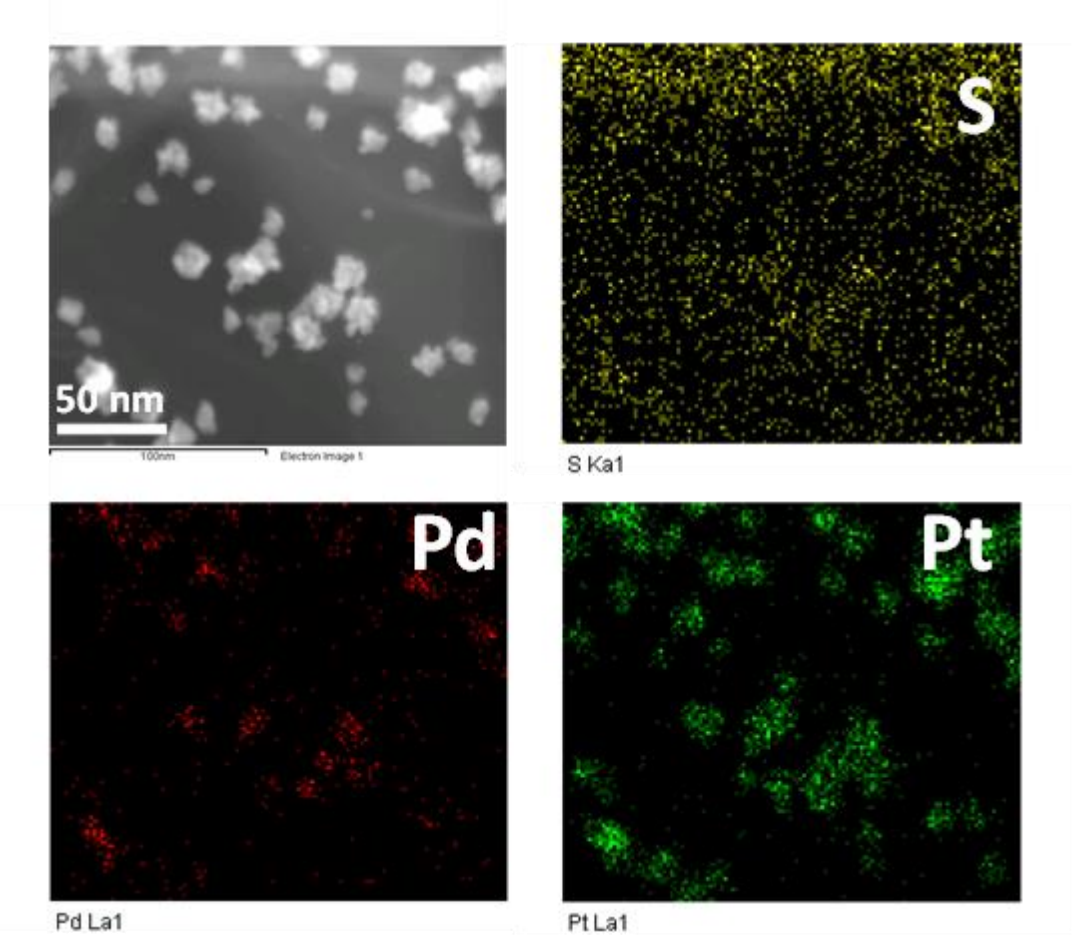

Figure 4-5: Low magnification TEM EDX mapping of sulfur (S), Pd and Pt in $Pt_{0.9}Pd_{0.1}$/SG.

The transmission electron microscopy (TEM) images in **Figure 4-3(a-c)** shows well attached and dispersed nanoflowers on SG sheets. PtPd-NF/SG was synthesized with different Pt:Pd atomic ratios, with 90 at.% Pt ($Pt_{0.9}Pd_{0.1}$/SG, **Figure 4-3a-c**) and 50 at.% Pt ($Pt_{0.5}Pd_{0.5}$/SG), (**Figure 4-4**). $Pt_{0.9}Pd_{0.1}$/SG appears well dispersed on SG (**Figure 4-3a**), and their nanoflower morphology is confirmed in the high-angle annular dark-field scanning TEM (HAADF-STEM) and high-

resolution TEM (HR-TEM) images in **Figure 4-3(b-c)**. Energy dispersive X-ray spectroscopy (EDX) was used to detect the distribution of elements (particularly Pt and Pd) in the material, while electron energy loss spectroscopy (EELS) was employed to detect light elements (i.e. carbon and sulfur) with high spatial resolution. EDX elemental mapping of two particles of $Pt_{0.9}Pd_{0.1}$/SG (**Figure 4-3d**) confirm the Pd core-Pt shell structural distribution of these two elements. To further confirm the core-shell structure, an EDX line scan profile of Pd (red) and Pt (black) across a Pt-Pd nanoflower is shown in **Figure 4-3e**, which displays normalized intensities of Pd and Pt. The two high-Pt intensity peaks at the sides with the high-Pd intensity peak in between indicates the presence of a Pd core and Pt shell. The size of the core and entire core-shell structure is 5-10 nm and 15-20 nm, respectively. The EDX spectra of sulfur, Pt and Pd in $Pt_{0.9}Pd_{0.1}$/SG and $Pt_{0.5}Pd_{0.5}$/SG are compared in **Figure 4-3f**, with the larger Pt peak in $Pt_{0.9}Pd_{0.1}$/SG and larger Pd peak in $Pt_{0.5}Pd_{0.5}$/SG indicating the successful control of the relative elements in each structure. In **Figure 4-5**, a low magnification HAADF-STEM image and corresponding EDX maps show the same Pd core-Pt shell structure across most of the $Pt_{0.9}Pd_{0.1}$/SG particles, while sulfur is homogenously distributed across the SG sheet. **Figure 4-6** shows a lower magnification HAADF-STEM overview of $Pt_{0.9}Pd_{0.1}$ nanoflower distribution on SG, with EDX elemental mapping indicating homogenous distribution of sulfur atoms and PtPd nanoflowers across the graphene sheet. **Figure 4-3g** displays a HAADF-STEM image of $Pt_{0.9}Pd_{0.1}$/SG and associated electron energy loss spectroscopy (EELS) maps of sulfur and carbon. Sulfur is concentrated particularly underneath the Pt petals of the nanoflower, indicating the desirable anchoring interaction between these two elements as demonstrated in our previous works.[108,135]

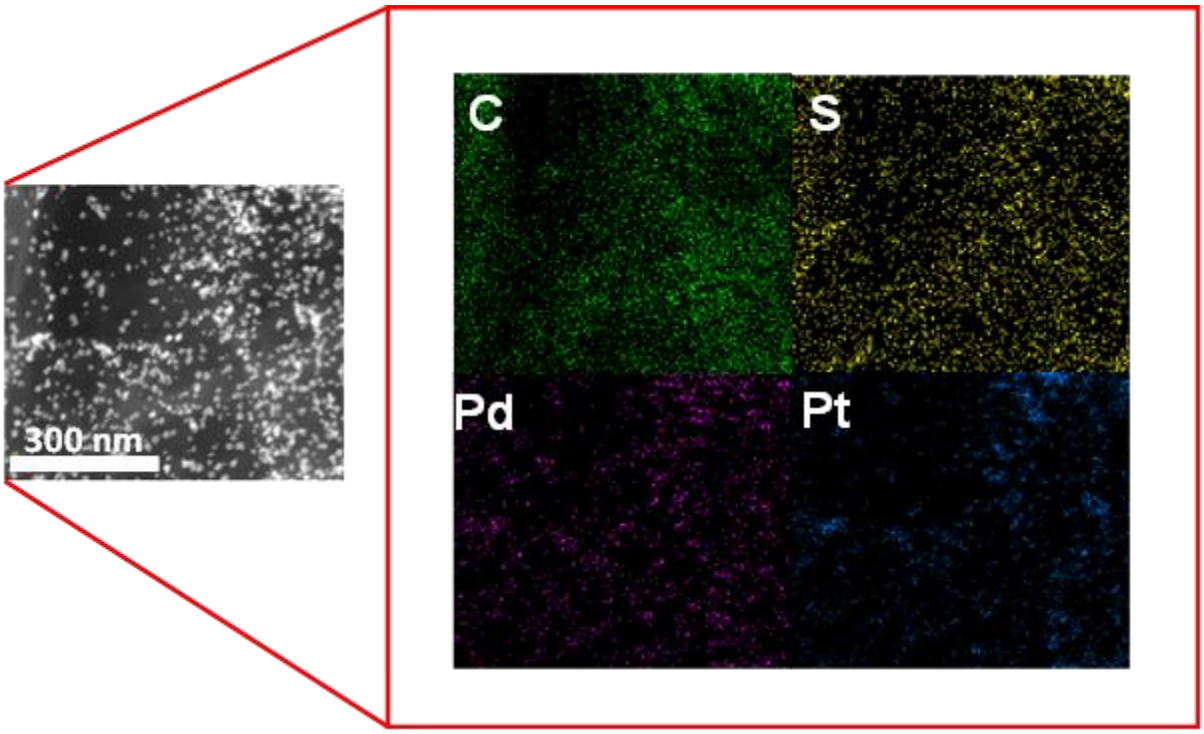

Figure 4-6: Overview TEM EDX mapping of $Pt_{0.9}Pd_{0.1}$/SG.

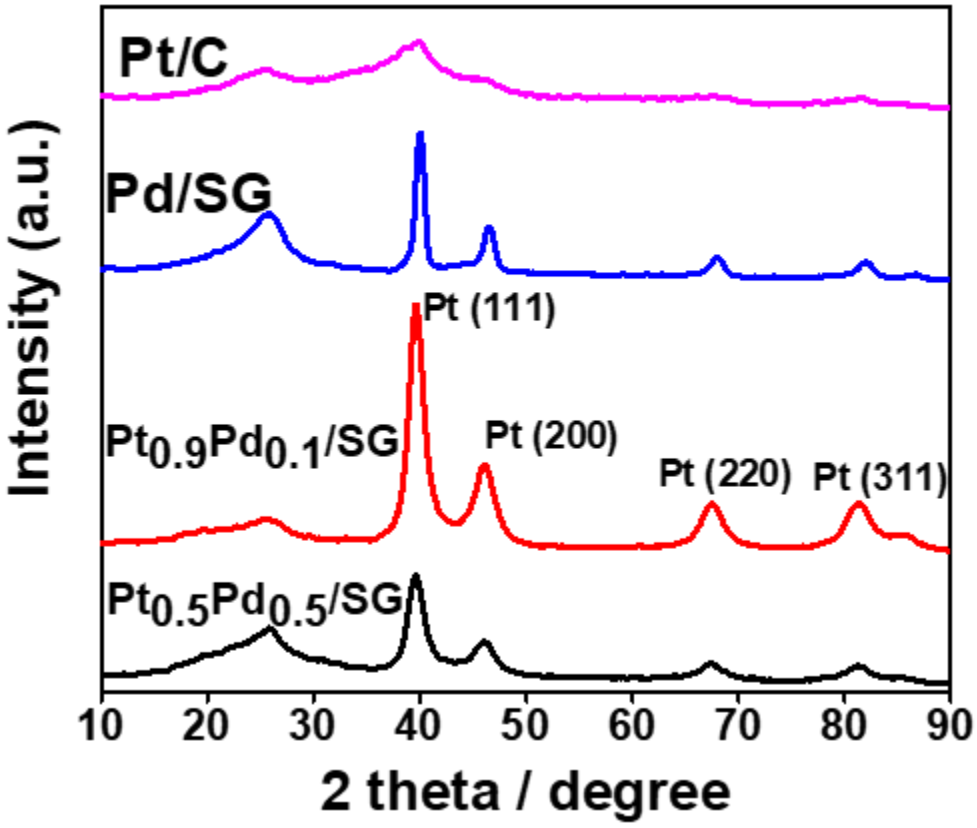

Figure 4-7: XRD spectra of Pt/C, Pd/SG, $Pt_{0.9}Pd_{0.1}$/SG and $Pt_{0.5}Pd_{0.5}$/SG.

Figure 4-7 shows that the X-ray diffraction (XRD) patterns of $Pt_{0.9}Pd_{0.1}$/SG and $Pt_{0.5}Pd_{0.5}$/SG reveal typical Pt-fcc peaks (JCPDS No. 04-0802), with diffraction pattern of Pd/SG and commercial Pt/C shown for comparison. The (111) crystal face, which delivers increased Pt mass based ORR activity in comparison to commercial Pt/C,[62,136,137] is prominent in $Pt_{0.9}Pd_{0.1}$/SG and $Pt_{0.5}Pd_{0.5}$/SG relative to the other characteristic peaks. There was no elemental sulfur, indicated by the lack of characteristic sulfur peaks. Pt and Pd have the same crystal structure and similar lattice constants, which makes them difficult to distinguish in regular XRD measurements. XPS can be

used to investigate the electronic state of a catalyst material surface, which is a significant factor in the catalytic activity and durability of Pt.[138] **Figure 4-8** displays the full X-ray photoelectron spectroscopy (XPS) spectra of SG, Pd/SG, $Pt_{0.9}Pd_{0.1}$/SG and $Pt_{0.5}Pd_{0.5}$/SG. The C1s peaks for SG are deconvoluted into separate peaks corresponding to sp^2 C=C (284.41 eV), sp^3 C-C (285.82 eV), C=O (287.90 eV) and π-π* (290.65 eV) (**Figure 4-9a**),[139–142] with the results showing that SG largely comprises sp^2 C=C bonds. After deposition of Pt on SG to create $Pt_{0.9}Pd_{0.1}$/SG, the C=C peak is shifted to 284.57 eV and the full width at half maximum (FWHM) increases from 1.0 eV (SG) to 1.29 eV ($Pt_{0.9}Pd_{0.1}$/SG); hence, the broadened peak can be convoluted into another peak at 285.68 eV corresponding to the sp^3 C-C bond (**Figure 4-9b**). The π-π* peak is also negatively shifted from 290.65 eV to 289.25 eV. These differences between SG and $Pt_{0.9}Pd_{0.1}$/SG can be attributed to the interaction between the Pt d orbital and π-π carbon in graphene.

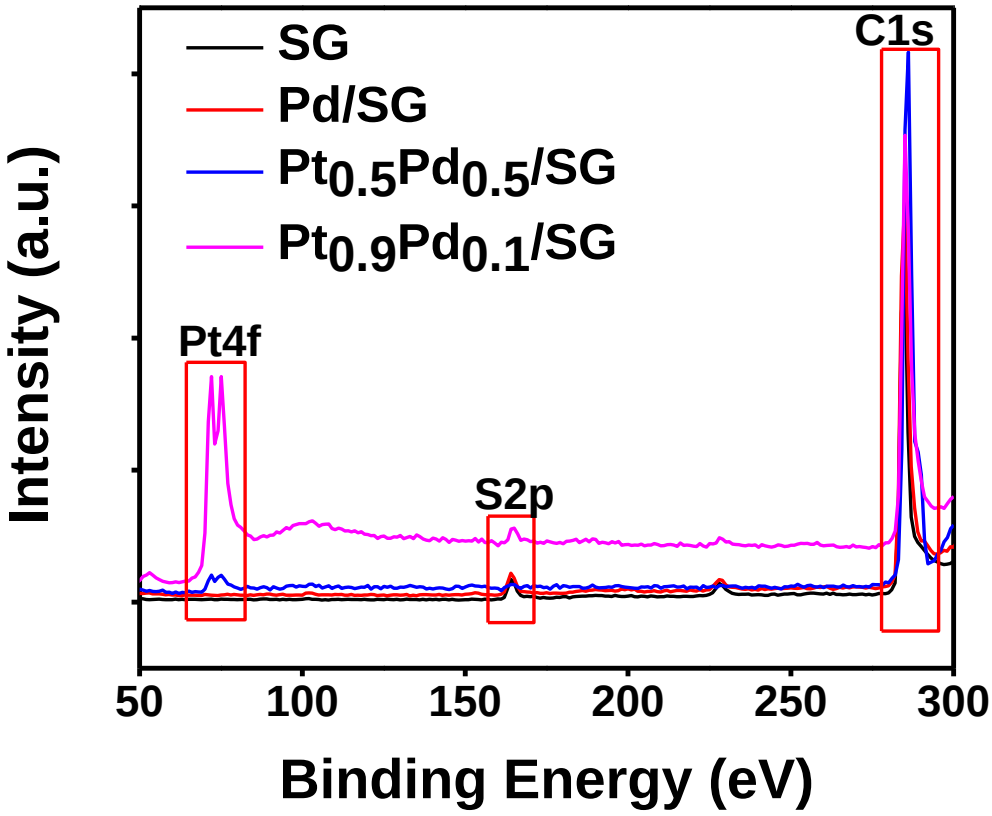

Figure 4-8: Full range high resolution XPS spectra of SG, Pd/SG, $Pt_{0.9}Pd_{0.1}$/SG and $Pt_{0.5}Pd_{0.5}$/SG.

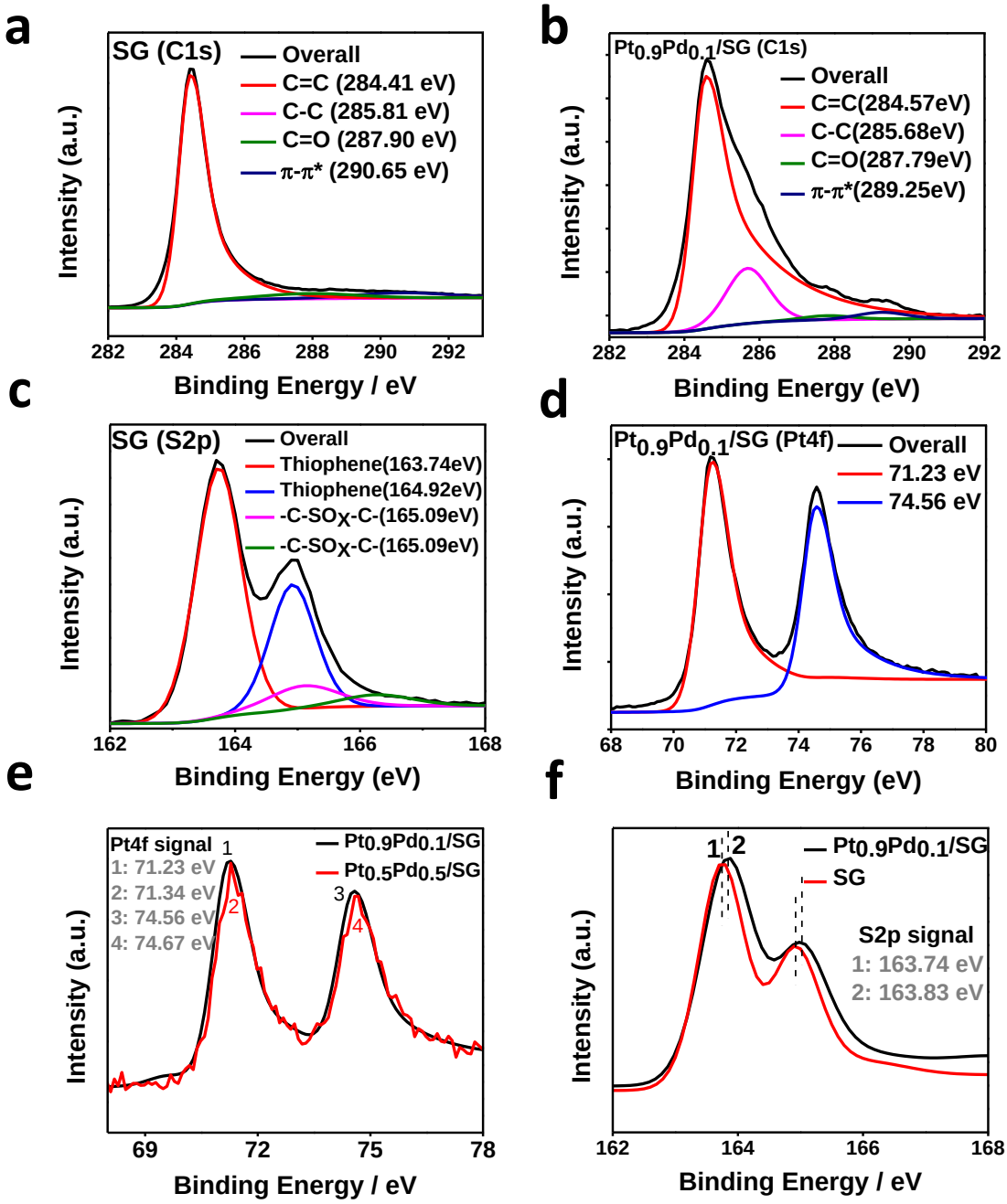

Figure 4-9: Deconvoluted XPS peaks (a) C1s peaks for SG (b) C1s peaks for $Pt_{0.9}Pd_{0.1}$/SG, (c) S2p peaks for SG, (d) Pt4f peaks for $Pt_{0.9}Pd_{0.1}$/SG, (e) Pt4f peaks for $Pt_{0.9}Pd_{0.1}$/SG and $Pt_{0.5}Pd_{0.5}$/SG, (f) S2p peaks in SG and $Pt_{0.9}Pd_{0.1}$/SG.

Table 4-1: Surface atomic concentration of SG as determined by XPS.

Sample	Carbon (at. %)	Sulfur (at. %)	Oxygen (at. %)
SG	92.09	3.77	3.16

The sulfur content of SG is 3.16 at.% (**Table 4-1**), mostly consisting of the thiophenic groups (**Figure S4-9c**). The high-resolution sulfur signal (S2p) was deconvoluted into two major peaks located at 163.74 eV and 164.92 eV and two minor peaks at 165.09 eV and 166.27 eV. The two major peaks resulting from the S2p spin-orbit doublet of the C-S-C bond ($S2p_{1/2}$ at 163.74 eV and $S2p_{3/2}$ at 164.92 eV) were separated by 1.18 eV, which is consistent in value with the theoretical spin doublet separation of 1.13 eV.[143] The two minor peaks can be attributed to carbon bonded with SO_x species (-C-SO_x-).[144,145] Thiophene species incorporate with graphene in a pentagonal configuration, therefore residing at the edge and defected sites of SG. Therefore, sulfur in SG can serve as a platform for anchoring nucleation and growth of Pt ions.[125] In addition to sulfur peak analysis, the fitted Pt $4f_{7/2}$ and Pt $4f_{5/2}$ peaks for $Pt_{0.9}Pd_{0.1}$/SG are observed at 71.23 eV and 74.56 eV respectively (**Figure 4-9d**), while those for $Pt_{0.5}Pd_{0.5}$/SG (50-50% Pt and Pd) are observed at 71.34 eV and 74.67eV, respectively (**Figure 4-9e**). The shift in peaks of 0.11 eV can be attributed to the interaction of Pt and the support material. This is further supported by the positive shift of 0.09 eV of S2p peak from SG to $Pt_{0.9}Pd_{0.1}$/SG (**Figure 4-9f**). It has been previously demonstrated that the interaction of deposited metal on support material plays a vital role in the stability of supported catalysts.[146] The shifting in peaks can be attributed to the sulfur bonding directly with the carbon atoms in the heterocyclic configuration.[147,148]

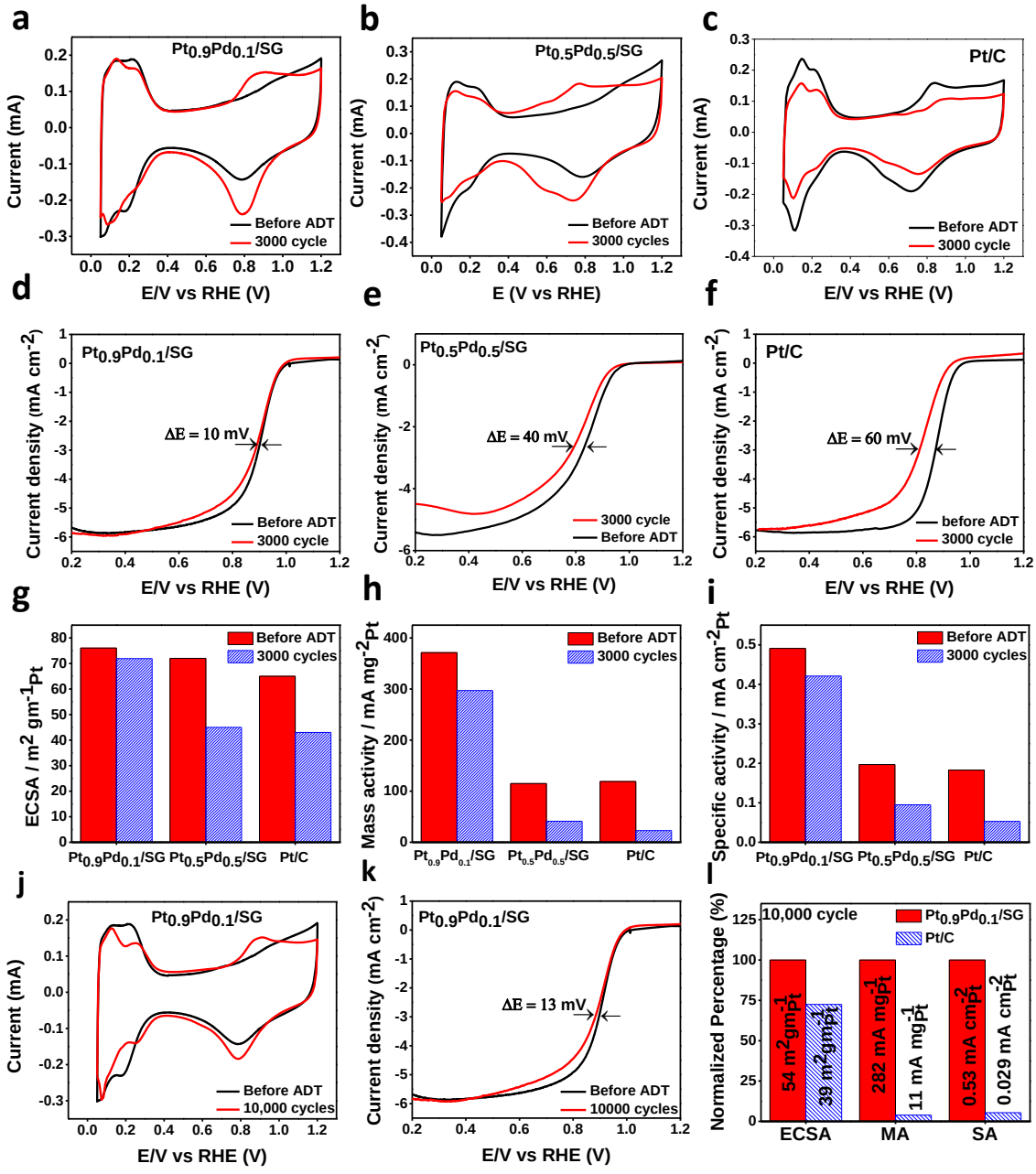

Figure 4-10: Cyclic voltammetry curves for (a) $Pt_{0.9}Pd_{0.1}$/SG (b) $Pt_{0.5}Pd_{0.5}$/SG and (c) Pt/C before and 3000 cycles. ORR polarization curve of (d) $Pt_{0.9}Pd_{0.1}$/SG (e) $Pt_{0.5}Pd_{0.5}$/SG and (f) Pt/C before and after 3000 cycles. (g) ECSA (h) Mass activity and (i) Specific activity bar chart of $Pt_{0.9}Pd_{0.1}$/SG, $Pt_{0.5}Pd_{0.5}$/SG and Pt/C before and after 3000 cycles. (j) CV curves (k) ORR polarization curves (l) Bar chart comparing ECSA, mass activity and specific activity of $Pt_{0.9}Pd_{0.5}$/SG with commercial Pt/C before and after 10,000 cycles.

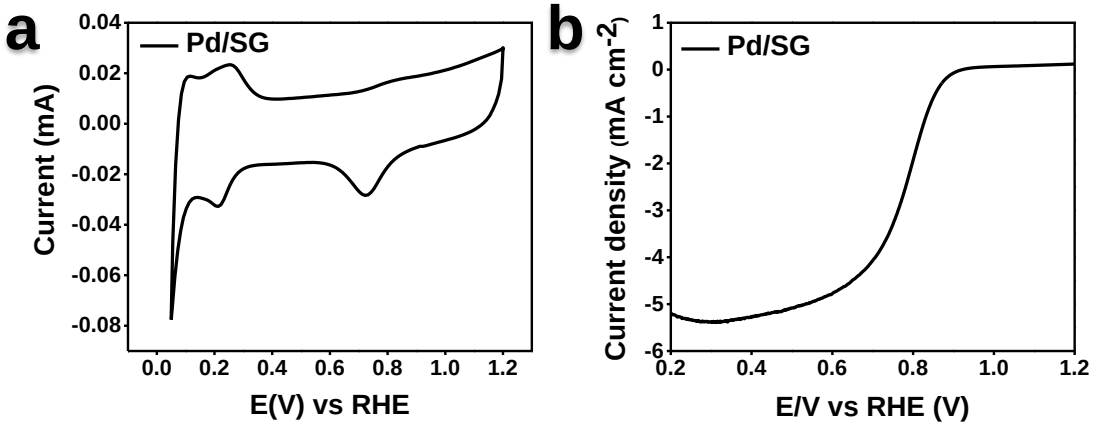

Figure 4-11: (a) Cyclic voltammetry curve and (b) ORR polarization curve of Pd/SG.

To investigate activity and durability, ORR kinetics and accelerated durability testing (ADT) was performed using a rotating disc electrode (RDE) to imitate the harsh, corrosive and potentiodynamic states encountered at the cathode of PEMFCs. **Figure 4-10a-c** shows cyclic voltammograms of $Pt_{0.9}Pd_{0.1}$/SG and $Pt_{0.5}Pd_{0.5}$/SG catalysts together with commercial Pt/C (TKK, 28.8 wt.% Pt). The cyclic voltammograms were performed in N_2-saturated 0.1 M $HClO_4$ solution at a sweep rate of 50 mV s^{-1} in the potential range of 0.05-1.20 V versus a reversible hydrogen electrode (RHE) at room temperature. This range was selected considering Pt dissolution (and subsequent agglomeration) can occur above 0.8 V vs RHE and carbon corrosion occurs above 0.9 V vs RHE.[149–151] The electrochemically active surface area (ECSA) of the catalysts was calculated from the charge associated with the hydrogen desorption peak and normalized with the Pt mass. Before ADT, the specific ECSA of $Pt_{0.9}Pd_{0.1}$/SG and $Pt_{0.5}Pd_{0.5}$/SG are 76 $m^2g^{-1}_{Pt}$ and 72 $m^2g^{-1}_{Pt}$, respectively, which are higher in comparison to the commercial Pt/C (65 $m^2g^{-1}_{Pt}$) (**Figure 4-10g**). Therefore, the fact that Pt-PdNF/SG possesses higher specific ECSA despite 3-4 times larger particle sizes in comparison to commercial Pt/C nanoparticles (2-5 nm) supports the claim that the

dispersion of active Pt surfaces can be improved with larger particles. In this case, the high ECSA of Pt-PdNF/SG can be attributed to its 2D core-shell nanoflower morphology, which includes higher dispersion of the catalyst, planar and porous catalyst morphology and seamless contact between the catalyst and the SG support material. The very small changes in hydrogen adsorption and desorption peaks during ADT and the lack of large oxidative currents at potentials above 1.0 V vs RHE indicates that sulfur oxides released from SG do not have a negative effect on the synthesized materials.[152] For reference, CV behavior and ORR activity of Pd/SG was also investigated (**Figure 4-11**) to show that Pd alone is not sufficient to achieve high electrochemical activity towards ORR. Comparing the double layer capacitance regions of the CV curves before ADT, both Pt-Pd/SG catalysts display higher double later thickness in comparison to Pt/C. It is well known that electrochemical double layer capacitance is affected by the specific surface area, pore structures and surface activity of the support materials. Graphene-based materials possess large surface area and higher capacitance capabilities, and these phenomenon can explain the increase in double layer capacitance.[68,108,135] After ADT, a relatively higher increase of the double-layer capacity under the CV curves was observed for $Pt_{0.5}Pd_{0.5}$/SG (**Figure 4-10b**) in comparison to $Pt_{0.9}Pd_{0.1}$/SG (**Figure 4-10a**). $Pt_{0.5}Pd_{0.5}$/SG undergoes more leaching away of Pd compared to the $Pt_{0.9}Pd_{0.1}$/SG due to the higher initial presence of Pd. This results in higher exposed surface area of highly porous SG, leading to enhanced double layer capacitance.

The ORR polarization curves of the catalysts are shown in **Figure 4-10d-f**. The ORR curves were recorded at room temperature in an O_2-saturated 0.1M $HClO_4$ solution. The kinetic current for each ORR polarization curve was calculated using the Koutechy-Levich equation and

normalized against Pt mass and ECSA for mass and specific activities ($j_{k,mass}$ and $j_{k,specific}$), respectively. Before ADT, the mass and specific activities of $Pt_{0.9}Pd_{0.1}$/SG and $Pt_{0.5}Pd_{0.5}$/SG are significantly improved in the 0.86-0.94 V vs RHE region relative to Pt/C. At 0.9 V vs RHE, the mass activities of $Pt_{0.9}Pd_{0.1}$/SG and $Pt_{0.5}Pd_{0.5}$/SG are 371 mA mg^{-1}_{Pt} and 115 mA mg^{-1}_{Pt}, respectively, with the former representing a 3.12-fold improvement over commercial Pt/C (119 mA mg^{-1}_{Pt}) (**Figure 4-10h**). The specific activities at 0.9 V vs RHE for $Pt_{0.9}Pd_{0.1}$/SG and $Pt_{0.5}Pd_{0.5}$/SG are 0.491 mA cm^{-2}_{Pt} and 0.197 mA cm^{-2}_{Pt}, respectively, with the former representing a 2.71-fold increase over commercial Pt/C (0.183 mA cm^{-2}_{Pt}) (**Figure 4-10i**). The high activities and ECSA of $Pt_{0.9}Pd_{0.1}$/SG could be attributed to the higher exposure of the (111) facets of Pt, which has comparatively better activity than the (100) facet and core-shell structure.[153–155] The addition of Pd to the core-shell structure also lowers its d-band center energy,[156] which provides a weaker Pt-OH_{ads} interaction[157,158] and leads to a decrease in –OH coverage at a given potential and a resulting increase in the number of sites available for O_2 adsorption, dissociation and reduction. Previous work has demonstrated that the vacant d-orbital of individual atoms play a vital role in the catalyst activity and are the basis for excellent catalytic activity.[159] The addition of another metal to the Pt downshifts its d-band center and therefore reduces oxygen binding energy and increases catalytic activity compared to pure Pt.[160–162] Generally, bimetallic structures form weaker bonds with oxygen in comparison with pure Pt, as the variation in oxygen metal bond depends to a large extent on the coupling between the oxygen 2p states and metal 3d states. This leads to a lower position of the d-band center relative to the Fermi level, which affects the metal-oxygen bond interaction and thus benefits ORR activity.[161] In the case of $Pt_{0.9}Pd_{0.1}$/SG, although the

thickness of the Pt shell is relatively high, defects in the core-shell structure can allow for sites where Pd atoms modify the electronic structure of the Pt surface. Moreover, the high mass and specific activity of $Pt_{0.9}Pd_{0.1}$/SG could be associated to its nanoflower morphology, with its well-attached 2D structure providing improved electron transfer kinetics.

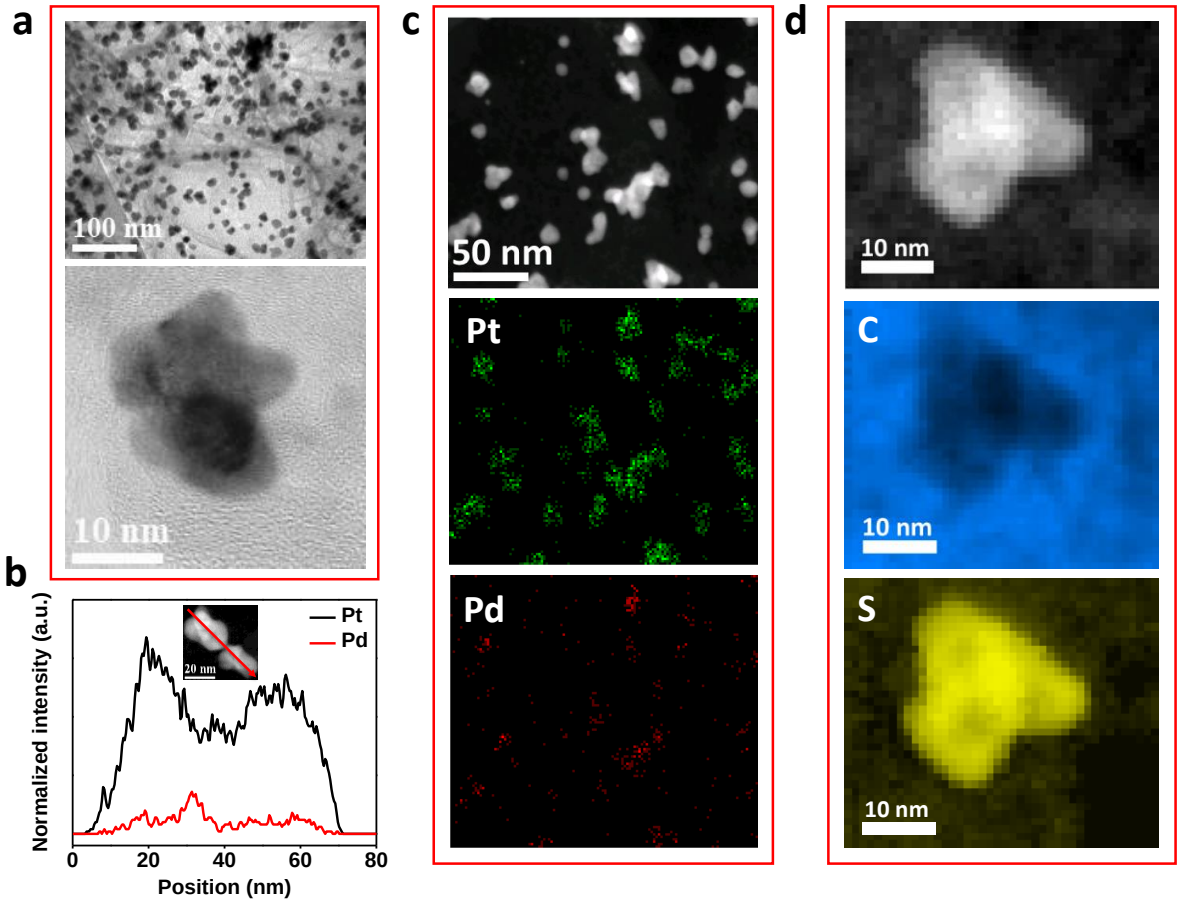

Figure 4-12: (a) TEM and HR-TEM images of $Pt_{0.9}Pd_{0.1}$/SG after 10,000 cycles. (b) EDX line scan profiles of Pt (black) and Pd (red) of two Pt-Pd core shell nanoflower particles after 10,000 cycles. (c) Low magnification HAADF-STEM image and corresponding EDX maps of $Pt_{0.9}Pd_{0.1}$/SG after 10,000 cycles. (d) HAADF-STEM image of $Pt_{0.9}Pd_{0.1}$/SG after 10,000 cycles and corresponding EELS maps of carbon and sulfur.

The electrocatalytic durability of the catalysts were evaluated through accelerated tests applying linear potential sweeps in the range of 0.05-1.2 V vs RHE at a rate of 50 mV s^{-1} in an N_2 saturation 0.1M $HClO_4$ solution at room temperature. After 3000 ADT cycles, $Pt_{0.9}Pd_{0.1}$/SG retains most of its ECSA and ORR activity. The ECSA of $Pt_{0.9}Pd_{0.1}$/SG, $Pt_{0.5}Pd_{0.5}$/SG and Pt/C after 3000 cycles was 72, 45 and 43 m^2 g^{-1}_{Pt} (**Figure 4-10g**), representing decreases of 5%, 38% and 34%, respectively. In terms of catalytic durability after 3000 cycles, the $Pt_{0.9}Pd_{0.1}$/SG only exhibits a 20% loss in mass activity (297 mA mg^{-1}_{Pt}) and 14% loss of specific activity (0.421 mA cm^{-2}), while $Pt_{0.5}Pd_{0.5}$/SG loses 63% (42 mA mg^{-1}_{Pt}) and 52% (0.095 mA cm^{-2}_{Pt}) and commercial Pt/C loses 81% (23 mA mg^{-1}_{Pt}) and 71% (0.053 mA cm^{-2}_{Pt}) of its mass and specific activity, respectively (**Figure 4-10h-i**). Indeed, after 3000 ADT cycles, the mass and specific activities of $Pt_{0.9}Pd_{0.1}$/SG are 13 and 8 times higher than commercial Pt/C, respectively. Even after 10,000 ADT cycles under the same condition (0.05 V-1.2 V vs RHE) (**Figure 4-10j-l**), the specific ECSA of $Pt_{0.9}Pd_{0.1}$/SG (54 m^2 g^{-1}_{Pt}) remains higher than Pt/C after 3000 cycles (43 m^2 g^{-1}_{Pt}) and 10,000 cycles (39 m^2 g^{-1}_{Pt}). Moreover, the mass and specific activities of $Pt_{0.9}Pd_{0.1}$/SG after 10,000 cycles (282 mA mg^{-1}_{Pt} and 0.525 mA cm^{-2}_{Pt}) remain higher than the initial Pt/C activity (119 mA mg^{-1}_{Pt} and 0.183 mA cm^{-2}_{Pt}), and are 25 and 18 times higher than the mass and specific activities of Pt/C after 10,000 cycles (11 mA mg^{-1}_{Pt} and 0.0285 mA cm^{-2}_{Pt}), respectively (**Figure 4-10l**). To further emphasize, $Pt_{0.9}Pd_{0.1}$/SG displays a mass activity loss of only 24% compared to the 91% mass activity loss of commercial Pt/C, which is critically important to the success of prospective ORR catalysts in PEMFCs. The durability of $Pt_{0.9}Pd_{0.1}$/SG, given the aggressive ADT potential range (0.05-1.2 V

vs RHE) used in this work in comparison to other recent Pt-based catalyst reports, is particularly impressive.[61,108,135,163]

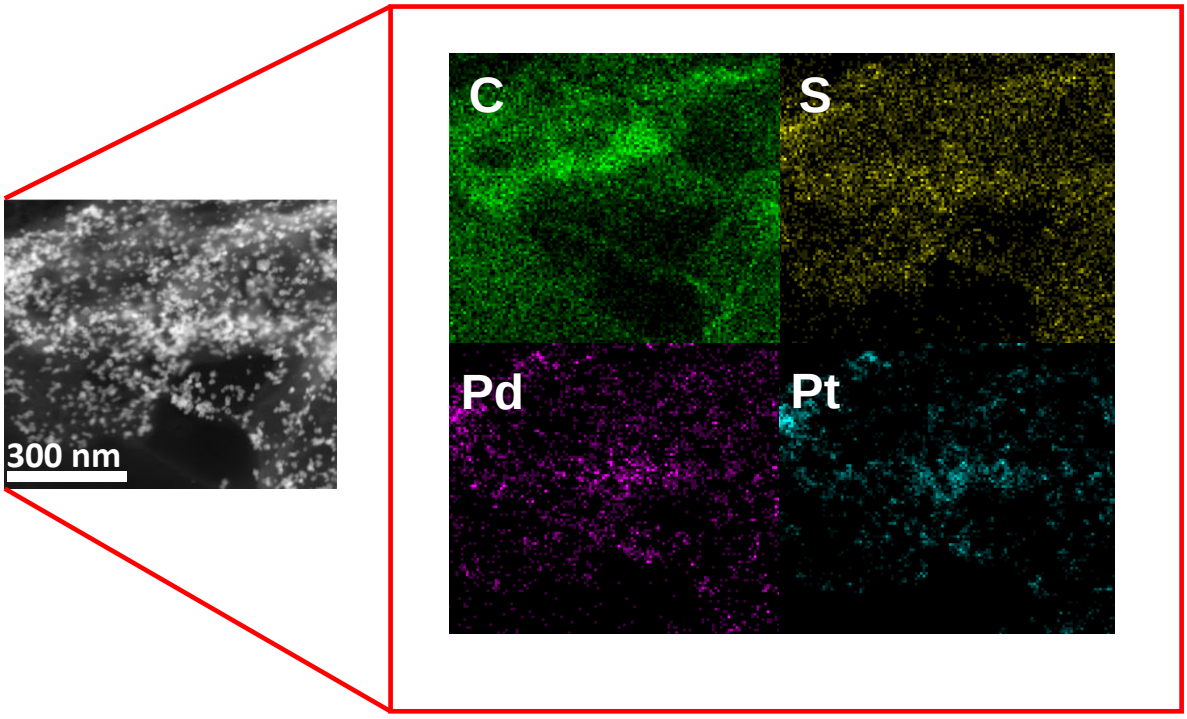

Figure 4-13: Overview TEM EDX mapping of $Pt_{0.9}Pd_{0.1}$/SG after ADT (10,000 cycles).

The exceptional stability of $Pt_{0.9}Pd_{0.1}$/SG is partly attributed to its high graphitic content, the core-shell nanoflower architecture of Pt-Pd and the presence of functional anchoring groups and strong interactions between SG and Pt.[135] Additionally, the Pd core delivers long term stability to the Pt shell layer, since Pd has a lower oxidation potential (0.92 V vs RHE) than Pt (1.19 V vs RHE), therefore preventing the cathode potential reaching a value where Pt oxidation can take place.[119] Since it is difficult to synthesize a pore-free Pt shell, the Pd core will establish contact with the electrolyte and gradually oxidize when the potential rises above its oxidation potential. Oxidized Pd^{+2} will subsequently diffuse through any pores in the Pt shell, leaving empty space in

the core. After prolonged potential cycling, the empty space left causes the Pt shell to undergo small contractions and become even less reactive.[156] Therefore, the Pd core increases the stability of the Pt shell by inducing lattice contractions and by acting as a sacrificial anode to provide cathodic protection to the Pt shell. Evidence of this protection mechanism is provided by post-cycling TEM analysis.

After 10,000 ADT cycles, $Pt_{0.9}Pd_{0.1}$/SG was removed from the glassy carbon electrode by rinsing in ethanol and analyzed with TEM to search for the presence of agglomeration or dissolution of Pt particles, and any other catalyst morphological changes. The Pt-Pd particles remained well-dispersed on SG, while no significant agglomeration or overall changes in its morphology were observed (**Figure 4-12a**). However, in comparison to the catalyst before cycling (**Figure 4-3f**), the EDX line spectra in **Figure 4-12b** shows a clear decrease of Pd intensity relative to the Pt intensity, thus demonstrating that Pd indeed dissolves during cycling due to defects in the core-shell structure. However, it should be noted that part of Pd remains after ADT testing. This can be attributed to the parting limit, where higher atomic ratio of the more noble component (Pt in this case) diminishes dissolution of the other or both metals in a binary systems.[164] EDX elemental mapping of individual nanoflowers in $Pt_{0.9}Pd_{0.1}$/SG shows the retention of the Pd core-Pt shell structure after ADT (**Figure 4-12c**), while mapping at lower magnification shows the homogenous distribution of carbon, sulfur, Pt and Pd is also maintained (**Figure 4-13**). EELS elemental mapping (**Figure 4-12d**) shows that sulfur stays concentrated at the edge of core-shell nanoflower catalyst, indicating the interaction between sulfur and Pt remains after ADT.

4.4 Conclusion

In summary, we have designed and synthesized a novel ORR catalyst composed of Pt-Pd core shell nanoflower-like structures deposited on sulfur-doped graphene. The core-shell nanoflower structures exhibit a substantial enhancement in electrochemical activity and remarkable long-term stability compared with commercial Pt/C. After 3000 ADT cycles, the $Pt_{0.9}Pd_{0.1}$/SG catalyst retains 80% and 86% of its mass and specific activity, respectively, while Pt/C only retains 19% and 28%. Even after longer-term ADT (10,000 cycles), the mass activity of $Pt_{0.9}Pd_{0.1}$/SG was 2.4 times higher than the initial activity of Pt/C, demonstrating its exceptional stability. Through the combination of a unique SG support and nanostructured 2D core-shell structure, this work provides an attractive strategy for obtaining excellent catalyst performance and durability to overcome the performance barriers of traditional PEMFC cathodes electrocatalyst.

Chapter 5: Space-confined catalyst design towards ultrafine Pt nanoparticles with enhanced oxygen reduction activity and durability

5.1 Background Information

Polymer electrolyte membrane fuel cell (PEMFC) is a promising sustainable clean energy system to meet global energy demands.[165,166] Commercial PEMFC uses platinum-based catalysts which are best available to catalyze sluggish oxygen reduction reaction (ORR).[150] Since only the surface Pt atoms are assessible to the reactants, catalytic activity of platinum nanoparticles greatly depends on their particle size. Where decrease in size increases catalytically active surface area due to enhanced surface area/volume ratio. Given this, intensive efforts are devoted in developing platinum-based catalysts with smaller particle size towards large electrochemical surface area (ECSA, $m^2.g^{-1}_{Pt}$) and mass activity (MA, $A.mg^{-2}_{Pt}$).[98,138,150,156,158,167–170] In fact, the state-of-the-art Pt/C catalyst are supported platinum nanoparticles with an average size of ~3 nm. However, the catalytic activity of the commercial Pt/C catalysts still can't meet the requirement for their widespread implementation, which calls for further decreasing the particle size, yet remains a big challenge due to the lack of effective synthetic strategies.[18,19,21] Besides, smaller Pt nanoparticle are even more susceptible to sintering and detachment from the support surface leading to rapid deterioration in catalytic activity.[23] Stability of oxygen reduction catalyst in PEMFC is at forefront limiting their commercialization.[151] State-of-the-art Pt/C catalyst are prone to platinum dissolution,

Ostwald ripening and platinum agglomeration at the working condition.[28,29,171,172] Particles migrate on the support surface follow Brownian movement due to relatively weak support-metal interaction. While Ostwald ripening lead to particle agglomeration as large particle grows on the expense of smaller one due size dependent surface energy.[28,31] High surface energy associated with smaller particle lead to easy migration and agglomeration, becomes more problematic due to unsaturated coordination and leads to spatial electron delocalization.[32,58,173] Agglomeration and dissolution of Pt nanoparticle on the surface of carbon material becomes more severe during start/stop of fuel cell operation and diminishes fuel cell performance.

To reduce the catalyst degradation scientific work has been fostered on discovering new more efficient catalyst material and methodologies to upgrade catalyst arrangement within structure.[174] The most widely used approach to improve durability is use of different carbon support with higher anti-corrosion ability such as CNT[60,90,175], graphene[176,177]. However, the well-crystallized carbon structure makes it difficult to deposit platinum nanoparticles uniformly on the support, which is unfavorable for long-term durability as the catalysts with uniform size, shape and distribution are proven to minimize driving force for Ostwald ripening or agglomeration.[30,178] Another approach is strengthening metal support interaction which can suppress particle free migration on the surface, therefore suppress coalescence and detachment of catalyst nanoparticles from the surface.[95,100,179] However, metal-support interaction on the surface are still vulnerable to agglomeration and dissolution. Therefore, precise control of Pt nanoparticle is an immense challenge and even with successful synthesis of small nanoparticles are prone to agglomeration and dissociation from support surface. Taking these points into consideration, the most promising

approach to precisely control size and stabilize small nanoparticles is by incorporating inside well-defined nanopores or crystalline matrices. Regardless of potential of seeding or embedding of nanoparticles within nanopores of host materials, one of the major challenges is how to channelize the Pt precursor inside pore. In fact, seeding of nanoparticles do not assure high ORR activity and durability as mass transfer limitations and reaction kinetics need to be excellent within pore of host materials.

In this work, we have developed a facile one-step strategy, which is easy for adaptation in scale-up production and duplication, to seed Pt nanoparticles inside the carbon support nanopore towards improved ORR intrinsic activity and stability. This strategy helps in controlling nucleation of ultrafine Pt nanoparticles inside pores and pore-confinement effect assists to synthesize uniform nanoparticle distribution. As a proof-of-concept, commercial KJ600 was selected as a model support material due to large surface area, high porosity with interconnected channels and high conductivity. The synthesized catalyst (Pt_{inside}/KJ600) exhibits 0.558 A mg^{-1} Pt mass activity at 0.9 V vs RHE, which is about 3.20 times higher than commercial carbon supported Pt catalyst (Pt/C) and exceeds the DOE 2020 targets. Remarkably high ECSA and mass activity confirms large number of catalytic active sites and indicate no mass transfer or reaction kinetics limitations due to seeding Pt nanoparticle inside pores. High ORR catalytic activity is a proof of concept that Pt seeding inside pores do not impede mass transfer and reaction kinetics. Besides, the as-developed Pt_{inside}/KJ600 shows dramatically improved long-term stability, as after 20K cycle mass activity of Pt_{inside}/KJ600 was 6 times higher than Pt/C catalyst, and even 2.20 times higher than

initial activity of Pt/C. The enhanced stability is predominately attributed to pore confinement effect, which reduces the particle dissolution and agglomeration by keeping Pt nanoparticle intact.

5.2 EXPERIMENTAL SECTION

5.2.1 Synthesis of Pt_{inside}/KJ600 and $Pt_{outside}$/KJ600 catalyst:

The Pt based catalyst was prepared by depositing Pt on carbon material KJ600 (Ketjen black EC-600JD, AkzoNobel). For Pt_{inside}/Kj600 catalyst synthesis, first the KJ600 was sonicated for 2 hours in deionized water and Ethanol (Anhydrous ethyl alcohol, Sigma-Aldrich). The 100 mM $H_2PtCl_6.6H_20$ was added to the support material and later Pt concentration was confirmed with ICP analysis. In a typical synthesis procedure, 50 mg of KJ600, 1ml of 100 mM of $H_2PtCl_6.6H_20$ and anhydrous ethanol was mixed. The Pt precursor carbon solution was sonicated for 2 hours and followed with overnight vacuum drying. While in case of $Pt_{outside}$/KJ600 catalyst, KJ600 was sonicated for 2 hours in large volume of deionized water to obtain uniform KJ600-DDI mixture. Then, Pt precursor solution was added and stirred rigorously for 2 hours to obtained uniform mixture. Subsequently, temperature was raised on stirred plate to slowly vaporized DDI water and final product was further vacuum dried for overnight. Platinum particle was reduced by heat treatment for 2 hours at 400 ºC in 10 % H_2/Ar environment. The flow rate of carrier gas was maintained at 100 sccm throughout the experiment. Final product was collected from furnace and used as it is for further physiochemical and electrochemical characterization.

5.2.2 Physiochemical characterization:

Powdered X-ray diffraction patterns was obtained using Rigaku MiniFlex X-ray diffractometer, with a scan rate of 1º per minute, and at a step size of 0.02 degree. Elemental composition percentage of material was determined by the inductively coupled plasma atomic emission spectroscopy (710-ES, Varian, ICP-OES). Elemental electronic configuration was determined by X-ray photoelectron spectroscopy (XPS) from Thermo Scientific K-Alpha spectrometer. Surface area and pore volume analysis was performed on ASAP 2020 Plus unit based on Brunauer-Emmett-Teller theory. Transmission electron microscopy (TEM), High-resolution TEM (HR-TEM), High-angle annular dark field microscopy (HAADFM), scanning transmission electron microscopy (STEM), and energy-dispersive X-ray (EDX) elemental mapping was performed using JOEL 2100F operated at 200 kV and Hitachi HD2700C STEM equipped with a probe aberration corrector operated at the 200 kV.

5.2.3 Electrochemical characterization:

Electrochemical characterization tests were conducted on the three electrode testing cells in 0.1 M $HClO_4$ solution at room temperature using Bio-Logic VSP electrochemical station. Glassy carbon electrode was used to deposit synthesized catalyst and was working electrode, reversible hydrogen electrode (RHE) was used as a reference electrode, and platinum foil was used as a counter electrode. Catalyst ink was prepared with deionized water, Iso-propanol (v/v=1:1) and 5 wt % Nafion solution and deposited on the glassy carbon electrode with active surface area of 0.196 cm^2. All potential in this manuscript is referred in the term of RHE potential. The Pt loading was calculated based on the ICP results and was consistent throughout catalyst used in this work. Catalyst activation was performed using cyclic voltammetry in a potential range of 0.05-1.05 V vs

RHE at a scan rate of 20 mV s^{-1} in 0.1 M $HClO_4$ saturated with N_2 gas. Electrochemical active surface area (ECSA) was determined by integrating H_2 adsorption/desorption region between 0.05 to 0.4 V vs RHE for reverse sweep, and a charge density of 210 μC cm^{-2} for hydrogen adsorption on monolayer of polycrystalline platinum in cyclic voltammetry. Linear sweep voltammetry (LSV) was used to capture ORR polarization curve in O_2-saturated 0.1 M $HClO_4$ solution at the scan rate of 10 mV s^{-1} at the rotation speed of 1600 rpm. The ORR polarization curve was used to calculate mass activity. Durability test was performed between potential range of 0.6-1.1 V vs RHE at a sweeping rate 50 mV s^{-1}. To compare results presented in this work Pt/C (TKK, 28.8%) was used as the baseline catalyst at same measuring conditions. Elemental composition based on the ICP results was used for the calculation of ECSA and mass activity.

5.3 Result and Discussion

The synthesis method developed for this work was facile one-step which includes sonication to obtain uniform mixture and reduction at low temperature to control particle size. Detailed synthesis procedure is presented in the material and methods section. This facile method possesses multiple advantages over their counterparts, such as reduction at high temperature which leads to the large growth of particle size. Some processes uses various capping and reducing agent which require the washing or other treatment to remove any unwanted element otherwise will have a detrimental effect on the performance of catalyst[180], or solvothermal methods demands removal of organic solvents and affects synthesis efficiency qualitatively and quantitatively.[61,135] Therefore, abandoning organic solvent, reducing agent, capping agent or any other chemical reagent during

synthesis minimized constraints and led highly repeatable and efficient synthesis route. Solvent volume and its polarity were tuned to maneuver the seeding of platinum inside nanopore and on surface of carbon support. Platinum precursor in ethanol with Ketjen Black EC600JD (KJ600) was sonicated to maneuver the Pt inside nanopore of carbon material, as adsorption of ethanol target nucleation site inside the carbon nanopores. After sonication ethanol was removed in vacuum oven and form the basis of Pt seeding inside the nanopores. Further annealed in H_2 environment led to nucleation and Pt particle growth. The catalyst through ethanol route called Pt_{inside}/KJ600 as platinum nanoparticle was seeded inside nanopore of KJ600. While same procedure was repeated with large volume of DDI with stirring instead of sonication to deposited Pt nanoparticle on the surface of carbon support ($Pt_{outside}$/KJ600). Wettability of DDI is lower on carbon support (KJ600), therefore non-selective deposition take place, while higher in case of ethanol and when coupled with sonication it helps in diffusion of Pt precursor solution inside nanopore. Overall synthesis route and schematic illustration of Pt nanoparticles inside pores are presented in schematic diagram (**Figure 5-1**).

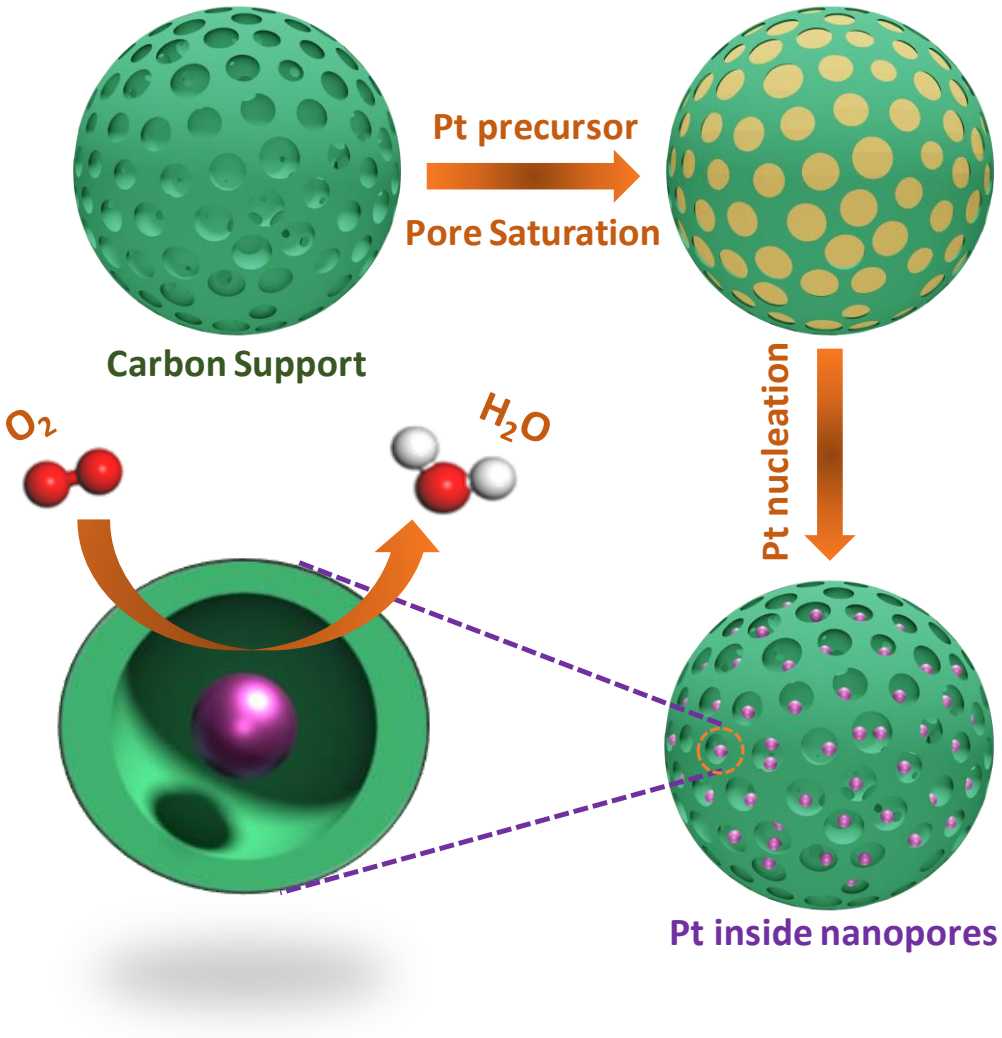

Figure 5-1: Schematic illustration of the synthesis route of Pt_{inside}/KJ600 catalyst.

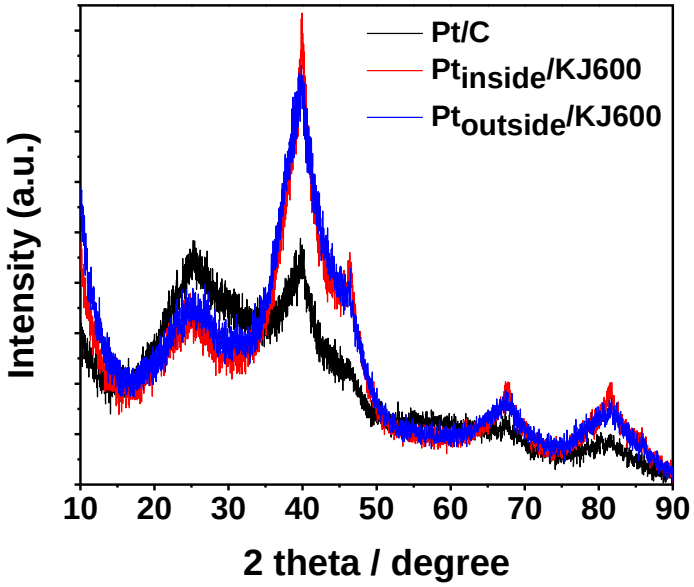

Figure 5-2: Full range XRD peak of Pt_{inside}/KJ600 and $Pt_{outside}$/KJ600 and of Pt/C.

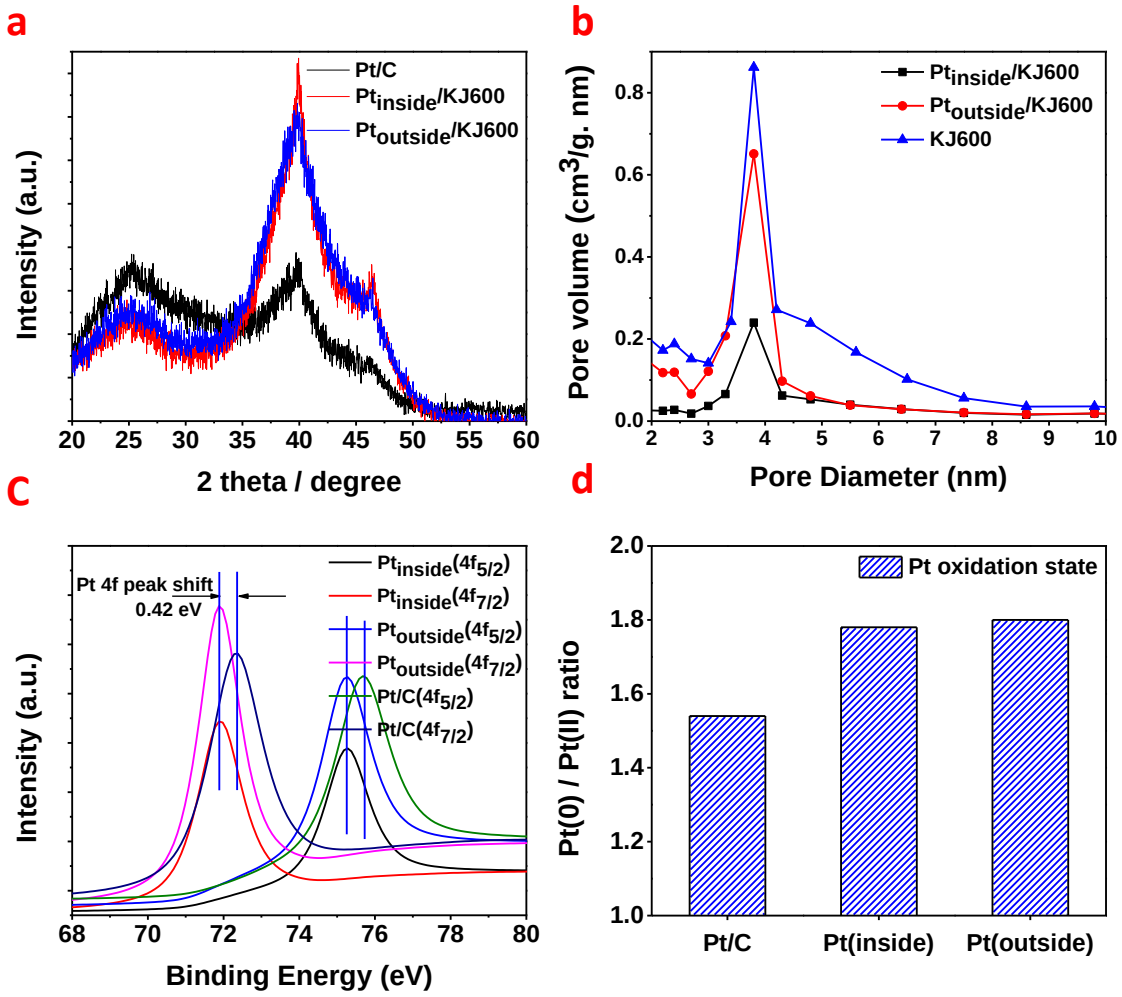

Figure 5-3: (a) XRD pattern, (b) BJH pore-size distribution of KJ600, Pt_{inside}/KJ600 and $Pt_{outside}$/KJ600, (c) Pt4f high-resolution XPS spectra of Pt_{inside}/KJ600, $Pt_{outside}$/KJ600 and Pt/C, (d) Pt(0)/Pt(II) oxidation state ratio in XPS spectra of Pt_{inside}/KJ600, $Pt_{outside}$/KJ600 and Pt/C.

Powdered X-ray diffraction (XRD) was used to identify the phase of crystal material, crystal size and characterize lattice parameters of the synthesized catalyst materials. The characteristic peaks of Pt was obtained at 39.6, 46.2, 67.38 and 81.34 degree, and correlated with Pt(111), Pt(200), Pt(220) and Pt(311) crystal phase respectively (**Figure 5-2, 5-3a**). These crystal planes observed in XRD curve indicate typical face-centered cubic (fcc) structure. There was no

significant difference observed in Pt peaks position of different catalyst synthesized in this work. The Pt particle size based on the XRD data was calculated using Scherrer equation and was observed in range of 2-3 nm. As per Scherrer equation, peak width is inversely proportional to the crystallite size. Relatively smaller particle size possesses more catalytic active surface, and relatively higher activity and vice-versa. XRD peaks were obtained and compared for the Pt deposited outside and inside of the KJ600 (**Figure 5-3a**). Average crystal domain size of Pt along the (111) direction from XRD peak was 2.43 nm when Pt nanoparticle was deposited on the surface ($Pt_{outside}$/KJ600), while 1.63 nm when Pt was seeded inside pores (Pt_{inside}/KJ600). Herein, the differences in size of Pt nanoparticle can be attributed to confinement of Pt particle inside the pores as both catalysts have undergone same heat treatment and reduction conditions. Only difference was the use different volume of solvent for the seeding of Pt nanoparticle inside the pores. It should be noted that, both the $Pt_{outside}$/KJ600 and Pt_{inside}/KJ600 exhibit smaller Pt size than the commercial Pt/C (2-5 nm) (**Figure 5-3a**), demonstrating the superiority of reduction method adapted in this work. Apart from the typical diffraction peaks for fcc Pt, comparatively broad peak around 25 degree corresponds to carbon characteristic peaks along (002) plane[181] was observed for both catalysts and commercial Pt/C, with higher intensity for Pt_{inside}/KJ600 and $Pt_{outside}$/KJ600 compared to Pt/C (**Figure 5-2a**). The higher intensity corresponds to higher graphitic crystallinity of KJ600 a positive trait to improve ORR stability.[182,183]

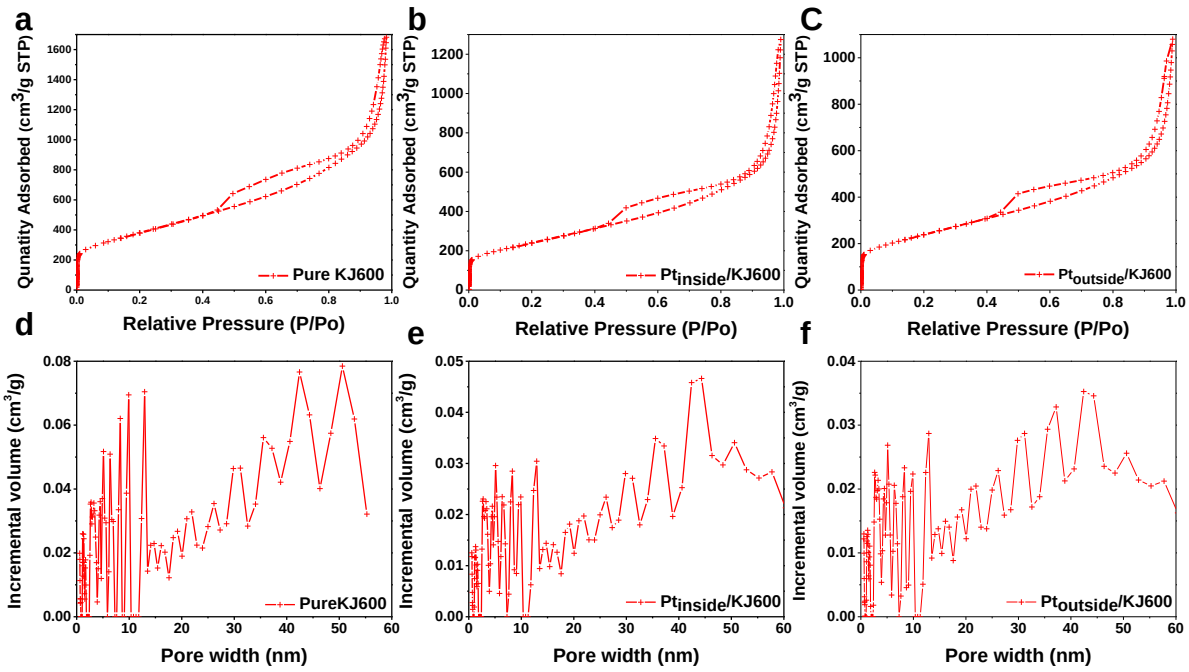

Figure 5-4: (a-c) N_2 adsorption desorption isotherm, (d-f) pore-size distribution isotherm of KJ600, Pt_{inside}/KJ600 and $Pt_{outside}$/KJ600.

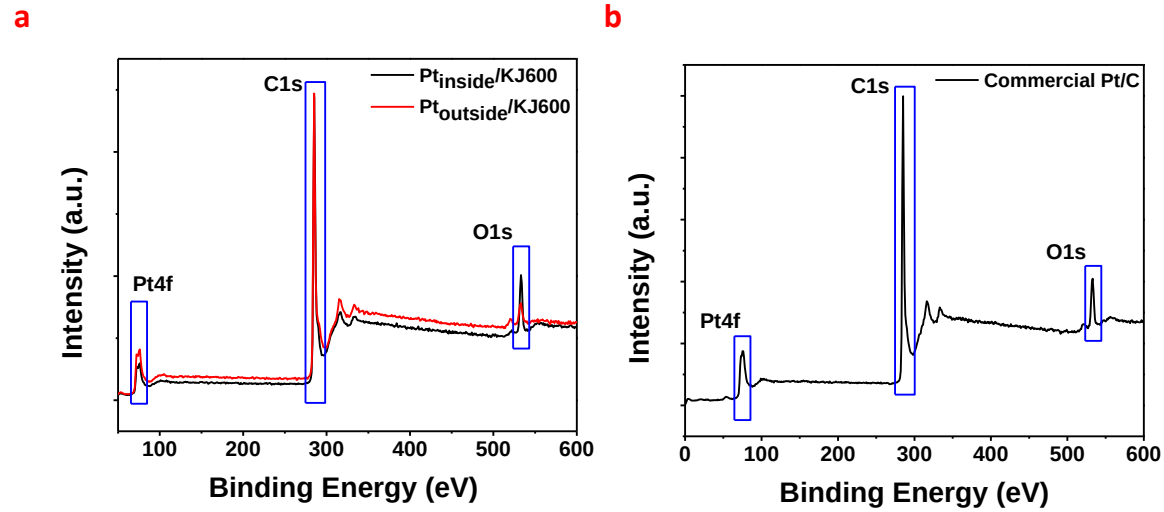

Figure 5-5: (a) Full range high-resolution XPS spectra of Pt_{inside}/KJ600 and $Pt_{outside}$/KJ600, (b) Full range high-resolution XPS spectra of Pt/C.

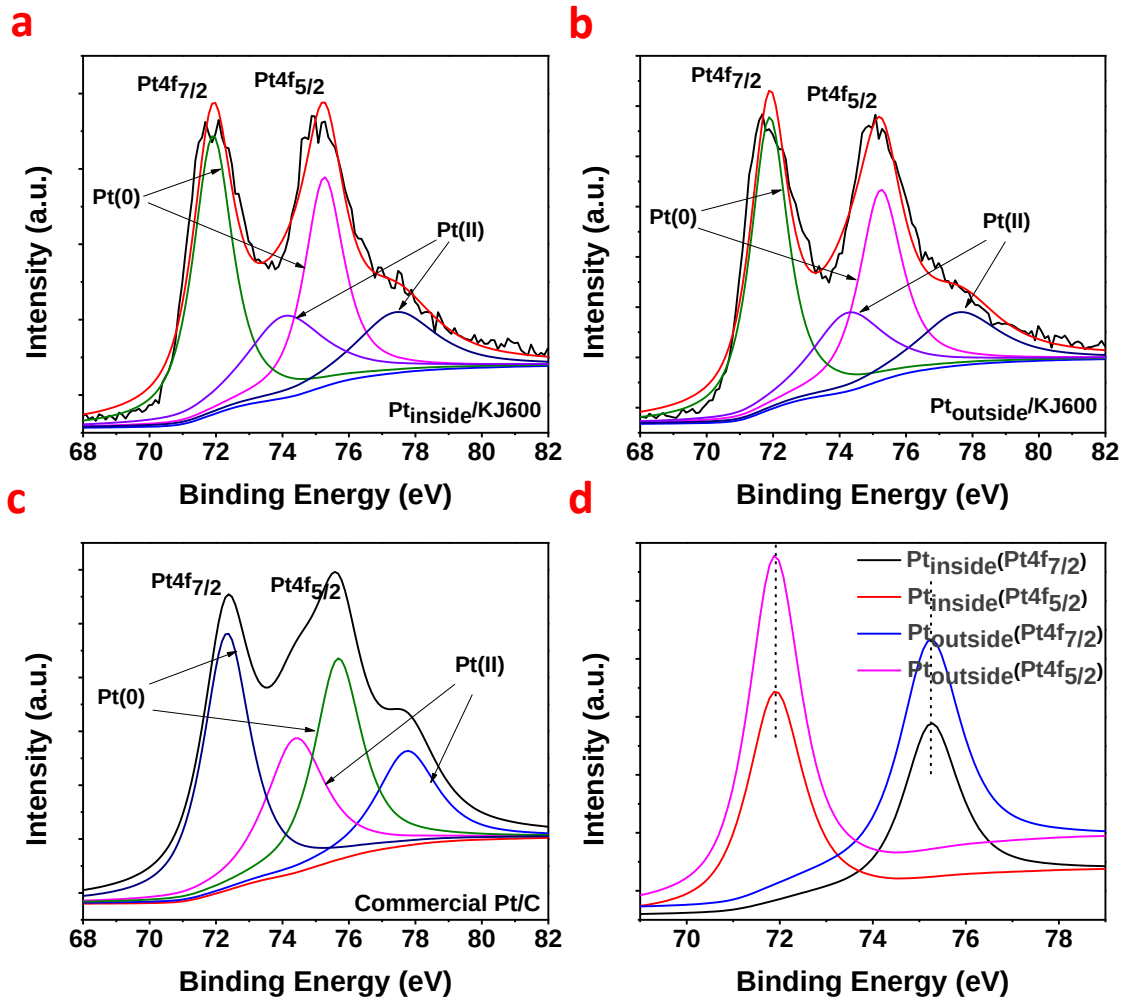

Figure 5-6: High-resolution XPS spectra comparison of Pt4f peaks of Pt_{inside}/KJ600 and $Pt_{outside}$/KJ600 samples.

Since the porosity of the carbon support material not only correlates with the mass transfer of electrocatalytic reactions, but also reflects the dispersion of the supported metal nanoparticles, pore characterization of carbon support material and catalysts was investigated by N_2 adsorption and desorption methods. Surface area and pore volume was estimated with BET analysis, while pore-size distribution was calculated through Barrett, Joyner and Halenda (BJH) models (**Figure 5-4**). As displayed in **Figure 5-4**, a typical type-IV isotherm shows a characteristic H3 hysteresis

loop which reveals a mixture of both micro-mesoporous nature of support material KJ600. It is also worth mentioning that from pore size distribution plot, the diameter of most pores falls in the range of 2 to 5 nm KJ600, which is large enough for easy diffusion of Pt precursor inside nanopores of carbon support.[184] BET surface area of carbon support was estimated as 1362.47 m^2 g^{-1}, and retained high values after Pt deposition with 850 m^2 g^{-1} when Pt was deposited inside nanopore, while 860.36 m^2 g^{-1} when Pt was deposited on the surface of support material. Herein, large porosity and surface area are favorable for high density of active sites and can be easily access to large volume of reactant and ultimately favorable condition for high electrocatalytic performance The pore volume of KJ600 was 2.59 cm^3/g and decreased to 1.61 cm^3/g for Pt_{inside}/KJ600，implying partial filling of nanopores as a result of Pt deposition. **Figure5-3b**, shows BJH pore-size distribution of KJ600, $Pt_{outside}$/KJ600 and Pt_{inside}/KJ600. There was a stern decrease in peak area and narrow pore-size distribution is noticeable in case of Pt_{inside}/KJ600 when compared with KJ600 and $Pt_{outside}$/KJ600, with no shift in peak position of pore-size distribution plot observed. These evidences strongly suggest confinement of Pt particle inside pores and that led to the effective immobilization of Pt nanoparticles. Diffusion Pt precursor solution assist in seeding of Pt precursor inside pores and followed with nucleation and Pt nanoparticle formation. Therefore, data extracted in case of Pt_{inside}/KJ600 from BET analysis clearly indicate diffusion, seeding and nucleation of Pt nanoparticles within nanopores of KJ600.

X-ray photoelectron spectroscopy (XPS) was conducted to further investigate the elemental composition and electronic configuration of synthesized catalysts. Full range XPS spectra of Pt_{inside}/KJ600, $Pt_{outside}$/KJ600 and Pt/C catalysts are displayed in **Figure 5-5**. The high-resolution

Pt 4f XPS of Pt_{inside}/KJ600, $Pt_{outside}$/KJ600 and Pt/C can be deconvoluted into atomic Pt(0) and oxidized Pt(II) as presented in **Figure 5-6(a-c)**. $Pt4f_{7/2}$ and $Pt4f_{5/2}$ peaks were observed at 71.88 and 75.28 eV separated with 3.35 eV within catalyst for Pt_{inside}/KJ600 and $Pt_{outside}$/KJ600 respectively (**Figure 5-6d**). Although there was no shift in peak position observed between Pt_{inside} and $Pt_{outside}$ catalyst, while a significant negative shift of 0.42 eV in peak position was observed when compared with Pt/C, attributed to strong metal-support interaction in synthesized catalysts (**Figure 5-3c**).[185] Strong-metal support interaction promisingly leads to higher intrinsic activity and eventually increase in ORR electrocatalytic activity.[186] Besides, the ratio of Pt(0)/Pt(II) was calculated for Pt_{inside}/KJ600, $Pt_{outside}$/KJ600 and Pt/C and presented in **Figure 5-3d**. Ratio of metallic Pt(0) to oxidized state Pt(II) peak area ratio at initial condition for both catalysts Pt_{inside}/KJ600 and $Pt_{outside}$/KJ600 is almost similar, which suggests same number of active sites as only metallic Pt atoms are active towards ORR.[187,188] Notably, the Pt(0)/Pt(II) ratio is higher for Pt_{inside} and $Pt_{outside}$ compared to Pt/C, probably contributing towards higher ORR activity. Higher intensity of Pt peaks in $Pt_{outside}$/KJ600 as compared to Pt_{inside}/KJ600 can also indirectly suggest seeding of Pt inside pore since XPS only detects surface Pt (**Figure 5-6d**).

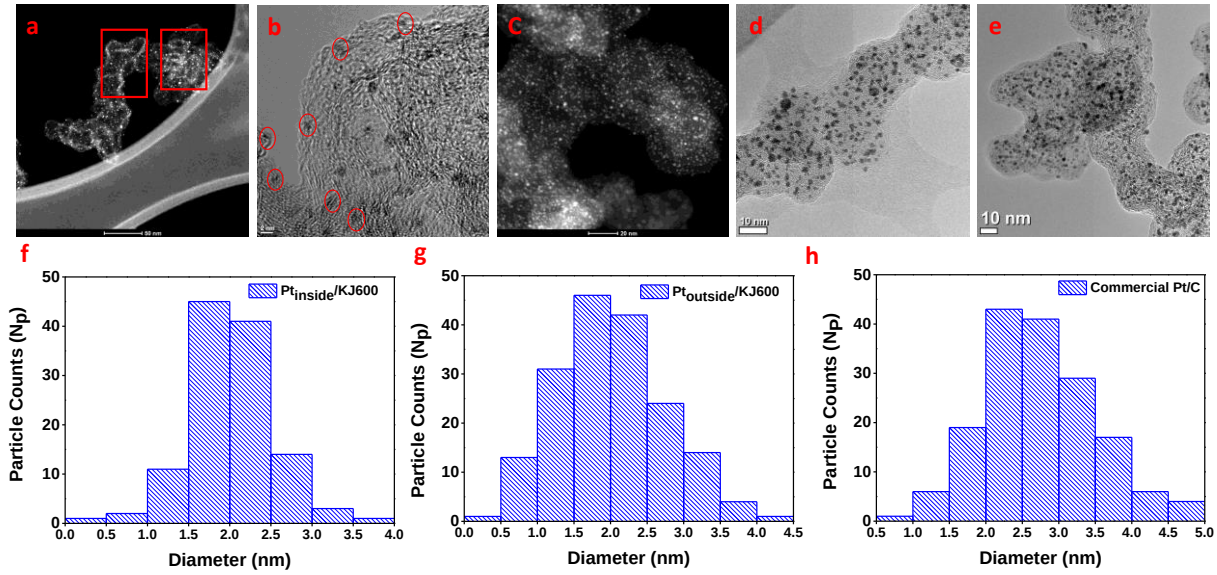

Figure 5-7: (a) HAADF image, (b) HR-TEM image of Pt_{inside}/KJ600, (c) HAADF image, (d) TEM image of $Pt_{outside}$/KJ600, (e) HR-TEM image of Pt/C, Particle size distribution of (a) Pt_{inside}/KJ600, (b) $Pt_{outside}$/KJ600 and (c) Pt/C respectively.

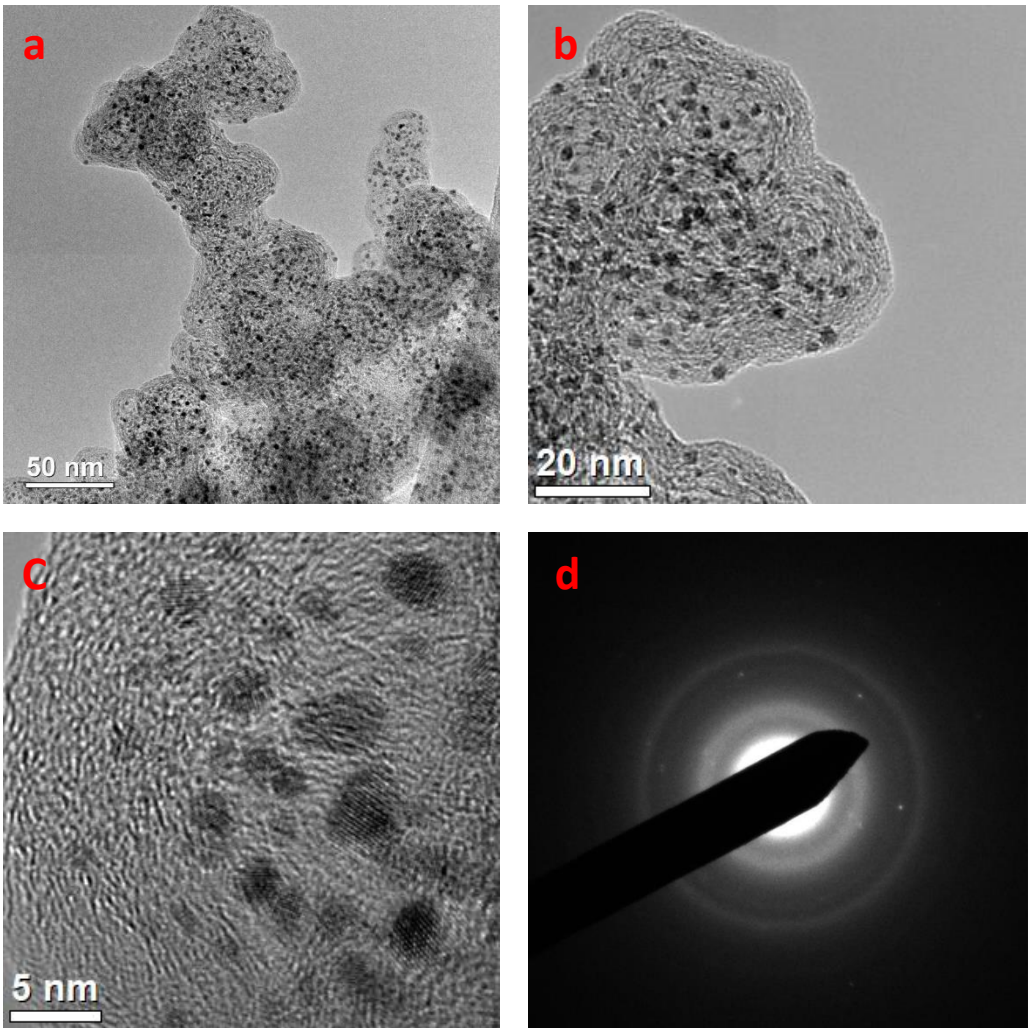

Figure 5-8: TEM images of Pt/C.

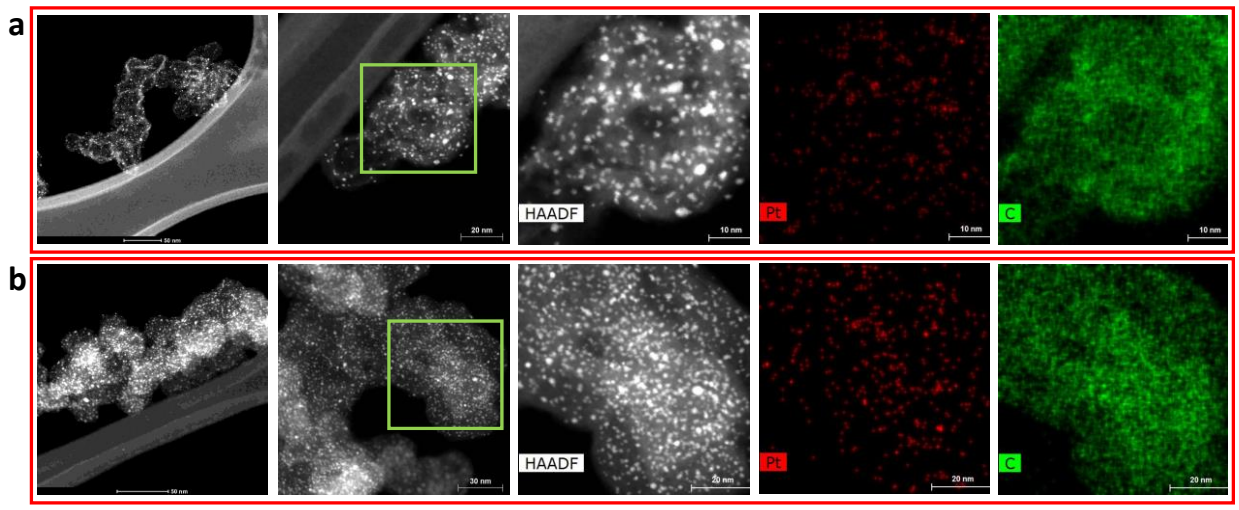

Figure 5-9: (a) HAADF image and EDS mapping of Pt_{inside}/KJ600, (b) HAADF image and EDS mapping of $Pt_{outside}$/KJ600.

Platinum particle size with XRD, their electronic configuration with XPS and with BET results have established the nanoparticle within pores. To further compliment these we looked at the morphology with TEM results and performed particle size distribution. Pt nanoparticle of uniform size was found to be homogeneously distributed over the carbon nanopores (**Figure 5-7a-b**). High angle annular dark field scanning transmission electron microscopy (HAADF-STEM) image and HR-TEM image for Pt_{inside}/KJ600 shows the uniform distribution of Pt nanoparticles (**Figure 5-7a-b**). Nanoparticles appears on the peripheral and can be clearly visualized and correlated in schematic diagram (**Figure 5-1**). The uniform dispersion without agglomeration can be attributed to pore-confinement effect on Pt nanoparticles. Overview HR-TEM image of Pt_{inside}/KJ600 is shown in **Figure 5-7b**, when consider it as top view you can clearly see Pt nanoparticle homogeneously embedded inside carbon material (in oval shaped marked box). Whereas, $Pt_{outside}$/KJ600 catalyst shows uniform distribution of Pt nanoparticle on the surface, while relatively more concentrated on top surface (**Figure 5-7c-d**). Pt/C commercial catalyst was

also investigated as a benchmark, where the Pt nanoparticles are deposited on the surface of carbon support (**Figure 5-7e, 5-8**). To make a quantitative analysis on the Pt dispersion, particle size distribution was also performed on Pt_{inside}/KJ600, $Pt_{outside}$/KJ600 and Pt/C respectively (**Figure 5-7d-f**). Average particle size of Pt_{inside}/KJ600, $Pt_{outside}$/KJ600 and Pt/C are 2.01, 2.04 and 2.75 nm respectively. These results also correlated with particle size calculated from XRD peaks. Moreover, Pt_{inside}/KJ600 show most narrow particle size distribution, while Pt/C and $Pt_{outside}$/KJ600 showed similar broad particle size distribution compared to Pt_{inside}/KJ600. In fact, uniform size of nanoparticle was maintained due to confinement effect of carbon nanopore. EDAX mapping further supports the uniform distribution for both catalysts (**Figure 5-9**).

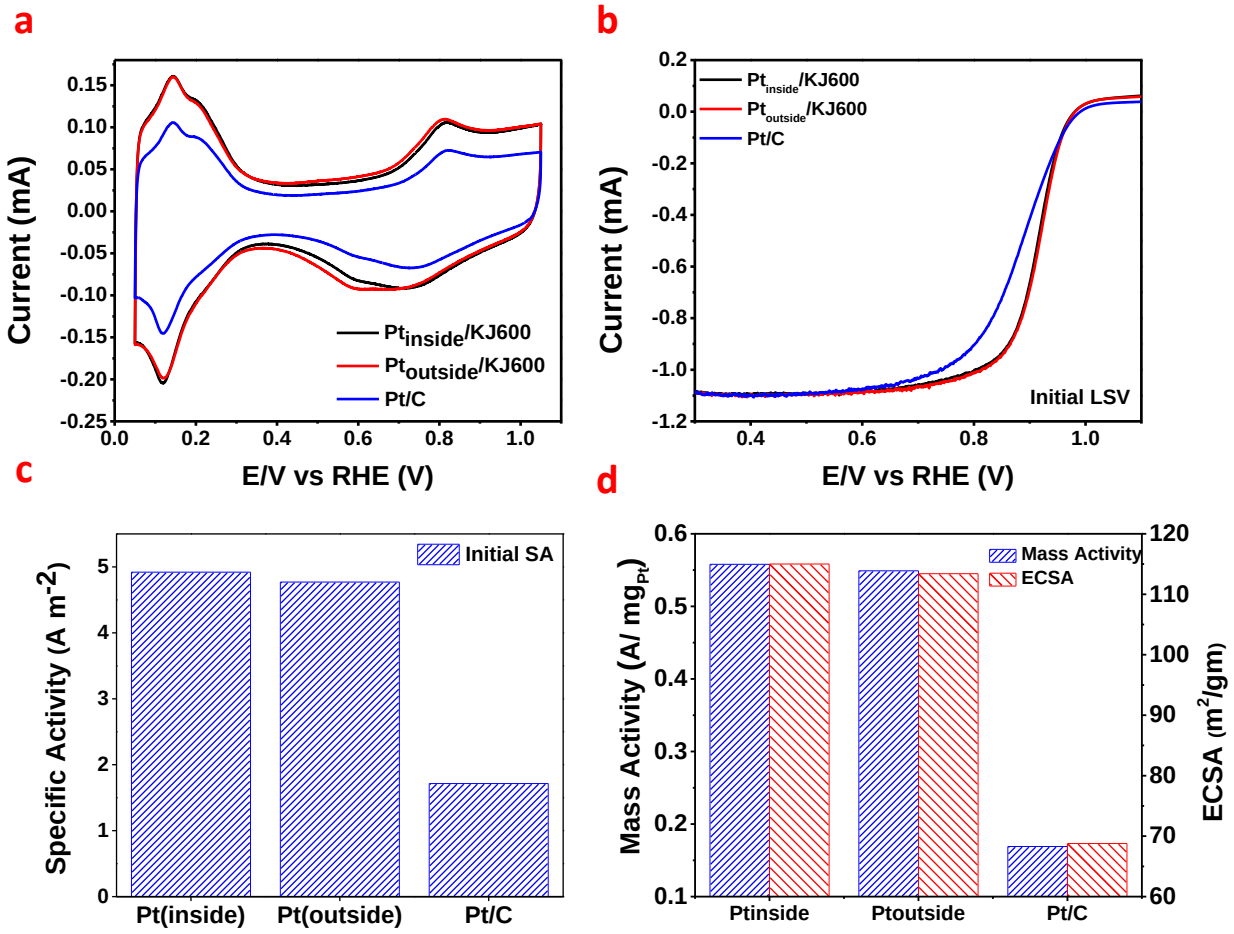

Figure 5-10: Initial electrocatalytic performance of Pt_{inside}/KJ600, $Pt_{outside}$/KJ600 and commercial Pt/C catalyst for ORR (a) CV comparison, (b) ORR polarization curve comparison, (b) Mass activity before and after 20K cycle, (c) ECSA comparison before and after 20K cycle, (d) Initial mass activity and ECSA, of Pt_{inside}/KJ600, $Pt_{outside}$/KJ600 and commercial Pt/C catalyst respectively.

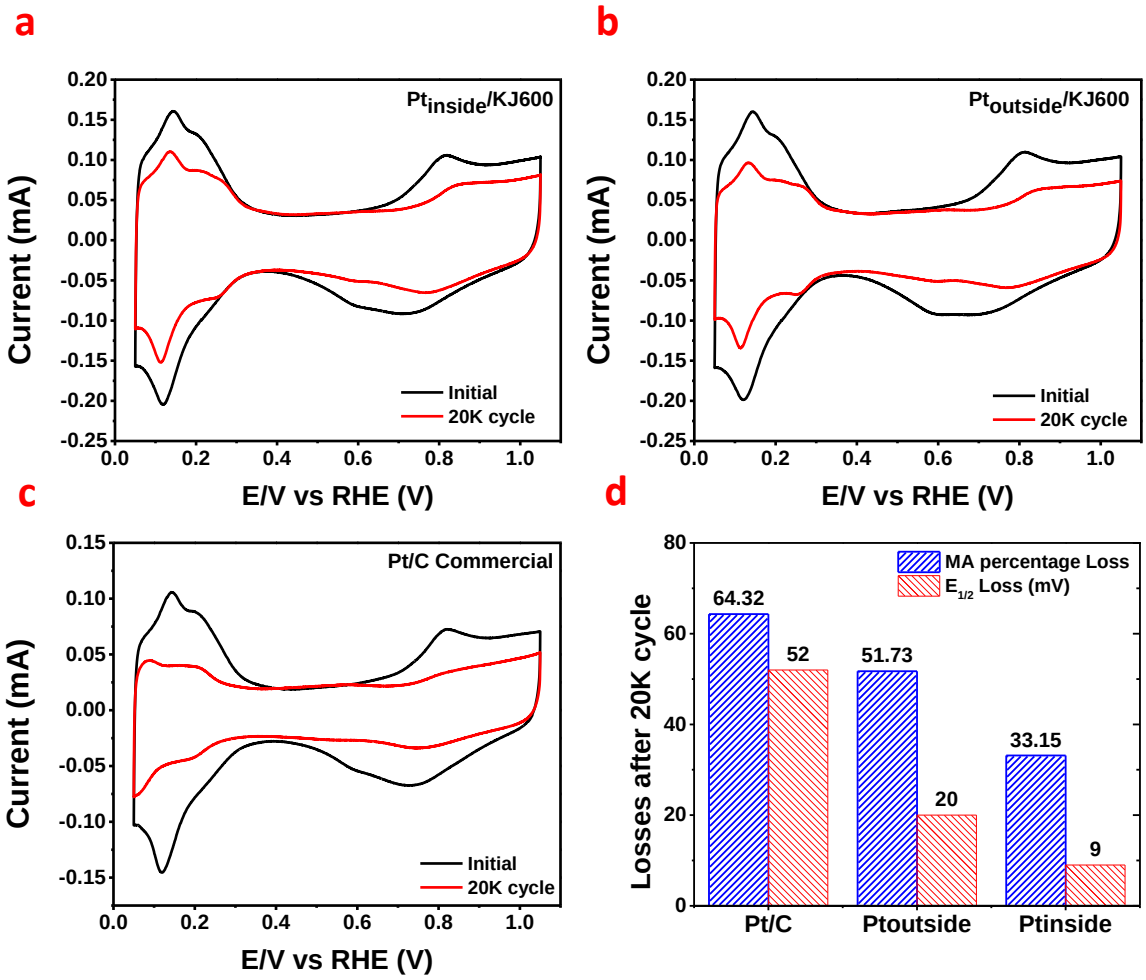

Figure 5-11: Initial and after 20K cycle CV curve comparison, (a) Pt_{inside}/KJ600, (b) $Pt_{outside}$/KJ600, (c) Pt/C, and (d) Mass activity percentage loss and Half-wave potential loss comparison.

Electrochemical activity and durability test of Pt_{inside}/KJ600 and $Pt_{outside}$/KJ600 catalyst was assessed in three cell system using rotating disk electrode (RDE) and compared with commercial Pt/C (TKK, 28.2 %) at same conditions. Inductively coupled plasma (ICP) test was performed to establish the Pt concentration in synthesized catalyst for the activity assessment. Potentiodynamic electrochemical measurement Cyclic voltammetry (CV) was used for catalyst activation and

electrochemical surface area (ECSA) measurement. Initial activation of $Pt_{outside}$/KJ600 took around 50 cycle which was same for commercial Pt/C catalyst. Considering both catalysts where Pt nanoparticle was deposited on the surface, while Pt_{inside}/KJ600 took few more cycles for catalyst activation. Activation of Pt_{inside}/KJ600 took a little higher number of cycles as wetting of Pt nanoparticles in the proximity of carbon pore took longer.[45] These phenomena can be further explained as activation cycles improve wettability of carbon channel porous network as a result even after durability cycles Pt nanoparticles are better accessed. Initial CV was recorded after catalyst activation at a scan rate of 20 mV s^{-1} in N_2 saturated 0.1 M $HCl0_4$ solution (**Figure 5-10a**). ECSA was calculated for positive going sweep between 0.05-0.4 V (all potentials used in this work are relative to the reversible hydrogen electrode (RHE)) for hydrogen underpotential desorption (HUPD) region. The charge density under HUPD was assumed to be 210 μC cm^{-2} and was used to normalize electrode surface area. The two peaks were observed at the 0.14 V and 0.21 V and considered as desorption of weakly (0.14 V) and strongly (0.21 V) adsorbed hydrogen. Initial ECSA for Pt_{inside}/KJ600, $Pt_{outside}$/KJ600 and Pt/C are 113.4, 115 and 68.78 m^2 gm^{-1}_{Pt} respectively. Even though nanoparticles are confined inside the nanopores shows a large ECSA advocates there was no hinderance or obstruction in electrolyte and reactant accessibility at the catalytically active sites.[47] Higher ECSA of synthesized catalyst are due smaller size of Pt nanoparticles, hence possess more catalytically active sites and validates advantages of facile one-step synthesis methods adapted in this work.

The ORR polarization curve of the catalyst was obtained at a scan rate of 10 mV s^{-1} in 0.1M $HClO_4$ solution at 1600 rpm and was corrected for ohmic drop. At the same conditions initial Half-

wave potential of Pt_{inside}/KJ600 and $Pt_{outside}$/KJ600 were observed at 0.9 V and were 32 mV higher than the commercial Pt/C catalyst (**Figure 5-10b**). Mass activity calculated for Pt_{inside}/KJ600 catalyst is 0.558 A mg^{-1}_{Pt} and 0.549 A mg^{-1}_{Pt} for $Pt_{outside}$/KJ600 at 0.9 V vs RHE respectively. Initial activity of synthesized catalyst crossed the U.S. Department of Energy 2025 target (0.44 A mg^{-1}_{Pt}) and about 3.3 times higher than commercial Pt/C catalyst (0.169 A mg^{-1}_{Pt}).[2] Specific activity of Pt_{inside}/KJ600 and $Pt_{outside}$/KJ600 are measured as 4.92 and 4.77 A m^{-2}_{Pt} respectively and earlier one is 2.0 times higher than Pt/C (2.457 A m^{-2}_{Pt}) (**Figure 5-10c**). Higher ORR activity of synthesized catalyst compared to Pt/C can be ascribed to higher ECSA, smaller particle size distribution, optimized electronic structure and higher Pt(0)/Pt(II) ratio as seen from XPS results. Initially Pt_{inside} and $Pt_{outside}$ catalysts showed similar ECSA, mass activity and specific activity due to similar particle size distribution, invariable electronic configuration as shown in XPS results, and support material structure. High surface area of support material is good enough to accommodate Pt nanoparticles within nanopores. While large porous structure which are interconnected and embedded with each other, establishes easily accessible pathway for ion movement without hindering mass transfer and reaction kinetics when compared to $Pt_{outside}$/KJ600 or Pt/C catalyst where Pt is deposited on the surface. High density of active sites diminishes the reaction kinetics limitations. Previous (Pt@HGS) studies showed mass transport resistances due to confinement of particles inside the pores but was not the case even at high current density for the catalyst synthesized in this work.[45] In fact, Pt deposited inside nanopore do not suffer any limitations. Furthermore, these nanopores kept nanoparticles intact and confined which can help in long-term stability of catalyst while prevents Pt dissolution and agglomeration.

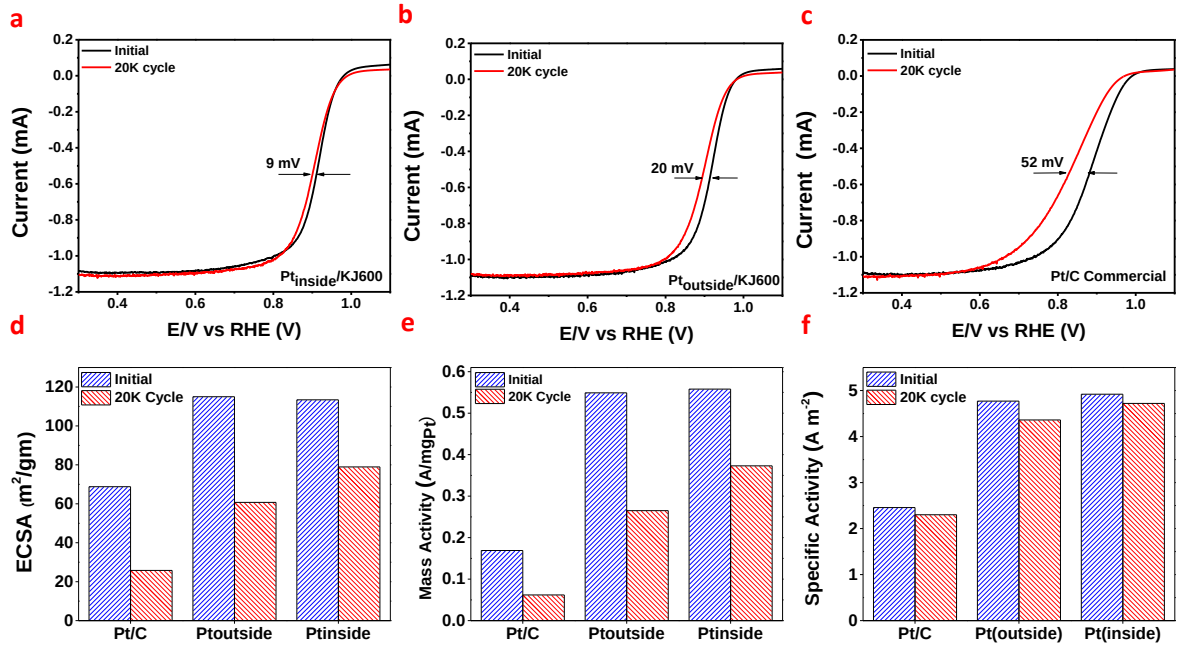

Figure 5-12: ORR polarization curve before and after 20K cycle for, (a) Pt_{inside}/KJ600, (b) $Pt_{outside}$/KJ600 (c) Pt/C catalysts, (d) ECSA, (e) Mass activity and (f) Specific activity comparison before and after 20K cycle for Pt_{inside}/KJ600, $Pt_{outside}$/KJ600 and Pt/C respectively.

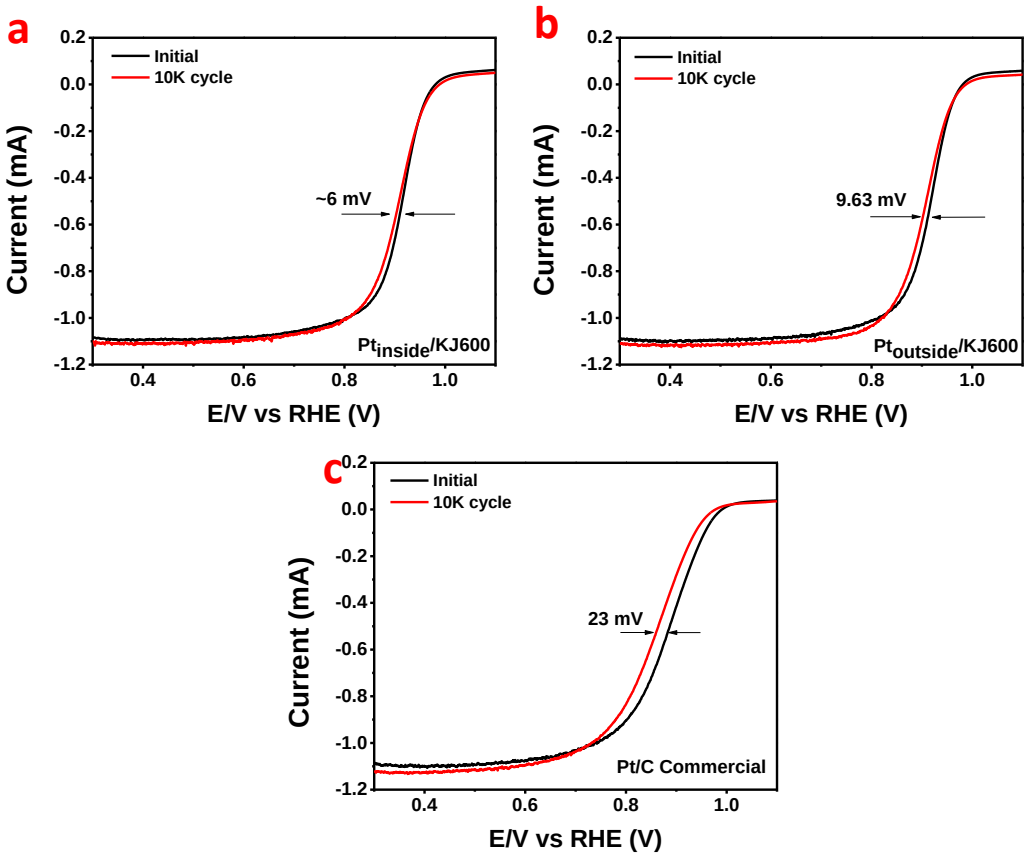

Figure 5-13: Initial and after 10K cycle ORR polarization curve comparison, (a) Pt_{inside}/KJ600, (b) $Pt_{outside}$/KJ600 and (c) Pt/C.

To establish the stability of catalyst due to seeding of Pt nanoparticle inside nanopores long-term durability test was performed. The stability of synthesized catalyst was examined by cycling between 0.6-1.1 V vs RHE at a scan rate of 50 mV s^{-1} up to 20000 cycles in N_2 saturated 0.1 M $HClO_4$ solution. CV curves before and after 20K cycles for Pt_{inside}/KJ600, $Pt_{outside}$/KJ600 and Pt/C were shown in **Figure 5-11**. ECSA of Pt_{inside}/KJ600 after 20K cycles was 78.96 m^2 gm^{-1}_{Pt} which is still higher than the initial ECSA of Pt/C (68.78 m^2 gm^{-1}_{Pt}) and 3.10 times higher after 20K cycles (25.80 m^2 gm^{-1}_{Pt} for Pt/C). Pt_{inside}/KJ600 and $Pt_{outside}$/KJ600 shows almost same initial ECSA while after 20K cycle $Pt_{outside}$/KJ600 loss was more significant as seeding inside pore proved

to be more efficient in term of activity and stability towards ORR (**Figure 5-12d**). ORR Polarization curve was also recorded after durability test and compared with initial polarization curve to estimate the half-wave potential loss for each catalyst. Half-wave potential loss was 9 mV, 20 mV and 52 mV for Pt_{inside}/KJ600, $Pt_{outside}$/KJ600 and Pt/C respectively and was significantly higher for both commercial Pt/C and $Pt_{outside}$/KJ600 (**Figure 5-12a-c**). While, Half-wave potential loss of Pt_{inside}/KJ600, $Pt_{outside}$/KJ600 and Pt/C was also recorded after 10K cycle and found to be 6 mV, 9.63 mV and 23 mV respectively (**Figure 5-13**). Therefore, further cycling form 10-20 K led to only 3 mV half-wave potential loss compared to Pt/C (~29 mV). Half-wave potential loss results endorse the benefit of seeding of Pt inside pore as it can hinders Pt dissolution and agglomeration and helps in maintaining the active sites and higher activity. Mass activity and specific activity is most important parameters for Pt based catalyst and was calculated to eventually compare and visualize catalyst activity after durability testing. Mass activity of Pt_{inside}/KJ600 was 0.373 A mg^{-1}_{Pt} after 20K cycle which is even 2.20 times higher than Pt/C initial activity. Mass activity of Pt_{inside}/KJ600 was 6 times higher than Pt/C (0.0619 A mg^{-1}_{Pt}) catalyst after 20K cycles and showed an outstanding improvement over the commercial catalyst (**Figure 5-12e**). Once Pt_{inside}/KJ600 compared with $Pt_{outside}$/KJ600 catalyst former has significant +11 mV half-wave potential improvement under same durability cycle. $Pt_{outside}$/KJ600 (0.265 A mg^{-1}_{Pt}) lost 52 percent of initial mass activity compared to 33 percent loss in Pt_{inside}/KJ600 after 20K cycle. There was only 4 percent loss in specific activity calculated for Pt_{inside}/KJ600 (4.72 A m^{-2}_{Pt}), therefore, specific activity of Pt_{inside}/KJ600 was approximately 7 times higher than Pt/C after 20K cycle

(**Figure 5-12f**). Evidence from ORR polarization curve strongly suggests highest stability in case of Pt confined inside pores.

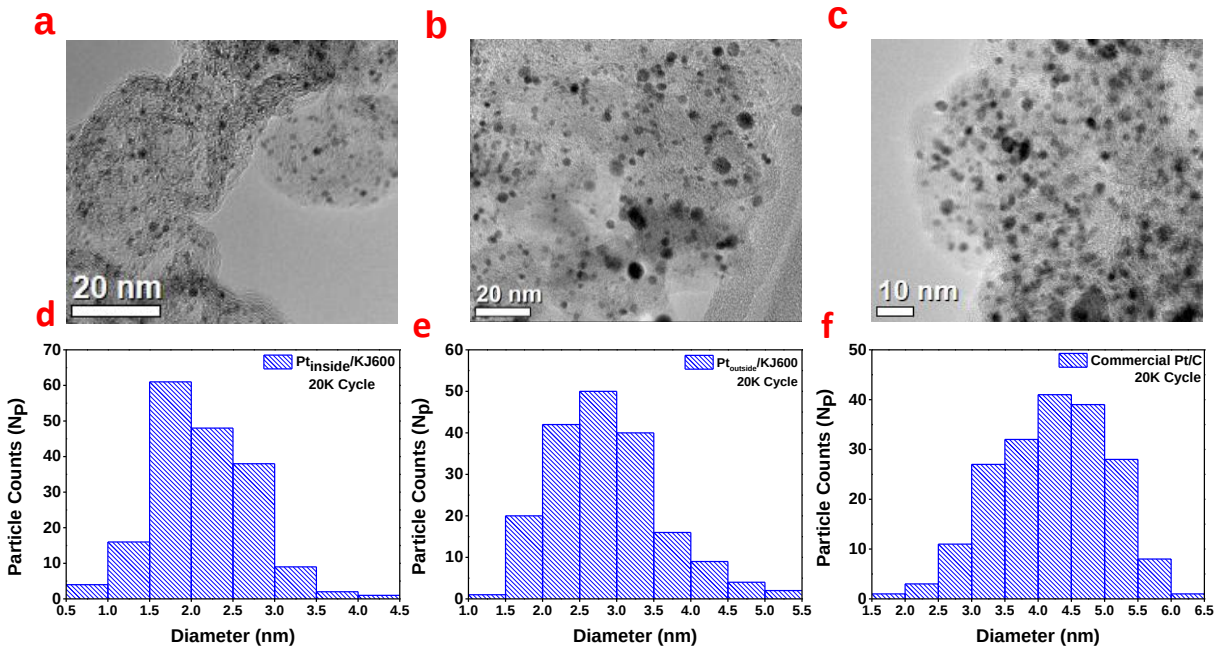

Figure 5-14: Physical characterization after durability test (a) HR-TEM image of Pt_{inside}/KJ600, (b) TEM images of $Pt_{outside}$/KJ600, (c) Overview TEM image of Pt/C after 20K cycle respectively, (d) Pt_{inside}/KJ600, (e) $Pt_{outside}$/KJ600 and (e) Pt/C, particle size distribution after 20 K cycle respectively.

To further verify the stability of Pt_{inside}/KJ600 after durability testing, TEM, and particle size distribution was performed on the tested catalyst. Tested catalyst was collected from glassing carbon electrode and preserved in DDI before further imaging was performed. Pt_{inside}/KJ600 shows no major change in KJ600 and Pt nanoparticles size (**Figure 5-14a**). There was general trend of Pt nanoparticle coalition or agglomeration due large durability cycle in $Pt_{outside}$/KJ600 and Pt/C (**Figure 5-14b-c**). Commercial Pt/C shows most particle agglomeration and deteriorate over time and was the reason behind loss in activity over time. Similar trend was seen in $Pt_{outside}$/KJ600 but

wasn't as bad as Pt/C catalyst and compliments the trend observed in electrochemical results throughout this work. Particle size distribution was performed on TEM image of Pt_{inside}/KJ600, $Pt_{outside}$/KJ600 and Pt/C catalyst after durability test (**Figure 5-14d-f**). Average particle size calculated from particle size distribution is 2.16, 2.92 and 4.23 nm for Pt_{inside}/KJ600, $Pt_{outside}$/KJ600 and Pt/C and can be compared with before durability cycle results (**Figure 5-7f-h**). Significant increase in Pt nanoparticle size is due agglomeration while loss in ECSA supports dissolution in case of $Pt_{outside}$/KJ600 and Pt/C.

5.4 Conclusion

Ultrafine Pt nanoparticles embedded inside the nanopore of carbon support were designed and successfully synthesized with facile one-step reduction method developed in this work. Combining XRD, BET and TEM observations, we confirmed the uniform dispersion of Pt nanoparticles inside the pore with a narrow particle size distribution for the Pt_{inside}/KJ600. As a result, Pt_{inside}/KJ600 exhibits unprecedented ORR activity with mass activity of 0.558 A mg^{-1}_{Pt} (@ 0.9 V vs RHE), outperforming the Pt/C benchmark (0.169 A mg^{-1}_{Pt}) and any sole Pt based catalyst synthesized so far, which is attributed to the increase in Pt utilization (ECSA of 113.4 m^2 gm^{-1}_{Pt}) and optimized electronic structure of Pt. Moreover, pore confinement of nanoparticle was beneficial in maintaining smaller particle size strongly intact within pore while undergoing durability test, which can effectively suppress Pt dissolution and aggregation therefore maintaining active for ORR activity. Impressively, the Pt_{inside}/KJ600 demonstrated only 31% loss of mass activity after 20k cycles, while the Pt/C undergoes 64% loss. The structural characterizations for the catalysts after stability test strongly revealed that our unique catalyst design effectively

maintained the uniform distribution of Pt nanoparticles as a result of space-confinement effect. This material synthesis concept is not limited to confine Pt nanoparticles inside pores and effectively immobilize Pt nanoparticles as an active material. We believe this catalyst design can be easily extended to synthesize Pt based alloy (with transition metal) to further improve activity and stability. Doping of heteroatoms N, S and B will also be applicable inside pore to improve durability by assimilating pore-confinement and tethering effect. In fact, we got exceedingly promising results with doping and will be follow-up of this current work.

Chapter 6: Spatial confined platinum nanoparticles within Sulfur doped carbon nanopore to improve oxygen reduction stability

6.1 Introduction

Polymer electrolyte membrane fuel cells (PEMFCs) is a green energy, zero emission technology which produce energy and water as only by-product from hydrogen and oxygen, and widely considered as future of transportations.[2,189] Development of highly active and durable catalyst to catalyze oxygen reduction reaction (ORR) remains a challenge in large-scale commercialization of PEMFC technology.[172,189] Metal based catalyst on carbon support has long been used to catalyze variety of reactions including oxygen reduction reactions (ORR), which is critical due to their limiting reaction kinetics in PEMFCs.[151] Platinum is best available metal catalyst to catalyze ORR in PEMFCs acidic, oxidative and corrosive environment.[190] However, catalytic activity and performance has been plagued owing to agglomeration, dissolution and sintering of precious Pt metals from the support surface.[24,149] This has led to sharp decrease in electrochemically active surface area (ECSA) and concurrently loss of catalytically active sites. Exposed surface atoms takes part in catalytic activity, and their activity increase with decrease in particle size.[54,191,192] Although, relatively higher surface energy of smaller nanoparticle makes it more vulnerable to sintering, particle agglomeration and dissolution from support materials. As a result, ORR activity and long-term stability of the catalyst degrades overtime in addition to the loss of precious Pt metal.[3] In sintering, nanoparticle follows Brownian movement on the surface

due to weak particle-support interaction, and consequently coalesce with other particles in close vicinity. While, in Ostwald ripening small nanoparticle with higher chemical potential coalescence to a larger particle with lower energy that led to the growth of nanoparticles.[28,31] Agglomeration and dissolution can be reduced by minimizing chemical potential within particles due large variation in particle size distributions, and non-uniform dispersion.[30] Two different approach can be examined to prevent sintering and agglomeration by modifying physical or chemical structure of the catalyst material.[59] Physical approach modifies the spatial arrangement of catalyst nanoparticle and support to provide a barrier towards sintering. Such as encapsulation of Pt nanoparticle within nanopores, which can provides three-dimensional confinement and minimize the particle migration as if on support surface and hence mitigate particle coalescence.[45,47,193] While encapsulation approach promises improvement in stability but they can suffer from limited access of active phase, ions and mass transfer limitations. Pt nanoparticle was deposited on the wall of ordered mesoporous carbon but have shown limited mass activity.[194] Chemical approach involves modifying catalyst chemistry at atomic scale, which involves altering chemical or electronic structure of catalyst or support material to stabilize nanoparticle.[59] Several chemical strategy have been looked to circumvent the sintering include design of metal-metal oxide core shell structures, addition of metal oxide stabilizers and also use of sintering-resistant support material.[195] While these strategies still lack benchmark activity threshold. Another strategy is to improve the metal support interactions which can restrict the particle migration, agglomeration and detachment on the support material.[95,100,179] Heteroatom doping changes the electronic properties and create a positive charge on the carbon atom in the vicinity of heteroatoms. These

sites generally considered as catalytically active sites where oxygen reduction takes place.[196,197] Doping favors electro-neutrality of carbon by improving molecular adsorption of oxygen and therefore benefit oxygen reduction. Heteroatoms doping also exerts a tethering effect on the platinum nanoparticles which helps in improvement both activity and stability of nanoparticles.[127,198] Heteroatoms such as nitrogen and sulfur are used to dope carbon support to improve the interaction and synergy between catalyst and support material.[127,128] Sulfur doping enhance the catalytic activity by improving the electron conductivity of support material and favors metal support interaction.[135,199,200] Thiophenic sulfur are considered active and improve oxygen reduction activity.[95,100] In fact, most of the work has been done on doping of sulfur on the surface of support materials.[61,108,135,201] Individually catalyst with heteroatom doping or deposition of platinum within carbon nanopores have shown potential to improve ORR kinetics and long-term stability. However, there is no work done to deposit platinum inside sulfur-doped nanopore to confine nanoparticles to reduce sintering and dissolution. Heteroatom doping within nanopore complements with Pt nanoparticle within nanopores can significantly improve stability of ultrafine platinum particles. These two strategies can work synergistically to reduce sintering and improve platinum-based catalyst long-term stability for oxygen reduction in acidic medium.

In this work, we have developed a strategy to synthesize sulfur-doped inside pore of carbon support (S_{in}/KJ600), then controlled nucleation Pt nanoparticles inside pore of support material (Pt@S_{in}/KJ600). Pore-confinement effect was adapted to synthesize ultrafine Pt nanoparticles of uniform size distribution, while sulfur doping will further enhance interaction between support and catalyst nanoparticles. To our best knowledge this is first time both doping and positioning of

metal catalyst inside pores is introduced together. We have successfully synthesized sulfur-doped inside carbon pores supported ultrafine Pt nanoparticles with average nanoparticle size less than 2 nm (Pt@S_{in}/KJ600). To establish effect of sulfur doping inside pore and confinement of Pt inside pore, another catalyst where sole Pt nanoparticle deposited inside pore (Pt@KJ600) was also synthesized. Designed catalyst combined multiple concepts to delivers high performance ORR catalyst; (i) Spatial confinement effect control the nucleation of Pt nanoparticles within carbon nanopores will restricts nanoparticles overgrowth to guarantee high surface area to volume ratio. This led to higher number of actives sites and limits nanoparticles aggregation in long-term stability test; (ii) Sulfur doping within carbon nanopore imparts tethering effect that change electronic structure to improve catalytic activity, while improved interactions between catalyst nanoparticles and carbon support will further reduces nanoparticles dissolution and agglomerations which led to better long-term stability; (iii) The choice carbon support with high surface area and porous network framework was to accommodate Pt nanoparticles with ease. The synergetic effect of catalyst developed in this work have shown excellent activity and remarkable long-term stability for oxygen reduction in acidic medium.

6.2 EXPERIMENTAL SECTION

6.2.1 Sulfur doped inside KJ600

Sulfur was doped inside pores of KJ600 (Ketjen black EC-600JD, AkzoNobel) with flash heat treatment and quenching method. In a typical synthesis procedure, first sulfur precursor (Phenyl disulfide, Sigma Aldrich) solution in anhydrous ethanol (Sigma Aldrich) was added to 50

mg of KJ600 and sonicated for 2 hours. Sonication was performed to saturate carbon pores with sulfur precursors. After sonication saturated carbon material was left overnight in vacuum oven at 60 °C to remove the ethanol. After drying in vacuum oven KJ600 pore were saturated with PDS. Sulfur doped inside KJ600 (S_{in}/KJ600) was synthesized by Flash heat treatment at 1000 °C for 30 minutes in Ar saturated environment and sample was taken out of heating zone after 30 minutes.

6.2.2 Pt deposited inside pore KJ600 (Pt@KJ600)

Platinum precursor ($H_2PtCl_6.6H_20$, Sigma Aldrich) solution was prepared in anhydrous ethanol and was added to the carbon support (KJ600). In a typical experiment, 100 mM of KJ600 was added to the 50 mg of KJ600 and was sonicated for 2 hours. Volume of solvent was fixed based on pore-volume and was estimated experimentally to saturate carbon power as if after saturation no liquid can be visible on the carbon powder. After sonication once platinum precursor was seeded inside the pore, saturated material vacuum dried overnight to evaporate ethanol from the material. In next step, dried material was heat treated at 400 °C for 2 hours in 10 percent H_2/Ar environment and as a result nucleation of Pt nanoparticle takes place inside pore.

6.2.3 Pt deposited inside pore of S_{in}/KJ600 (Pt@S_{in}/KJ600)

100 mM $H_2PtCl_6.6H_20$ solution in ethanol was prepared and added to the 50 mg of previously synthesized sulfur doped inside pore of KJ600 (S_{in}/KJ600). Pt precursor solution in KJ600 were sonicated for 2 hours water bath. Once sonication established the saturation of carbon support, sample were followed with vacuum drying for ethanol evaporation. Finally, dried sample were heat treated at 400 °C for 2 hours in 10 percent H_2/Ar and cooled in pure argon environment.

Final synthesized materials were collected from furnace in each case and were further taken for Physiochemical and electrochemical characterization.

6.2.4 Physiochemical characterization:

To obtain characteristic peaks and diffraction pattern of catalyst material Powdered X-ray diffraction patterns were captured using Rigaku MiniFlex X-ray diffractometer at a scan rate of 1 degree per minute. All the synthesized materials were scanned at the same scan rate. Elemental composition was calculated based on inductively coupled plasma atomic emission spectroscopy (710-ES, Varian, ICP-OES) analysis. Electronic configuration and elemental state were identified by using X-ray photoelectron spectroscopy (XPS) from Thermo Scientific K-Alpha spectrometer. Surface area and pore volume analysis was performed on Micrometrics ASAP 2020 unit based on Brunauer-Emmett-Teller theory. Physical morphology, particle size distribution was investigated by using Hitachi HD2700C STEM equipped with a probe aberration corrector operated at 200 kV and JOEL 2100F at 200 kV.

6.2.5 Electrochemical characterization:

Electrochemical activity and performance test were performed on three electrode testing cells. Cyclic voltammetry and Linear sweep voltammetry test were performed in 0.1 M $HClO_4$ solution using Biological VSP electrochemical station at room temperature. Glassy carbon electrode with active surface area of 0.196 cm^2 was used as working electrode, platinum wire was used counter electrode and reversible hydrogen electrode (RHE) was used reference electrode in three electrode testing cells. Deionized water and isopropanol were used in a ratio of (v/v = 1:1) with 20 µl of 5 weight percent Nafion solution was sonicated for 30 minutes to obtain well

dispersed catalyst ink and deposited in glassy carbon electrode. All potential mentioned in the manuscript is based on RHE. Pt loading was on the results obtained from ICP results. All the catalysts used in this work has undergone catalyst activation using cyclic voltammetry between 0.05-1.05 V vs RHE at a scan rate of 50 mV s^{-1} in $HClO_4$ solution saturated with N_2 gas. While ECSA was estimated by integrating hydrogen adsorption/desorption region between 0.05-0.4 V vs RHE and a charge density of 210 µC cm^{-2} was taken for hydrogen adsorption on monolayer of polycrystalline platinum surface. Linear sweep voltammetry (LSV) was performed between 0.05-1.1 V vs RHE at scan rate of 10 mV s^{-1} at rotating speed of 1600 rpm in 0.1 M $HClO_4$ saturated in O_2 environment. Polarization curve obtained from LSV was used to calculate kinetic current and mass activity at 0.9V vs RHE. Long-term stability test was performed for 20000 cycles between 0.6-1.1 V vs RHE at a scan rate of 50 mV s^{-1}. As benchmark state-of-the-art commercial Pt/C (TKK, 28.8%) was used compared with the results of synthesized catalyst.

6.3 Result and discussion:

A facile method was developed for synthesis of catalyst in this work. First sulfur was doped inside pore of carbon support (KJ600), and then followed with platinum deposition inside the sulfur doped pore. Different catalysts were synthesized, and detailed procedure is presented in the experimental sections. Overall synthesis strategy and pictorial diagram are represented in the Schematic diagram (**Figure 6-1**, **6-2**). Phenyl disulfide dissolved ethanol was added to KJ600 and were sonicated to channelize and saturate carbon pores with sulfur precursor followed with overnight vacuum drying to vaporize the ethanol from carbon material. Following this, flash heat

treatment was performed to obtain sulfur doped inside KJ600 pore (S_{in}/KJ600). Same procedure was repeated for synthesis of Pt@S_{in}/KJ600 and Pt@KJ600 catalyst (Pt is deposited inside KJ600). In brief, Pt precursor dissolved in ethanol was added to S_{in}/KJ600 and KJ600, sonicated and vacuum dried respectively, followed with heat treatment in 10 percent hydrogen that led to nucleation of Pt nanoparticle inside pores.

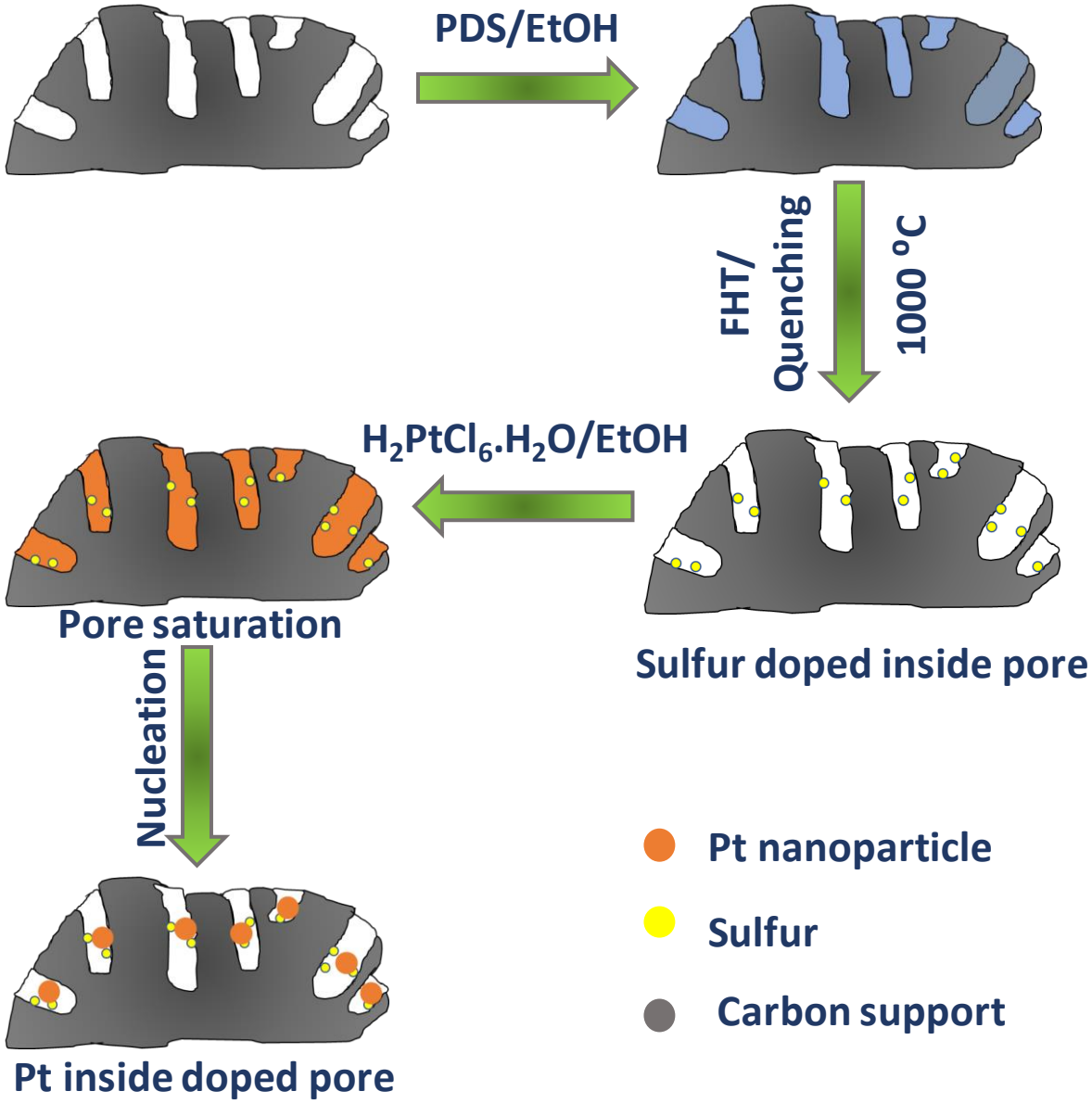

Figure 6-1: Schematic illustration of the synthesis route of Pt@S_{in}/KJ600.

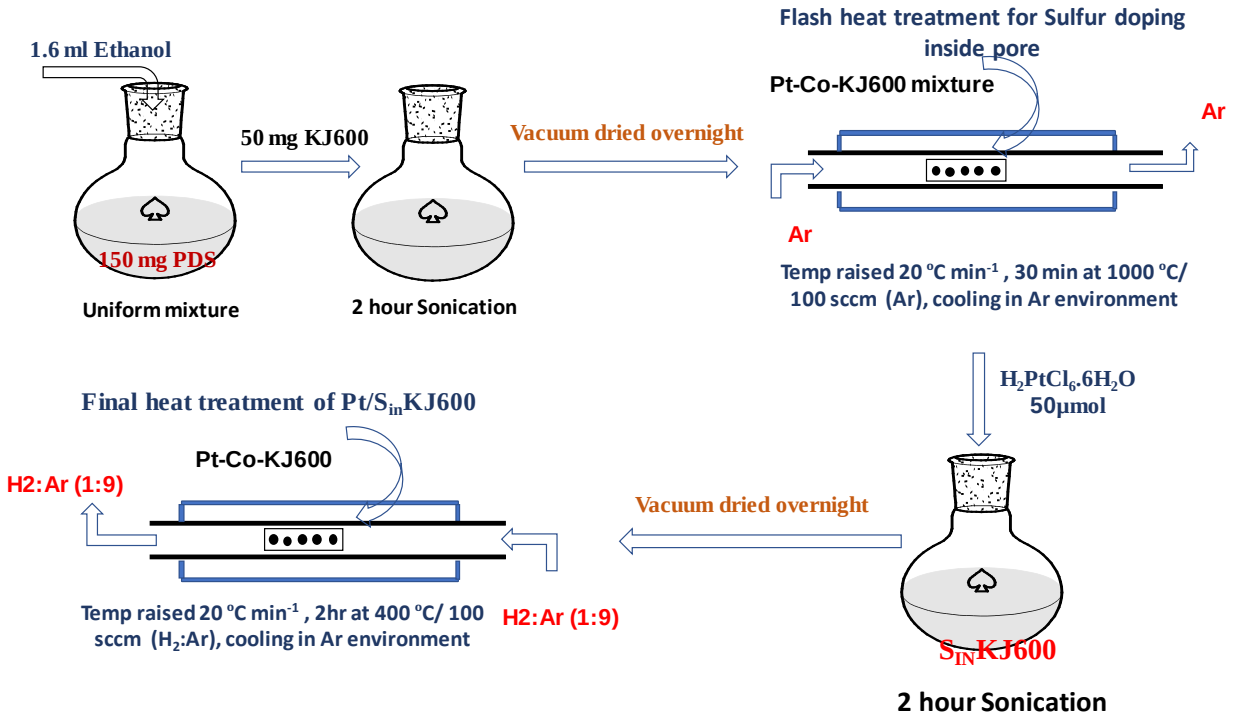

Figure 6-2: Experimental design of Pt@S_{in}/KJ600.

Crystalline nature of the synthesized catalysts was investigated and compared to commercial Pt/C catalyst using Powdered X-ray diffraction pattern (XRD) (**Figure 6-3a**). The characteristics peaks of Pt in Pt@S_{in}/KJ600 and Pt@KJ600 were obtained at 39.72°, 46.38°, 67.53° and 81.57° are corresponds to the Pt(111), Pt(200), Pt(220) and Pt(311) respectively. Diffraction pattern of Pt crystal plane displayed the typical face centered cubic (fcc) structure and were compared with commercial state of the art Pt/C (TKK, 28 %). There was no significant change in peak position obtained in for Pt@S_{in}/KJ600, Pt@KJ600 and Pt/C respectively. Average platinum particle size was obtained in the range of 2 nm using Scherrer equation. Pt@S_{in}/KJ600 and Pt@KJ600 average particle size along Pt(111) direction are 1.63 and 1.69 respectively. As expected, there was no huge difference in nanoparticle size as Pt was seeded inside pore of carbon in both cases. However, such

an ultrafine nanoparticle with average size smaller than 2 nm were obtained due to confinement of Pt nanoparticle inside nanopore of carbon support. Relatively smaller nanoparticles possess higher number of catalytically active sites and electrochemically active surface area (ECSA) as compared to Pt/C with average particle size between 2-5 nm. Moreover, typical carbon (002) plane peak is obtained at 24.3° for carbon support KJ600. Higher intensity of C(002) peaks for S_{in}/KJ600 compared to KJ600 were obtained and can be correlated to the numerous defects formation due to sulfur doping inside skeleton of carbon support (**Figure 6-4**). Higher intensity of C(002) peaks also leads to comparatively higher graphitization of carbon due to flash heat treatment at 1000 °C during sulfur doping. In general, graphitization kinetically delays the carbon oxidation, therefore reduces the detachment of catalytically active nanoparticles due to carbon corrosion and improve long-term durability of synthesized catalyst.[182,183] Graphitic nature and porous carbon network favours the mass and ions transfer of electrolyte and product of catalytic reactions.

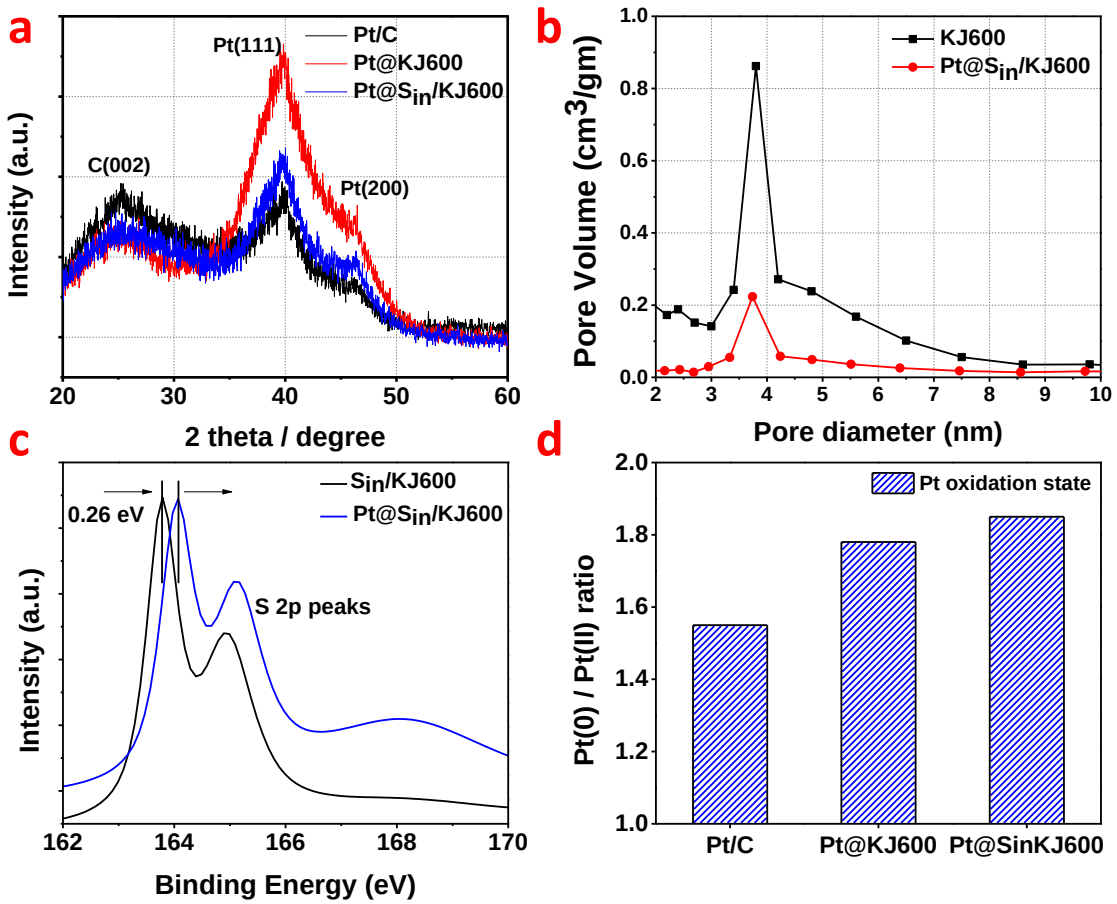

Figure 6-3: (a) Powdered X-ray diffraction pattern of Pt@S_{in}/KJ600, Pt@/KJ600 and Pt/C (b) BJH pore-size distribution of KJ600 and Pt@S_{in}/KJ600, (c) S2p high-resolution XPS spectra of S_{in}/KJ600 and Pt@S_{in}/KJ600, (d) Pt(0)/Pt(II) oxidation state ratio in deconvoluted Pt4f XPS spectra of Pt/C, Pt/KJ600 and Pt@S_{in}/KJ600.

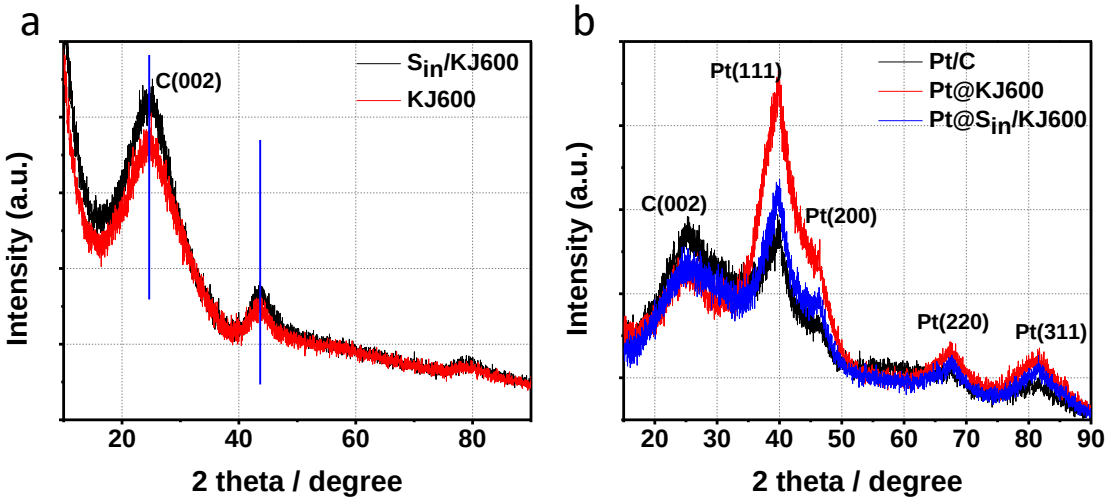

Figure 6-4: Full range XRD spectra of S_{in}/KJ600 and KJ600

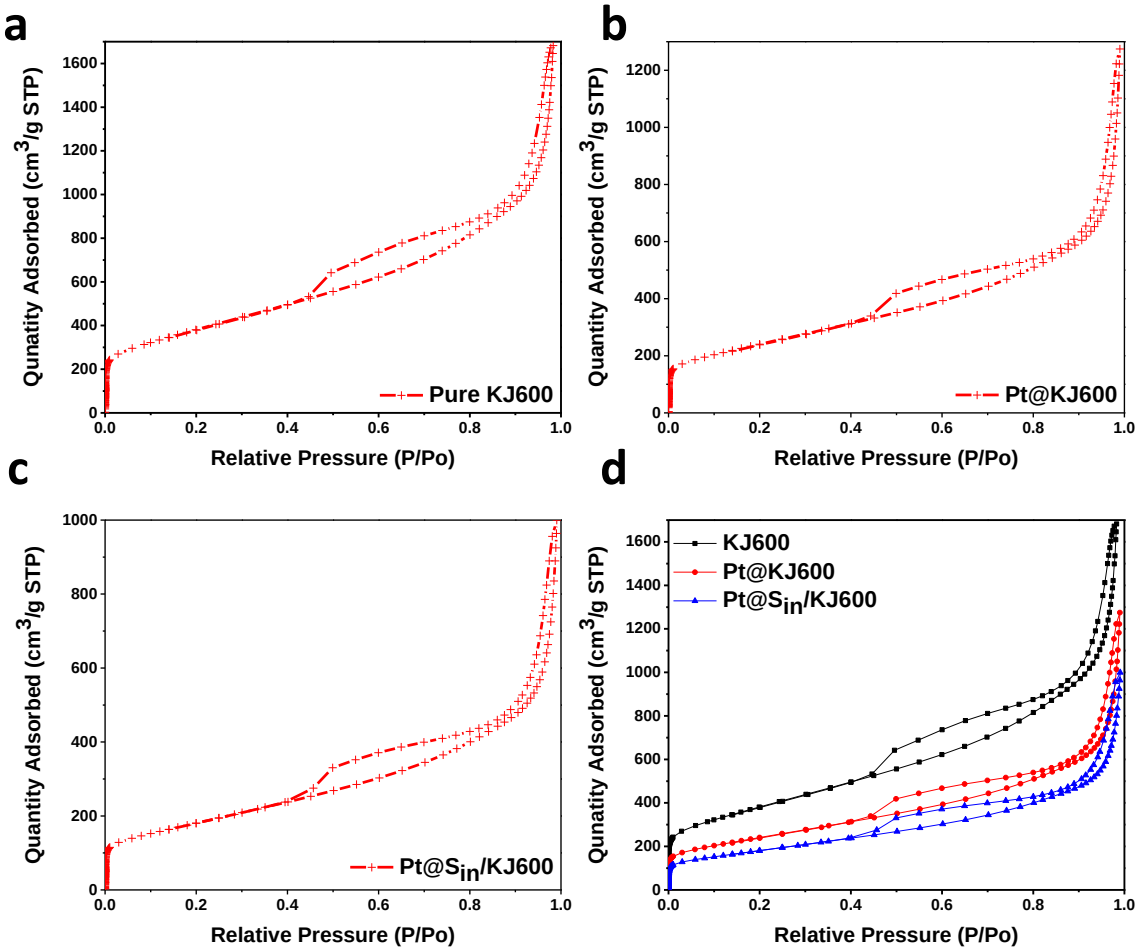

Figure 6-5: N_2 adsorption desorption isotherm (a) KJ600, (b) Pt@KJ600, (c) Pt@S_{in}/KJ600 and (d) comparison of KJ600, Pt@KJ600 and Pt@S_{in}/KJ600 catalyst respectively.

Higher surface area and porosity of the carbon support are an important factor for catalysis. Higher surface area and pores volume are an important factor which affects nanoparticles dispersion, mass transfer and ions movement during oxygen reduction. Therefore, pore volume, surface area was thoroughly investigated by N_2 adsorption methods. Surface area and pore volume of carbon support and synthesized catalyst was obtained through BET analysis, while pore volume analysis was performed using Barrett, Joyner and Halenda (BJH) desorption data. **Figure 6-5**

displayed the typical type-IV isotherms of KJ600, Pt@KJ600 which showed a characteristic H3 hysteresis loops discloses both micro and mesoporous nature of carbon support. The specific surface area of KJ600 estimated as 1363 $m^2 g^{-1}$ and pore volume of 2.59 $cm^3 g^{-1}$. Most of the pores KJ600 fall in the average 4 nm region with narrow pore size distribution (**Figure 6-3b**). Pore diameter are large enough for the channelization platinum and sulfur precursor solution, while large surface area and pore volume favors uniform dispersion and guarantee large number of nucleation sites. This will also result in easy diffusion of solvent and reactant to the active sites. **Figure 6-3b** shows pore size distribution of KJ600 and Pt@S_{in}/KJ600, and correspondingly there was no shift in peak position observed. However, the sharp decrease in peak area with narrower pore size distribution indicates the filling carbon nanopores with Pt and S atoms. Pore size of KJ600 is adequate enough to confine and effectively immobilize Pt@S nanoparticle.

To further interrogate nanopore filling, pore volume and BET surface area of KJ600 and synthesized catalysts was compared quantitatively. When only Pt was deposited inside pore of KJ600 (Pt@KJ600), BET surface area was decreased to the 860 $m^2 g^{-1}$. However, when both sulfur doping and Pt nanoparticle was deposited inside pore of KJ600 (Pt@S_{in}/KJ600), BET surface was decreased to 649.32 $m^2 g^{-1}$. In addition, pore volume was decreased to 1.62 $cm^3 g^{-1}$ for Pt@KJ600, while it was further drop down to 1.49 $cm^3 g^{-1}$ for Pt@S_{in}/KJ600. These results have clearly shown that surface area and pore volume was further reduced when both sulfur and Pt were deposited inside pore, while trivial decrease in pore volume from Pt@KJ600 to Pt@S_{in}/KJ600 is due to comparatively much smaller size of sulfur atom. Pt@S_{in}/KJ600, Pt@KJ600 and KJ600 N_2 adsorption desorption isotherm maintained similar shape of isotherms curve, except decrease in

surface area and pore volume (**Figure 6-5**). All these results imply the confinement of sulfur doped Pt nanoparticles inside pore of KJ600.

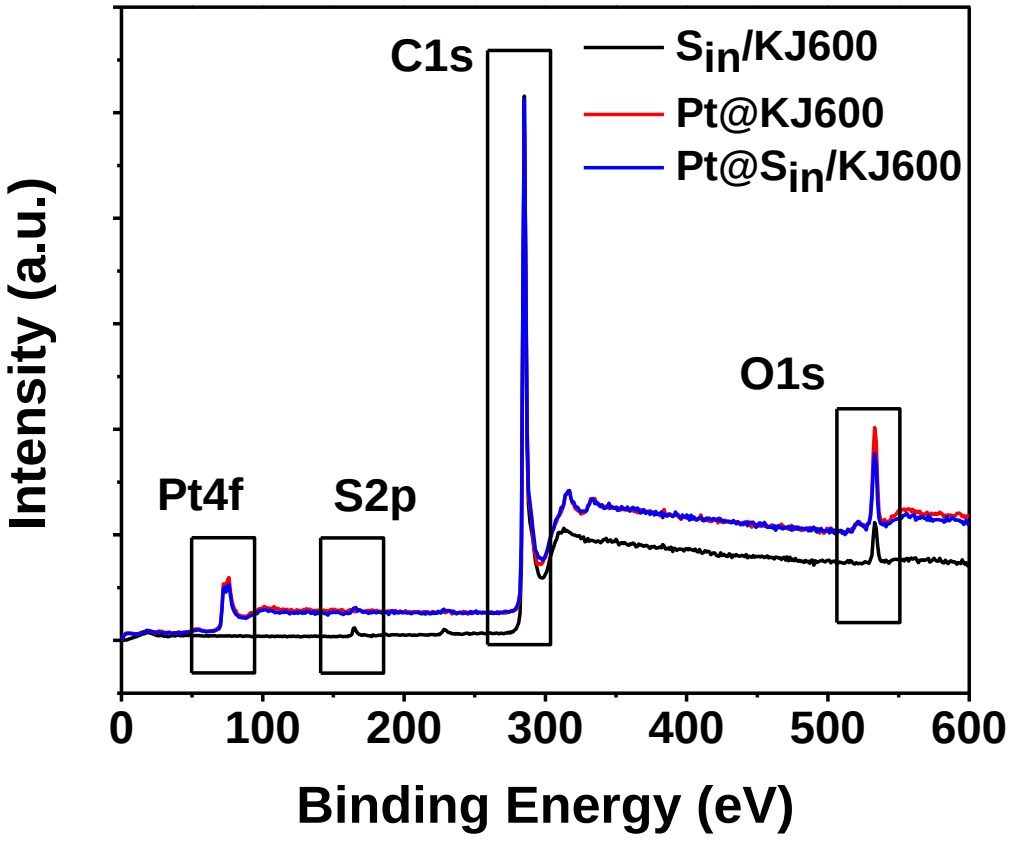

Figure 6-6: Full range XPS spectra of S_{in}/KJ600, Pt@KJ600 and Pt@S_{in}/KJ600 respectively.

Elemental composition and electronic configuration of the synthesized materials were studied using X-ray photoelectron spectroscopy (XPS). Full range XPS spectra of S_{in}/KJ600, Pt@KJ600 and Pt@S_{in}/KJ600 are presented in **Figure 6-7**. High resolution S2p spectrum was captured to understand the sulfur electronic structure when sulfur was doped inside pore of support

material KJ600 (S_{in}KJ600) and Pt@S_{in}KJ600 catalyst (**Figure 6-7**). For S_{in}/KJ600, high resolution S2p peaks are deconvoluted into two major peaks at 163.79 and 164.96 eV and attributed to the C-S-C bonds, while one minor peak appears at the 168.15 eV and related to -SO_x functional group. The minor -SO_x group peaks observed around 168 eV can be formed due to oxidation of sulfur in oxygen environment. In addition, two major S2p peaks in S_{in}KJ600 were separated by 1.17 eV, which are developed from the S2p spin-orbit doublet at $S2p_{1/2}$ and $S2p_{3/2}$ respectively.[143]

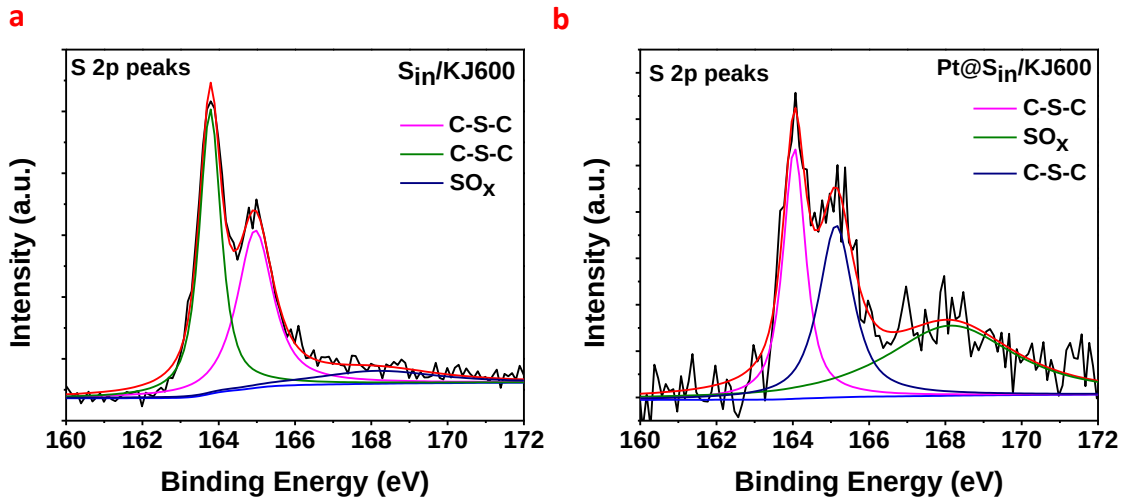

Figure 6-7: High-resolution full range S2p XPS spectra of (a) S_{in}/KJ600 and (b) Pt@S_{in}/KJ600.

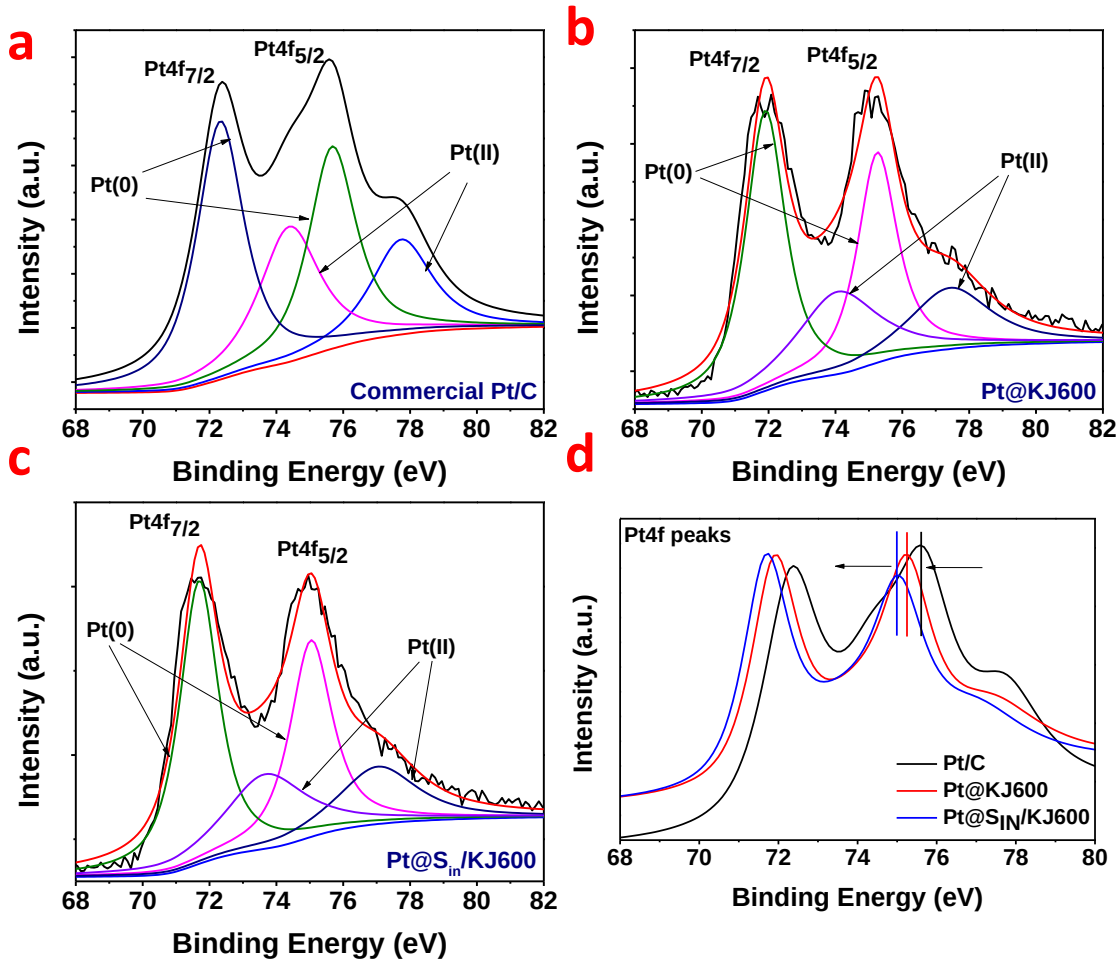

Figure 6-8: High-resolution full range Pt4f XPS spectra of (a) Commercial Pt/C, (b) Pt@/KJ600, (c) Pt@S_{in}/KJ600 and (d) peak shift comparison of Pt@S_{in}/KJ600, Pt@/KJ600 and Pt/C respectively.

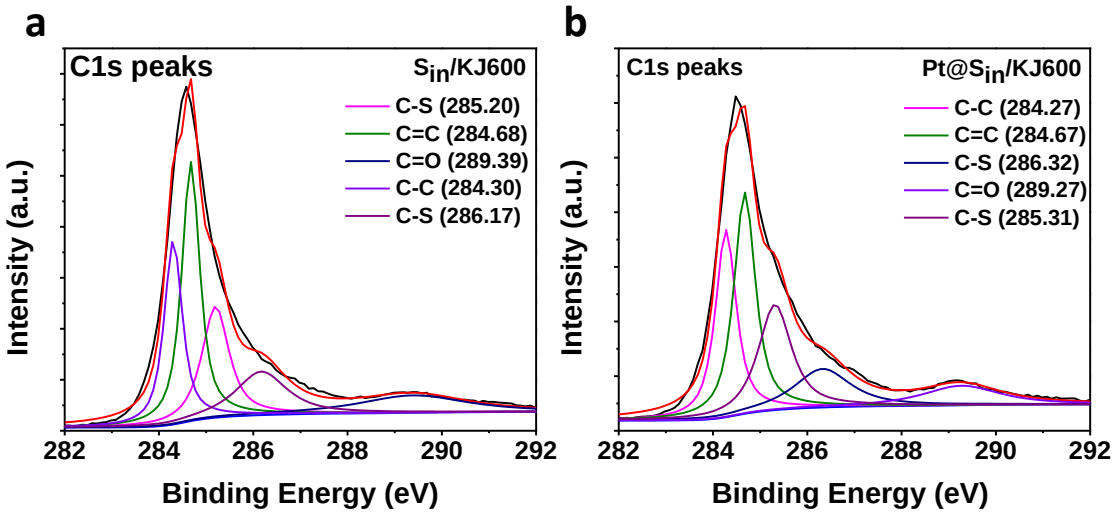

Figure 6-9: High-resolution full range C1s XPS spectra of (a) S_{in}/KJ600 and (b) Pt@S_{in}/KJ600.

These pairs of characteristic peaks in S_{in}/KJ600 are attributed to the thiophene and validate the use of flash heat treatment to incorporate sulfur directly into the carbon matrices and there was no elemental sulfur observed in XRD peaks.[147,148] Pt@S_{in}/KJ600 catalyst S2p peaks are also deconvoluted in two major peaks at 164.05 and 165.15eV and corresponds to the C-S-C bond, while a minor peak obtained at 168.14 eV are due to SO_x group (**Figure 6-7b**). There is a positive S2p peak shift of 0.26 eV in Pt@S_{in}/KJ600 compared to S_{in}/KJ600 (**Figure 6-3c**). The positive shift in S2p peaks clearly indicate the change in electronic structure due to Pt interaction with sulfur in -C-S-C- groups. To further analyze the change in Pt electronic structure and oxidation state high resolution Pt4f spectra of Pt@KJ600 and Pt@S_{in}/KJ600 was captured and compared with commercial Pt/C catalyst (**Figure 6-8**). High resolution Pt4f was deconvoluted into atomic Pt(0) and oxidized Pt(II) peaks. The $Pt4f_{7/2}$(0) and $Pt4f_{5/2}$(0) peaks were observed at 75.25 and 71.90 eV for Pt@KJ600 catalyst and were separated by 3.35 eV, while at 72.32 and 75.67 eV for Pt/C catalyst. There was a negative shift of Pt4f peak position by 0.42 eV for Pt@KJ600 compared

to Pt/C catalyst and can be due to attributed strong-metal support interaction due to confinement of Pt nanoparticles inside carbon pores.[185] While, for Pt@S_{in}/KJ600 catalyst, $Pt4f_{7/2}$(0) and $Pt4f_{5/2}$(0) peaks are observed at 71.67 and 75.02 eV. Therefore, a further negative shift of 0.23 eV observed from Pt@KJ600 to Pt@S_{in}/KJ600, which is due to Pt interaction with doped sulfur inside carbon nanopores (**Figure 6-8d**). The negative shift indicates improved interaction between Pt and support material, and further complements with positive shift of 0.26 eV observed in S2p peaks positions for Pt@S_{in}/KJ600 compared to S_{in}/KJ600. Metallic Pt(0) takes part in catalyzing oxygen reduction, therefore, ratio of metallic Pt(0) to the oxidized Pt(II) at initial condition will indicate about number of active site present in the catalyst. The Pt(0)/Pt(II) ratio for Pt@S_{in}/KJ600, Pt@/KJ600 and Pt/C are calculated as 1.55, 1.75 and 1.85 respectively (**Figure 6-3d**). Higher ratio can be an indication of higher oxygen reduction activity of the synthesized catalyst.[187,188] It can be concluded till this point as deposition Pt inside pore improve metal support interaction due spatial confinement effect (Pt@KJ600) and was further improved due to Pt interaction with sulfur doped inside pore (Pt@S_{in}/KJ600). The high resolution C1s spectra of S_{in}/KJ600 and Pt@S_{in}/KJ600 was also captured and shown C-C (284.30 eV), C=C (284.68 eV), C=O (289.39 eV) and C-S (285.2, 286.17 eV) peaks for S_{in}/KJ600. While, C-C (284.27 eV), C=C (284.67 eV), C=O (289.27 eV) and C-S (285.31, 286.67 eV) peaks are observed for Pt@S_{in}/KJ600 (**Figure 6-9**). Existence of C-S peaks indicate successful incorporation of sulfur inside carbon pore, while there was slight change in C1s (C-S) peak position indicate change in carbon electronic structure due to metal (Pt) sulfur interactions. These results successfully resonate with previous finding throughout this work.

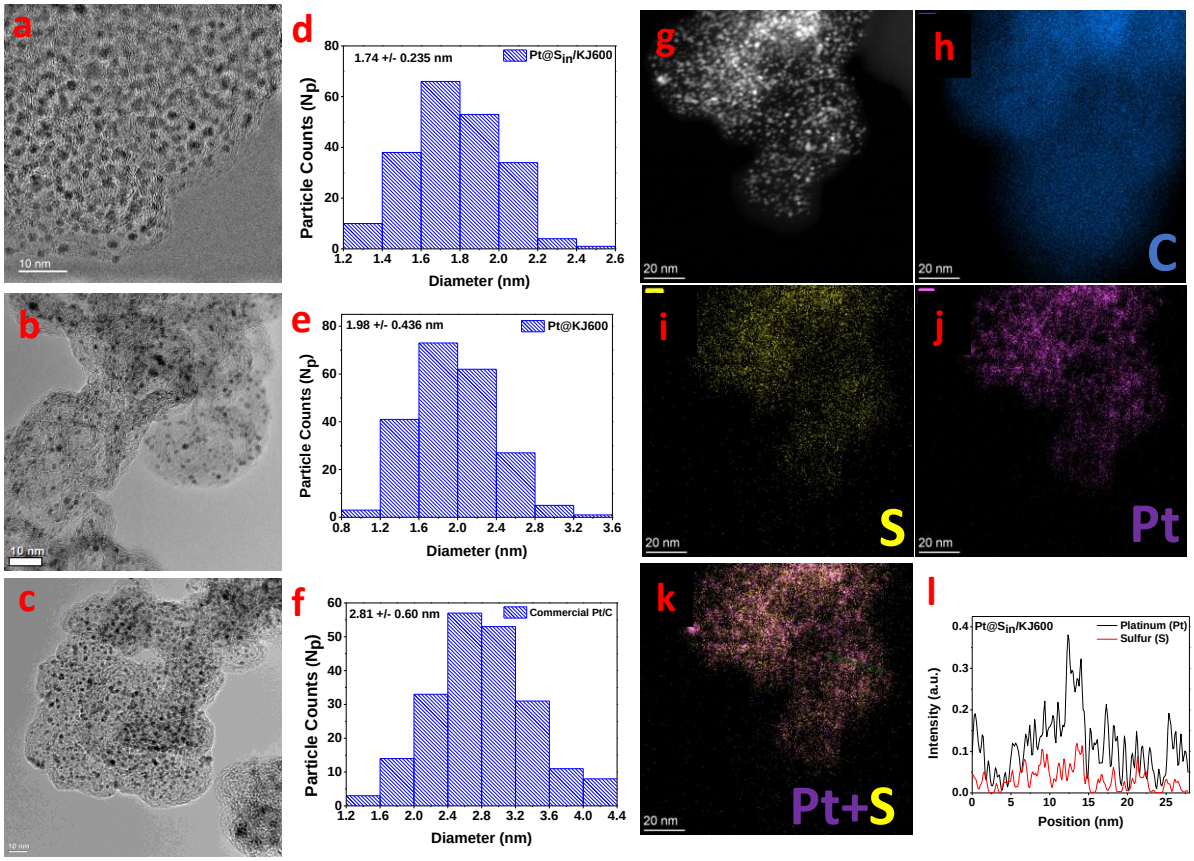

Figure 6-10: HR-TEM image of (a) Pt@S_{in}/KJ600, (b) Pt@KJ600, (c) Commercial Pt/C; Particle size distribution of (d) Pt@S_{in}/KJ600, (e) Pt@/KJ600, (f) Commercial Pt/C; HRTEM image of (g) Pt@S_{in}/KJ600, corresponding elemental mapping (h) Carbon, (i) Sulfur, (j) Platinum, (k) Superimpose image of Pt and sulfur and (l) Line scan of platinum and sulfur.

Transmission electron microscopy (TEM) was performed to enquire physical morphology of the synthesized catalyst. HR-TEM image of Pt@S_{in}/KJ600, Pt@KJ600 and Pt/C are presented in **Figure 6-10(a-c)** respectively. Pt nanoparticles of uniform size found to be uniformly distributed over their respective support materials in Pt@S_{in}/KJ600 and Pt@KJ600 catalyst. There was no evidence of Pt nanoparticle agglomeration due to successful encapsulation of Pt nanoparticle inside pore of KJ600 (Pt@KJ600) and S_{in}/KJ600 (Pt@S_{in}/KJ600) respectively. As proposed due pore-confinement effect, catalyst should possess narrow and uniform particle size

distribution in Pt@KJ600, and this phenomenon should be further enhanced due to strong metal-support interaction in sulfur doped carbon pore (Pt@S_{in}/KJ600). Therefore, to analyze quantitatively particle size distribution was performed on more than 200 nanoparticles of individual catalysts and compared with commercial Pt/C. Average particle size of Pt@S_{in}/KJ600, Pt@KJ600 and Pt/C was calculated as 1.74 ± 0.235 nm, 1.98 ± 0.436 nm and 2.81 ± 0.60 nm respectively (**Figure 6-10**d-f). Such a small particle size with narrow size distribution was attained due to pore-confinement effect and can be seen further reduced in Pt@S_{in}/KJ600. High angle annular dark field scanning transmission electron microscopy (HAADF-STEM) image of Pt@S_{in}/KJ600 and their corresponding elemental mapping of carbon, sulfur and platinum was also performed and shown in **Figure 6-10**(g-k). Uniform distribution of sulfur was realized in the skeletal of KJ600 and have not affected Pt nucleation on the site. Line-scan was also performed over the region and uniform signal of Pt and sulfur was realized over the surface (**Figure 6-10l**). In addition, d-spacing of Pt@KJ600 and Pt@S_{in}/KJ600 and were compared to KJ600 (carbon support) in the literature. KJ600 carbon support exhibits a typical C (002) facet of average d-spacing around 0.337 nm,[44] while d-spacing for Pt@KJ600 (average ~398 nm), whereas largest in Pt@S_{in}/KJ600 (~ 450 nm) due successful incorporation of both Pt and S within carbon skeleton (**Figure 6-11**).[202]

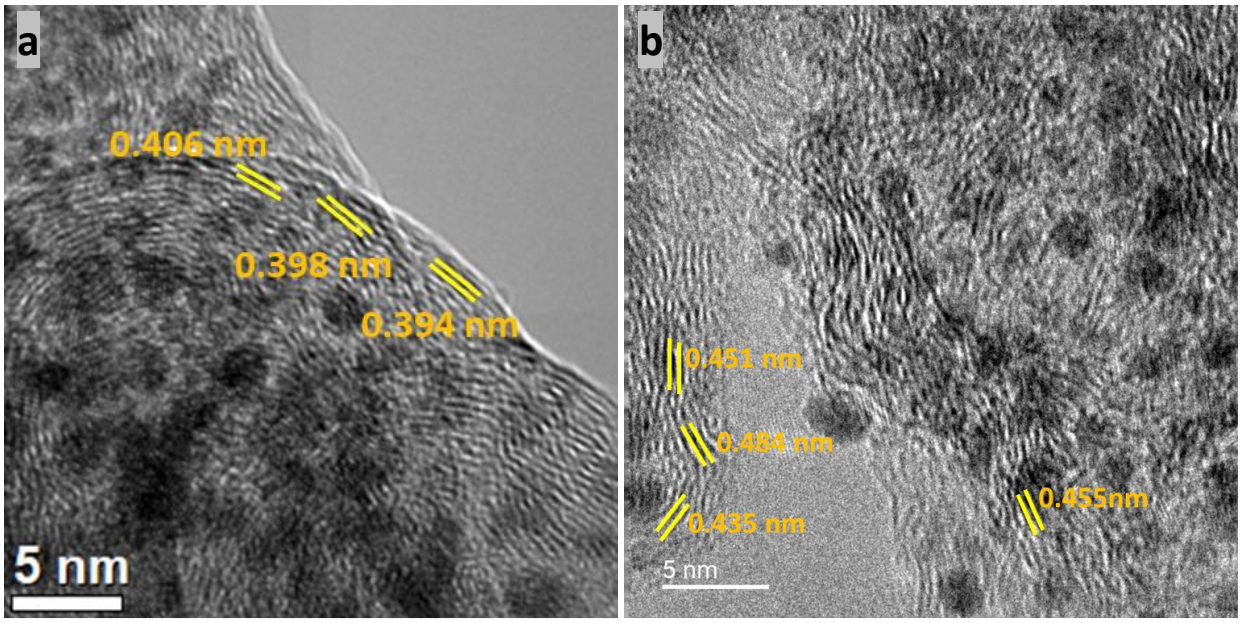

Figure 6-11: HR-TEM image of (a) Pt@KJ600 and (b) Pt@S_{in}/KJ600.

Hitherto, the results and analysis performed have demonstrated the size of Pt nanoparticles in the synthesized catalyst is in the region of carbon support pore-size distribution. Pore-size distribution plot form BET have shown the filling of Pt nanoparticles and sulfur inside pore of carbon. Furthermore, we have realized change in electronic structure of Pt due to both pore-confinement and metal-support interaction in Pt@S_{in}/KJ600, while change in Pt@KJ600 was only due pore-confinement. All the exhibited features have great potential for of an exceptionally durable oxygen reduction catalyst.

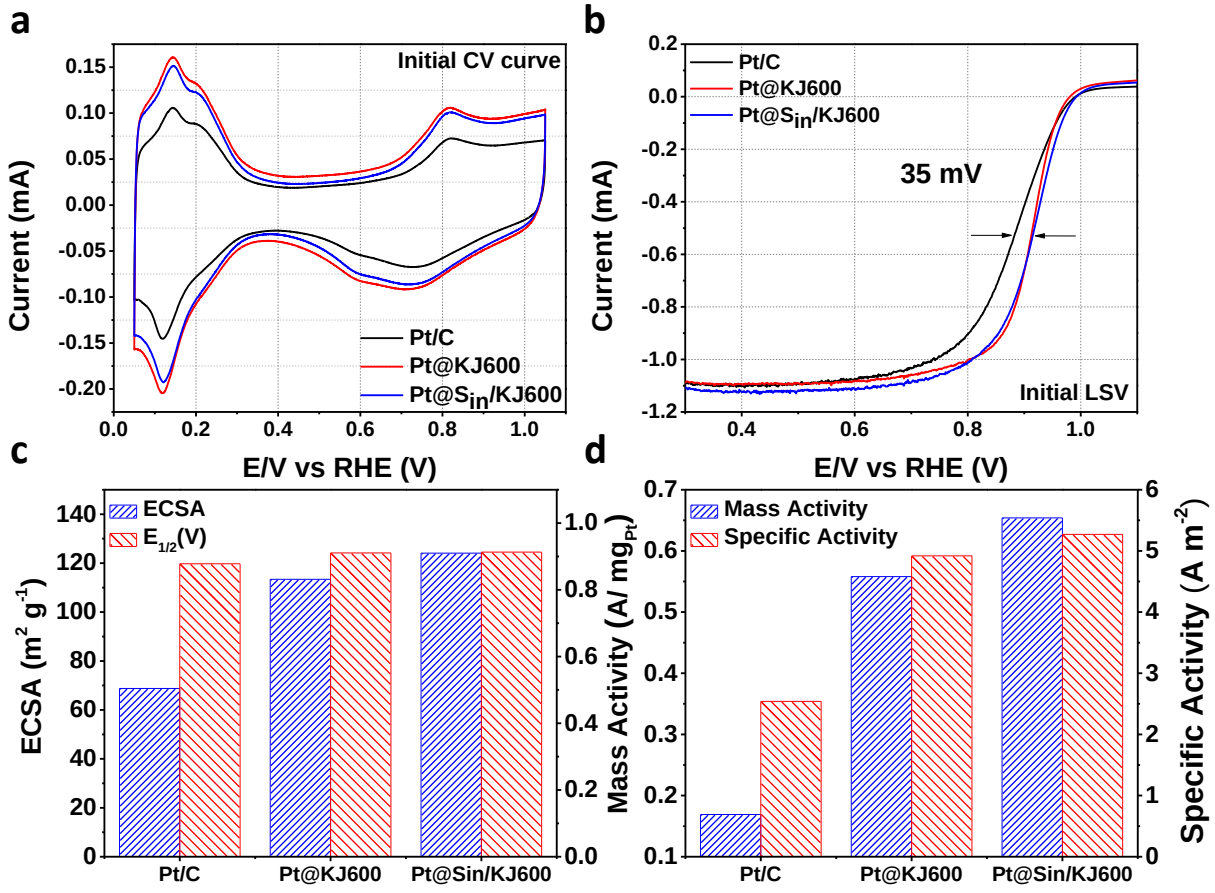

Figure 6-12: (a) Initial CV curves, (b) Initial ORR polarization of Pt@S_{in}/KJ600, Pt@KJ600 and Pt/C respectively; (c) Initial ECSA and half-wave potential and (d) Initial mass activity and specific activity of Pt@S_{in}/KJ600, Pt@KJ600 and Pt/C respectively.

Electrochemical characterization and performance of Pt@S_{in}/KJ600 and Pt@KJ600 were investigated in three cell electrochemical system using rotating disc electrode (RDE) and compared with commercial Pt/C (TKK, 28 percent). Inductively coupled plasma (ICP) test were performed to establish the Pt weight percentage in the synthesized catalyst. Catalyst activation, Pt characteristic peaks and electrochemical active surface area (ECSA) was explored using Potentiodynamic electrochemical measurement technique "Cyclic Voltammetry". Catalyst

activation of Pt@S_{in}/KJ600 and Pt@KJ600 catalysts have taken few more cycles than Pt/C, as Pt nanoparticles were inside nanopore compared to surface in commercial Pt/C catalyst. Few more cycles were taken as wettability of Pt nanoparticles inside the proximity of pore were taken extra time, but as catalyst were activated there were no evidence of any obstruction in catalyst activity.[45] This distinctiveness can also explained as wettability of porous network and carbon channel took more time compared to when nanoparticle was only deposited on the surface. Initial CV curves were recorded in 0.1 M $HClO_4$ solution in N_2 saturated environment at a scan rate of 20 mV s^{-1} **(Figure 6-11a**). The two peaks were observed at 0.146 and O.21 V for Pt@S_{in}/KJ600, 0.14 and 0.21 V for Pt@KJ600 in adsorbed hydrogen region respectively. ECSA was calculated for hydrogen underpotential desorption (HUPD) region between 0.05 to 0.4 V vs RHE and charge density under HUPD were taken as 210 µC cm^{-2} to normalize electrode surface area. ECSA of Pt@S_{in}/KJ600, Pt@KJ600 and Pt/C was calculated as 124.11, 113.40 and 68.78 m^2/g respectively (**Figure 6-11c**). Higher ECSA of synthesized catalyst can be correlated to smaller particle size and narrow particle size distribution due to pore confinement effect. Higher ECSA indicates no obstruction in electrolyte and reactant accessibility on nanoparticle placed in pores, while further slight improvement of ECSA in Pt@S_{in}/KJ600 suggest no negative impact of sulfur doping. Although particle size distribution was further narrowed in case Pt@S_{in}/KJ600 due to further strengthening in metal-support interaction in doped carbon. The ORR polarization curve of Pt@S_{in}/KJ600, Pt@KJ600 and Pt/C was recorded at a scan rate of 10 mV s^{-1} in oxygen saturated 0.1 M $HClO_4$ solution at 1600 rpm. Half-wave potential of Pt@S_{in}/KJ600 is 0.917 V and around 37 mV higher than commercial Pt/C catalyst (**Figure 6-11b**). Initial mass activity of Pt@S_{in}/KJ600

is 0.654 A mg^{-1} at 0.9 V vs RHE, which had crossed the Department of Energy (DOE) 2020 targets (0.44 A mg^{-1}). Mass activity of Pt@S_{in}/KJ600 is 3.87 times higher than commercial Pt/C catalyst (0.169 A mg^{-1}) (**Figure 6-11d**). Specific activity of Pt@S_{in}/KJ600, Pt@KJ600 and Pt/C are 5.27, 4.92 and 2.45 A m^{-2} respectively. Higher mass activity of the Pt@S_{in}/KJ600 catalyst is due ultrafine nanoparticle of average diameter of 1.74 nm, optimized electronic structure, higher Pt(0)/Pt(II) ratio as seen in XPS results and high current density due to change in surface electronic structure which are conditioned by the combination of synthetic and chemical factors due to sulfur doping.[203] Pt@KJ600 catalyst have also shown a mass activity of 0.558 A mg^{-1}, as synthesized with similar route and deposited inside nanopore. Successful synthesis of ultrafine Pt nanoparticles are due pore-confine effect, higher Pt(0)/Pt(II) ratio, while porous interconnected carbon network with high surface area suites large number of active sites which diminishes any reaction kinetics limitations.[45,47] All these factors led to higher ECSA and initial activity of Pt@/KJ600 and Pt@S_{in}/KJ600 compared to Pt/C catalyst. Whereas, slightly higher ECSA and ORR activity of Pt@S_{in}/KJ600 compared to Pt@KJ600 are due to further smaller nanoparticles, narrow particle size distribution due to enhanced metal support interaction and change in surface electronic property due to sulfur doping inside pore of KJ600.

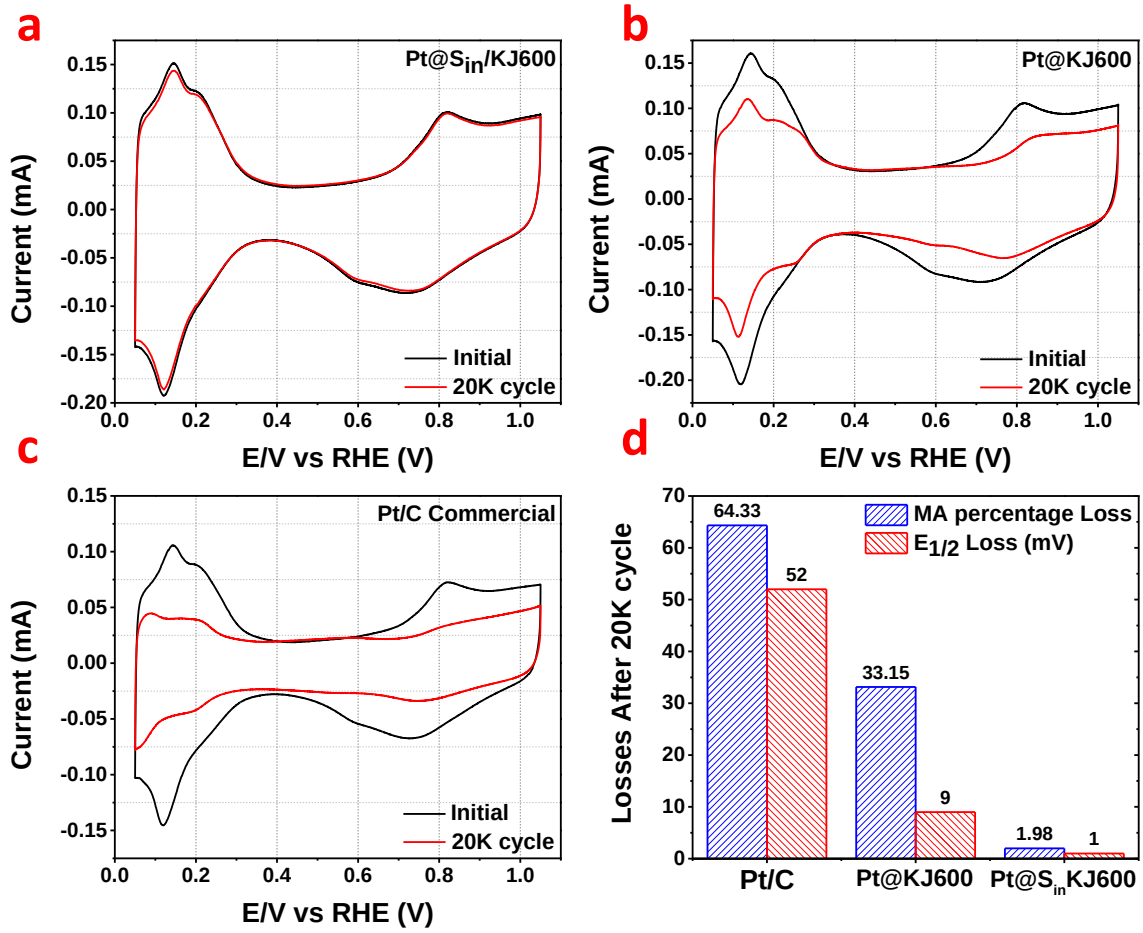

Figure 6-13: Initial and after 20K cycle CV curve comparison, (a) Pt@S_{in}/KJ600, (b) Pt/KJ600, (c) Pt/C, and (d) Mass activity percentage loss and Half-wave potential loss comparison.

Ultrafine nanoparticles are vulnerable to agglomeration and dissolution and one of the most important factors for the loss in activity for ORR. Therefore, stability of the synthesized catalysts was checked by cycling between 0.6-1.1 V vs RHE at a scan rate of 50 mV s^{-1} up to 20000 cycles in N_2 saturated 0.1 M $HClO_4$ solution. To compare ECSA, CV curve before and after 20K cycles were recorded and compared (**Figure 6-12**). ECSA after 20K cycles were 25.80, 78.96 and 108.36 m^2 g^{-1} for Pt/C, Pt@KJ600 and Pt@S_{in}/KJ600 catalyst respectively (**Figure 6-13d**). Pt@KJ600

lost 30 percent of initial ECSA compare 63 percent in Pt/C catalyst, and this can be attributed to pore-confinement effect which kept Pt nanoparticles intact. Whereas, Pt@S_{in}/KJ600 catalyst lost only 13 percent of initial ECSA, this improvement is due interaction between ultrafine Pt nanoparticle and sulfur doping inside pore of carbon (S_{in}/KJ600) which further improved nanoparticles stability. ORR polarization curve was also recorded after 20K cycle and compared with initial curve (**Figure 6-13**a-c). There was merely 1 mV negative loss in half-wave potential for Pt@S_{in}/KJ600 compared to 9mV and 52 mV loss for Pt@KJ600 and Pt/C catalyst respectively. Mass activity of Pt@S_{in}/KJ600, Pt@/KJ600 and Pt/C are 0.640, 0.373 and 0.0619 A mg^{-1} respectively after 20K cycles (**Figure 6-13e**). Pt@S_{in}/KJ600 lost 2 percent while Pt/C have lost 63 percent of their initial mass activity, and mass activity of former was more than 10 times higher than later after 20K cycle respectively (**Figure 6-13**d). Similarly, Pt@/KJ600 also shows great improvement over commercial Pt/C and have lost only 33 percent of its initial activity. Specific activity of Pt@S_{in}/KJ600 is 5.92 A m^{-2} after 20K cycle, which is 12 percent increase compared initial value and almost 2.60 times higher compared Pt/C specific activity after 20K cycle (**Figure 6-13**f). We ascribed excellent ECSA and activity retention of Pt@/KJ600 catalyst due pore-confinement effect which kept Pt nanoparticles intact and reduces nanoparticles agglomeration and dissolution during durability cycle.

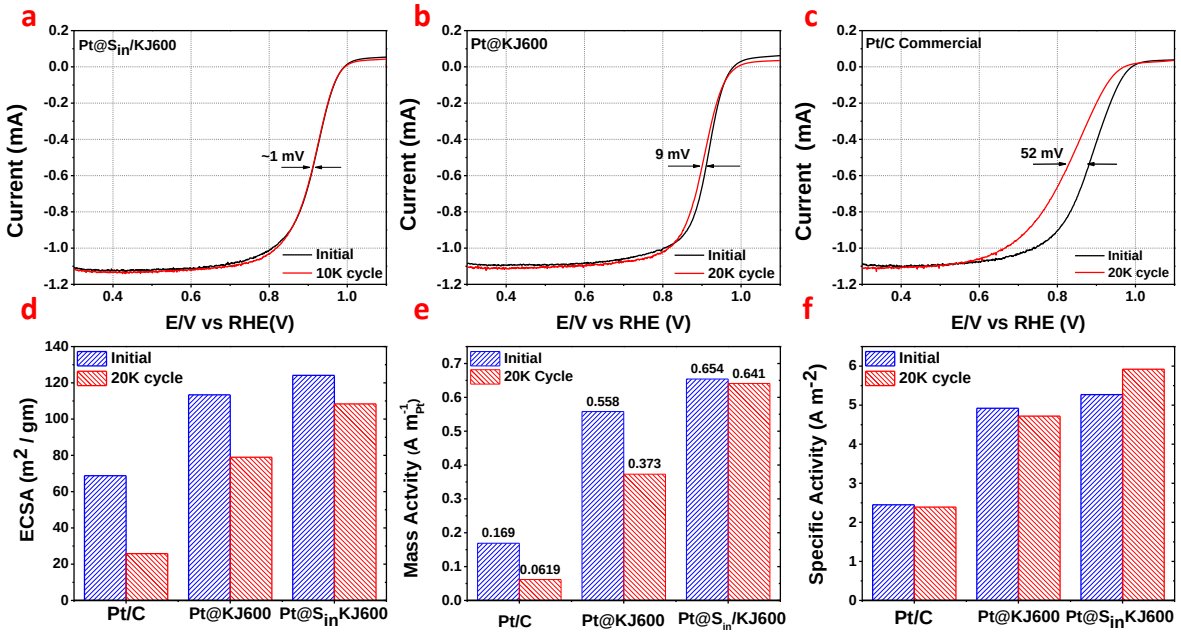

Figure 6-14: (a-c) ORR polarization curve before and after 20K cycles for Pt@Sin/KJ600, Pt@KJ600 and Pt/C respectively; (d) ECSA, (e) mass activity, (f) specific activity, before and after 20K cycles for Pt@Sin/KJ600, Pt@KJ600 and Pt/C respectively.

While ECSA and activity retention further improved when pore of KJ600 were doped with sulfur (S_{in}/KJ600) and followed Pt nanoparticle nucleation within nanopores (Pt@S_{in}/KJ600), which led to improved Pt-support interaction where sulfur act as a linking agent. Therefore, Pt@S_{in}/KJ600 catalyst due combined effect sulfur doping and pore-confinement shown remarkable long-term stability for ORR.

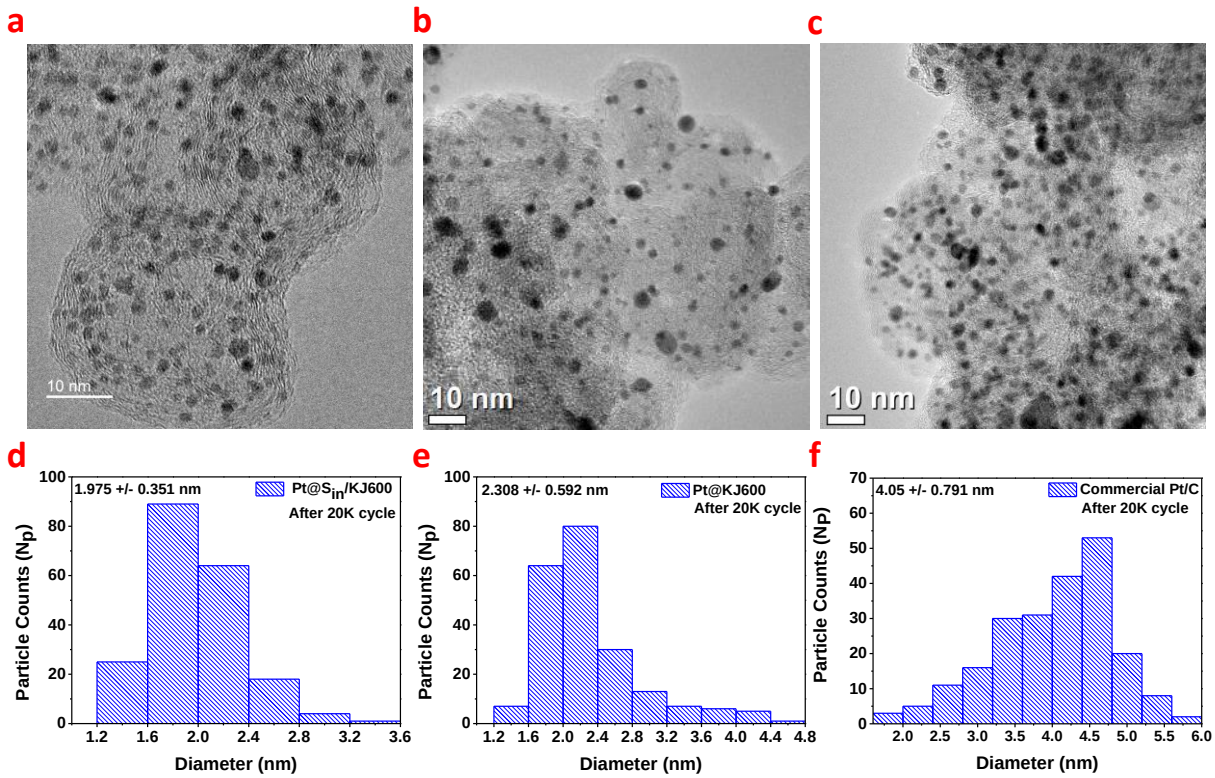

Figure 6-15: HR-TEM image and corresponding particle size distribution of (a-b) Pt/C, (c-d) Pt@KJ600 and (e-f) Pt@S_{in}/KJ600 respectively.

The structural stability of the tested catalysts was assessed with TEM imaging and particle size distribution. Catalyst ink were collected from glassy carbon electrode and preserved in DDI before taken for imaging. TEM image of Pt@S_{in}/KJ600, Pt@KJ600 and Pt/C catalyst and corresponding particle size distribution histogram is presented in the **Figure 6-14**. There was no substantial particle agglomeration or size changes in Pt@S_{in}/KJ600 catalyst (1.975 ± 0.351 nm), while there is a noticeable size increase due to particle agglomeration observed in Pt/C catalyst (4.05 ± 0.791 nm). These results concluded that pore-confinement with doping kept particle intact and provide spatial protection during long-term stability test.

6.4 Conclusion

In this work, we have designed, and successfully synthesized sulfur doped inside pore of KJ600 (S_{in}/KJ600) support and then selectively embedded ultrafine Pt nanoparticles inside pore of support (Pt@S_{in}/KJ600) catalyst. Altogether XRD, BET and TEM results confirmed the uniform dispersion of sub 2 nm Pt nanoparticle deposition with narrow particle size distribution across S_{in}/KJ600 pores. This catalyst realizes excellent mass activity (0.654 A mg^{-1}) due to improved Pt utilization (124.11 m^2 g^{-1}) and optimized electronic structure of Pt due pore confinement and sulfur doping. Moreover, pore-confinement when complemented with sulfur doping it further enhanced metal support interaction with spatial protection within pore effectively suppressed Pt dissolution and aggregation. Pore-confinement controls overgrowth of Pt nanoparticles while sulfur doping increase tethering effect. As a result, Pt@S_{in}/KJ600 catalyst demonstrated excellent stability with loss of 1 mV in half-wave potential and only 2 percent loss of initial mass activity after 20K cycles, compared to Pt/C which lost 52 mV in $E_{1/2}$ potential and 73 percent of initial mass activity. The structural characterization after long-term stability test confirmed unique catalyst design maintained uniform particle size even after 20K cycles. This catalyst synthesis design has great potential other than ORR and are not limited to Pt based catalyst.

Chapter 7: Conclusion and Future work

7.1 Conclusions

The purpose of this thesis was to investigate and develop new catalyst material to improve ORR activity and long-term stability in PEMFCs. The long-term stability of the Pt based catalyst is mostly affected due to agglomeration, Ostwald ripening and dissolution on support material which led to activity decay in addition to loss of a precious metal responsible for the majority PEMFCs cost. We have investigated into new catalyst design to improve Pt utilization and at the same time improve long-term stability of the synthesized catalysts.

In chapter 4, Sulfur doped graphene was synthesized as a support material using flash heat treatment. Polyol method was used to synthesize PtPd core-shell structure as an active catalyst material and was supported on the sulfur doped graphene (PtPd/SG). The synthesized catalyst material was thoroughly characterized physiochemically and their electrochemical activity and stability towards ORR was investigated. Based on TEM, HR-TEM, EDAX line scan core-shell structure of Pt-Pd nanoflower anchored on the SG support material was established. While EELS mapping confirms the interaction between Pt and sulfur doped on graphene, the XPS techniques identified the presence of sulfur as -C-S-C- group embedded in the graphene structure as well as change in electronic structure of sulfur and platinum due to interaction between them. The presence sulfur induced strong metal-support interaction and helps in improvement of long-term electrochemical stability towards ORR. Whereas, the use of Pd alters d-band center, surface atomic arrangement which decreases the chemisorption of oxygen containing species (-OH adsorption considered rate determining step) and positively impact ORR kinetics. Additionally, Pd also acted

as a sacrificial element by turning into anode in Pt-Pd system and exhibits better durability of the synthesized catalyst as observed experimentally. We have demonstrated higher mass and specific activity of 0.371 A mg^{-1} and 4.91 A m^2 respectively. While mass and specific activity of PtPd/SG catalyst after 10K cycles is 25 and 18 folds higher than commercial Pt/C catalyst.

Herein, we have observed increase in mass activity but was still lacking DOE 2025 target of 0.44 A mg^{-1}. In addition, complexity of polyol procedure which require PVP as a reducing agent, capping agent and DEG as a solvent required rigorous washing step, large size of cores-shell structure (10-20 nm), lack of technology to synthesize graphene on large scale, led to our next two projects where we worked to reduce nanoparticle below 2 nm to improve Pt utilization and optimize Pt-C system to improve ORR activity and durability.

In chapter 5, we have a developed a new facile catalyst design to synthesis ultrafine Pt nanoparticles. A facile one-step strategy is easy for adaptation in scale-up production and duplication as use of organic solvent such as EG/DEG, capping agent and reducing agent was avoided. Uniform size ultrafine Pt nanoparticles with average size below 2 nm which increased Pt atom utilization and was embedded inside nanopore of carbon support to suppress agglomeration and Ostwald ripening through pore-confinement effect. This novel strategy endows resultant Pt nanoparticles with an optimized electronic structure which further accelerated ORR kinetics. Synthesized Pt_{inside}/KJ600 catalyst shown remarkable initial activity 0.558 A mg^{-1} at 0.9 V vs RHE (DOE target 0.44 A mg^{-1}), which is 3.30 times higher than Pt/C catalyst and outperforms most of the reported sole Pt based catalyst. To compare $Pt_{outside}$/KJ600 (Pt nanoparticle deposited on the surface of carbon support) was also synthesized and compared with Pt_{inside}/KJ600 and there was

no significant difference observed in ECSA and ORR activity. High ECSA (113.4 m^2 g^{-1}) and ORR activity of Pt_{inside}/KJ600 validates catalyst design as there as was no mass transfer and reaction kinetics limitations observed when Pt nanoparticles was seeded inside carbon nanopore. Moreover, Pt_{inside}/KJ600 exhibits 9 mV negative shift in half-wave potential after 20K cycles, a significant improved over commercial Pt/C catalyst which undergoes 52 mV decays. Mass activity of Pt_{inside}/KJ600 was 6 times higher than Pt/C after 20K cycles, as former lost 31 percent while Pt/C lost 64 percent of initial activity. The structural characterization after durability tests confirms the pore-confinement design effectively inhibit particle agglomeration and kept Pt nanoparticles intact. These results motivate us to further investigate, as this catalyst design is not limited to Pt based catalyst but can easily applicable to the synthesis of Pt based alloy (with transition metal), doping of heteroatoms to further improve Pt nanoparticle stability in ORR conditions. This led us to our next project where we had investigated effect of heteroatoms doping combined with ultrafine Pt nanoparticles deposited inside the pore of carbon support.

Finally, in chapter 6, we have synthesized Pt@S_{in}/KJ600 catalyst, where first sulfur was doped inside the nanopore of carbon support (S_{in}/KJ600) followed with Pt nucleation inside pore of S_{in}/KJ600 results in final catalyst (Pt@S_{in}/KJ600). Sulfur doping improved the catalytic activity by improving conductivity of support material and favors the metal support interaction which improves the particle stability. XPS results confirmed sulfur doping within carbon structure as Thiophenic form and interacted with Pt atom inside nanopores to strengthen metal-support interaction. Ultrafine synthesized catalyst Pt@S_{in}/KJ600 endows exceptional ECSA of 124.11 m^2 g^{-1} and initial activity of 0.654 A mg^{-1}_{Pt} at 0.9V vs RHE, which is 3.87 times higher than initial

mass activity of commercial Pt/C catalyst. Moreover, after 20K cycles Pt@S_{in}/KJ600 (0.641 A mg^{-1}) catalyst had lost merely 1 mV of half-wave potential compared to 52 mV loss in Pt/C (0.0619 A mg^{-1}) after 20K cycles, while mass activity was 10 times higher than Pt/C activity. The performance improvement without affecting reaction kinetics of the synthesized catalyst have clearly demonstrate the sulfur can effectively doped inside pore of carbon support and greatly improve long-term stability of the catalyst. To our best knowledge this is the first study where both doping and active metal catalyst was deposited inside carbon nanopore.

Overall in last two projects first it was established the with this unique method ultrafine Pt nanoparticles can be effectively deposited inside pore and compared when Pt was deposited on the surface. Results have shown improvement in both activity and durability. Secondly, when sulfur was doped it further improved activity but most explicitly long-term stability of the catalyst. Progress in terms of activity and stability of Pt based catalyst presented in this thesis is compiled in table below.

Table 7-1: Catalyst activity and ECSA of synthesized catalyst.

Catalyst	ECSA	Mass Activity	Specific Activity
Pt/C	68.0 $m^2 g^{-1}$	0.169 A mg^{-1}	2.45 A m^{-2}
$Pt_{0.5}Pd_{0.5}$/SG	72.0 $m^2 g^{-1}$	0.115 A mg^{-1}	1.60 A m^{-2}
$Pt_{0.9}Pd_{0.1}$/SG	76.0 $m^2 g^{-1}$	0.371 A mg^{-1}	4.90 A m^{-2}
$Pt_{outside}$/KJ600	114.0 $m^2 g^{-1}$	0.549 A mg^{-1}	4.77 A m^{-2}
Pt_{inside}/KJ600	113.4 $m^2 g^{-1}$	0.558 A mg^{-1}	4.92 A m^{-2}

Pt@S_{in}/KJ600	124.4 m^2 g^{-1}	0.654 A mg^{-1}	5.26 A m^{-2}

DOE 2020 target of 0.44 A mg^{-1}.

7.2 Future Work

Based on the work presented in this thesis future project should focus on the development of catalyst nanoparticle inside pore of carbon support for PEMFCs application. These projects should focus in the following directions. As mentioned in last two projects of this thesis, developed catalyst design is not limited to only Pt based catalyst, but can be further implemented in for Pt-transition metal alloy and heteroatoms doping inside support nanopore. Second part include integration and optimization of these sole Pt, Pt alloy and Pt with heteroatom doped catalyst inside support nanopore catalysts in membrane electrode assembly for full cell testing and optimizations for practical PEMFCs applications.

7.2.1 Electrocatalyst optimization for ORR

Electrocatalyst confined inside pore have shown promising results and can further be investigated for nitrogen doping followed with Platinum deposition inside pore. Nitrogen doped carbon coupled with platinum have shown promising results in catalyzing oxygen reduction reaction. There are different factors affecting pore-confinement such as solvent volume, precursor solubility towards solvent and then solvent affinity (wettability) towards pore nature (hydrophobic and hydrophilic). Therefore, by careful screening few organic nitrogen precursors such as phenylenediamine, Polyaniline and Pyridine can be investigated for successful incorporation inside pore. This can be followed with ultra-low Pt deposition inside pore, procedure has already established in this work. Nitrogen doping can improve ORR activity while further improve

nanoparticle stability. There are few transition metal (Ni, Co, Fe) known to improve catalytic activity tremendously when alloyed with platinum. Pt alloy can be synthesized with similar route to deposit metal catalyst inside pore and can be complemented with doping to further strengthen metal-support interaction. All these synthesized catalysts can be rigorously screened for their physiochemical and electrochemical property. Extensive study needs to be done on long-term stability of the catalyst material, as pore-confinement effectively control particle size while provide spatial protection from Ostwald ripening, particle agglomeration and dissolution. Initial study includes half cell testing for reaction kinetics and activity investigation and then followed with different ADT procedure recommended from DOE to study particle stability on carbon support for ORR (0.05-1.5 V vs RHE). Physiochemical study will be performed to elucidate change in particle size distribution, properties and structure of the catalyst after long-term stability test. Once electrocatalyst screened thoroughly they will be taken to MEA assembly for PEMFCs application.

7.2.2 Membrane electrode assembly integration

The utmost goal of these project is the integration of ORR catalyst developed in these works into membrane electrode assembly to accelerate wide-spread application of PEMFCs. The performance and activity test in full cell setup will help in the realization of developed catalyst technology into PEMFCs automotive application. Optimization of catalyst layer in MEA setup depends on several factors such as catalyst ink composition, catalyst deposition technique, loading etc. Catalyst ink preparation required screening of suitable solvent such as ethanol, isopropanol, DDI and their mixtures compositions.[204] Ionomers (Nafion): solvent ratio, catalyst layer thickness need to be controlled to improve Pt utilization in MEA setup. For catalyst deposition, spraying can

be done on either Nafion membrane called catalyst coated membrane or deposited on gas diffusion layer (GDL). Both methods can be used to improve Pt utilization and impede mass transfer limitations to have a positive effect MEA performance. Once the best solvent, ionomers to solvent ratio and coating methods is established, the electrode thickness and catalyst loading can be varied to determine the impact on PEMFCs performance. All these variables study will give a better understanding of MEA performance and can be realized in other Pt-C catalyst system as well.

Letters of Copyright Permission

1. John Wiley and Sons / Advanced Materials Interfaces

JOHN WILEY AND SONS LICENSE
TERMS AND CONDITIONS
Mar 22, 2020

This Agreement between 245 Lester Street ("You") and John Wiley and Sons ("John Wiley and Sons") consists of your license details and the terms and conditions provided by John Wiley and Sons and Copyright Clearance Center.

License Number	4794360646627
License date	Mar 22, 2020
Licensed Content Publisher	John Wiley and Sons
Licensed Content Publication	Advanced Materials Interfaces
Licensed Content Title	Platinum‐Palladium Core‐Shell Nanoflower Catalyst with Improved Activity and Excellent Durability for the Oxygen Reduction Reaction
Licensed Content Author	Zhongwei Chen, Md Ariful Hoque, Zachary P. Cano, et al
Licensed Content Date	Jan 31, 2018
Licensed Content Volume	5
Licensed Content Issue	7
Licensed Content Pages	8
Type of use	Dissertation/Thesis
Requestor type	Author of this Wiley article
Format	Electronic
Portion	Full article
Will you be translating?	No
Title of your thesis/dissertation	Nanostructured catalyst design to improve ultrafine Pt nanoparticle utilization and stability for PEMFCs
Expected completion date	May 2020
Expected size (number of pages)	190
Requestor Location	Mohd Altamash Jauhar Department of Chemical Engineering University of Waterloo

	200 University Avenue West Waterloo, ON N2L 3G1 Canada Attn: Mohd Altamash Jauhar
Publisher Tax ID	EU826007151
Total	0.00 USD
Terms and Conditions	

TERMS AND CONDITIONS

This copyrighted material is owned by or exclusively licensed to John Wiley & Sons, Inc. or one of its group companies (each a"Wiley Company") or handled on behalf of a society with which a Wiley Company has exclusive publishing rights in relation to a particular work 3/22/2020 RightsLink Printable License https://s100.copyright.com/AppDispatchServlet 3/6 (collectively "WILEY"). By clicking "accept" in connection with completing this licensing transaction, you agree that the following terms and conditions apply to this transaction (along with the billing and payment terms and conditions established by the Copyright Clearance Center Inc., ("CCC's Billing and Payment terms and conditions"), at the time that you opened your RightsLink account (these are available at any time at http://myaccount.copyright.com).

Terms and Conditions

- The materials you have requested permission to reproduce or reuse (the "Wiley Materials") are protected by copyright.

- You are hereby granted a personal, non-exclusive, non-sub licensable (on a standalone basis), non-transferable, worldwide, limited license to reproduce the Wiley Materials for the purpose specified in the licensing process. This license, **and any CONTENT (PDF or image file) purchased as part of your order,** is for a one-time use only and limited to any maximum distribution number specified in the license. The first instance of republication or reuse granted by this license must be completed within two years of the date of the grant of this license (although copies prepared before the end date may be distributed thereafter). The Wiley Materials shall not be used in any other manner or for any other purpose, beyond what is granted in the license. Permission is granted subject to an appropriate acknowledgement given to the author, title of the material/book/journal and the publisher. You shall also duplicate the copyright notice that appears in the Wiley publication in your use of the Wiley Material. Permission is also granted on the understanding that nowhere in the text is a previously published source acknowledged for all or part of this Wiley Material. Any third party content is expressly excluded from this permission.

- With respect to the Wiley Materials, all rights are reserved. Except as expressly granted by the terms of the license, no part of the Wiley Materials may be copied, modified, adapted

(except for minor reformatting required by the new Publication), translated, reproduced, transferred or distributed, in any form or by any means, and no derivative works may be made based on the Wiley Materials without the prior permission of the respective copyright owner. **For STM Signatory Publishers clearing permission under the terms of the STM Permissions Guidelines only, the terms of the license are extended to include subsequent editions and for editions in other languages, provided such editions are for the work as a whole in situ and does not involve the separate exploitation of the permitted figures or extracts,** You may not alter, remove or suppress in any manner any copyright, trademark or other notices displayed by the Wiley Materials. You may not license, rent, sell, loan, lease, pledge, offer as security, transfer or assign the Wiley Materials on a stand-alone basis, or any of the rights granted to you hereunder to any other person.

- The Wiley Materials and all of the intellectual property rights therein shall at all times remain the exclusive property of John Wiley & Sons Inc, the Wiley Companies, or their respective licensors, and your interest therein is only that of having possession of and the right to reproduce the Wiley Materials pursuant to Section 2 herein during the continuance of this Agreement. You agree that you own no right, title or interest in or to the Wiley Materials or any of the intellectual property rights therein. You shall have no rights hereunder other than the license as provided for above in Section 2. No right, license or interest to any trademark, trade name, service mark or other branding ("Marks") of WILEY or its licensors is granted hereunder, and you agree that you shall not assert any such right, license or interest with respect thereto

- NEITHER WILEY NOR ITS LICENSORS MAKES ANY WARRANTY OR REPRESENTATION OF ANY KIND TO YOU OR ANY THIRD PARTY, EXPRESS, IMPLIED OR STATUTORY, WITH RESPECT TO THE MATERIALS OR THE ACCURACY OF ANY INFORMATION CONTAINED IN THE MATERIALS, INCLUDING, WITHOUT LIMITATION, ANY IMPLIED WARRANTY OF MERCHANTABILITY, ACCURACY, SATISFACTORY QUALITY, FITNESS FOR A PARTICULAR PURPOSE, USABILITY, INTEGRATION OR NON-INFRINGEMENT AND ALL SUCH WARRANTIES ARE HEREBY EXCLUDED BY WILEY AND ITS LICENSORS AND WAIVED BY YOU.

- WILEY shall have the right to terminate this Agreement immediately upon breach of this Agreement by you.

- You shall indemnify, defend and hold harmless WILEY, its Licensors and their respective directors, officers, agents and employees, from and against any actual or threatened claims, demands, causes of action or proceedings arising from any breach of this Agreement by you.

- IN NO EVENT SHALL WILEY OR ITS LICENSORS BE LIABLE TO YOU OR ANY OTHER PARTY OR ANY OTHER PERSON OR ENTITY FOR ANYSPECIAL, CONSEQUENTIAL, INCIDENTAL, INDIRECT, EXEMPLARY OR PUNITIVE DAMAGES, HOWEVER CAUSED, ARISING OUT OF OR IN CONNECTION WITH THE DOWNLOADING, PROVISIONING, VIEWING OR USE OF THE MATERIALS REGARDLESS OF THE FORM OF ACTION, WHETHER FOR BREACH OF CONTRACT, BREACH OF WARRANTY, TORT, NEGLIGENCE, INFRINGEMENT OR OTHERWISE (INCLUDING, WITHOUT LIMITATION, DAMAGES BASED ON LOSS OF PROFITS, DATA, FILES, USE, BUSINESS OPPORTUNITY OR CLAIMS OF THIRD PARTIES), AND WHETHER OR NOT THE PARTY HAS BEEN ADVISED OF THE POSSIBILITY OF SUCH DAMAGES. THIS LIMITATION SHALL APPLY NOTWITHSTANDING ANY FAILURE OF ESSENTIAL PURPOSE OF ANY LIMITED REMEDY PROVIDED HEREIN.

- Should any provision of this Agreement be held by a court of competent jurisdiction to be illegal, invalid, or unenforceable, that provision shall be deemed amended to achieve as nearly as possible the same economic effect as the original provision, and the legality, validity and enforceability of the remaining provisions of this Agreement shall not be affected or impaired thereby. The failure of either party to enforce any term or condition of this Agreement shall not constitute a waiver of either party's right to enforce each and every term and condition of this Agreement. No breach under this agreement shall be deemed waived or excused by either party unless such waiver or consent is in writing signed by the party granting such waiver or consent. The waiver by or consent of a party to a breach of any provision of this Agreement shall not operate or be construed as a waiver of or consent to any other or subsequent breach by such other party.

- This Agreement may not be assigned (including by operation of law or otherwise) by you without WILEY's prior written consent.

- Any fee required for this permission shall be non-refundable after thirty (30) days from receipt by the CCC.

- These terms and conditions together with CCC's Billing and Payment terms and conditions (which are incorporated herein) form the entire agreement between you and WILEY concerning this licensing transaction and (in the absence of fraud) supersedes all prior agreements and representations of the parties, oral or written. This Agreement may not be amended except in writing signed by both parties. This Agreement shall be binding upon and inure to the benefit of the parties' successors, legal representatives, and authorized assigns.

- In the event of any conflict between your obligations established by these terms and conditions and those established by CCC's Billing and Payment terms and conditions, these terms and conditions shall prevail.

- WILEY expressly reserves all rights not specifically granted in the combination of (i) the license details provided by you and accepted in the course of this licensing transaction, (ii) these terms and conditions and (iii) CCC's Billing and Payment terms and conditions.

- This Agreement will be void if the Type of Use, Format, Circulation, or Requestor Type was misrepresented during the licensing process.

- This Agreement shall be governed by and construed in accordance with the laws of the State of New York, USA, without regards to such state's conflict of law rules. Any legal action, suit or proceeding arising out of or relating to these Terms and Conditions or the breach thereof shall be instituted in a court of competent jurisdiction in New York County in the State of New York in the United States of America and each party hereby consents and submits to the personal jurisdiction of such court, waives any objection to venue in such court and consents to service of process by registered or certified mail, return receipt requested, at the last known address of such party.

WILEY OPEN ACCESS TERMS AND CONDITIONS

Wiley Publishes Open Access Articles in fully Open Access Journals and in Subscription journals offering Online Open. Although most of the fully Open Access journals publish open access articles under the terms of the Creative Commons Attribution (CC BY) License only, the subscription journals and a few of the Open Access Journals offer a choice of Creative Commons Licenses. The license type is clearly identified on the article.

The Creative Commons Attribution License

The Creative Commons Attribution License (CC-BY) allows users to copy, distribute and transmit an article, adapt the article and make commercial use of the article. The CC-BY license permits commercial and non-

Creative Commons Attribution Non-Commercial License

The Creative Commons Attribution Non-Commercial (CC-BY-NC) License permits use, distribution and reproduction in any medium, provided the original work is properly cited and is not used for commercial purposes. (see below)

Creative Commons Attribution-Non-Commercial-NoDerivs License

References

(1) U.S. Doe. *Fuel Cells Technical Plan*; 2012.

(2) FUEL CELL TECHNOLOGIES OFFICE. DOE Technical Targets for Polymer Electrolyte Membrane Fuel Cell Components https://www.energy.gov/eere/fuelcells/doe-technical-targets-polymer-electrolyte-membrane-fuel-cell-components.

(3) Jason Marcinkoski, Jacob Spendelow, A. W.; Papageorgopoulos, D. *DOE Hydrogen and Fuel Cells Program Record*; Washington, DC, 2015.

(4) Bennaceur, K.; Clark, B.; Orr, F. M.; Ramakrishnan, T. S.; Roulet, C.; Stout, E. Hydrogen : A Future Energy Carrier? *Oilf. Rev.* **2005**, 30–41 DOI: 10.1002/9783527622894.

(5) Haryanto, A.; Fernando, S.; Murali, N.; Adhikari, S. Current status of hydrogen production techniques by steam reforming of ethanol: A review. *Energy and Fuels* **2005**, *19* (5), 2098–2106 DOI: 10.1021/ef0500538.

(6) Pollet, B. G.; Staffell, I.; Shang, J. L. Current status of hybrid, battery and fuel cell electric vehicles: From electrochemistry to market prospects. *Electrochim. Acta* **2012**, *84*, 235–249 DOI: 10.1016/j.electacta.2012.03.172.

(7) Supported, P.; Cell, F.; Program, T. Pathways to Commercial Success : *Technology* **2010**, No. August.

(8) Larminie, J.; Dicks, A. *Fuel cell systems explained*; 2003.

(9) Bressmann, T. Self-inflicted cosmetic tongue split: a case report. *J. Can. Dent. Assoc.* **2004**, *70* (3), 156–157 DOI: 10.1002/adfm.201200186.

(10) Steele, B. C. H.; Heinzel, A. Materials for fuel-cell technologies. **2001**, *414* (November),

345–352.

(11) Song, C.; Zhang, J. Electrocatalytic oxygen reduction reaction. *PEM Fuel Cell Electrocatal. Catal. Layers Fundam. Appl.* **2008**, 89–134 DOI: 10.1007/978-1-84800-936-3_2.

(12) Debe, M. K. Electrocatalyst approaches and challenges for automotive fuel cells. *Nature* **2012**, *486* (7401), 43–51 DOI: 10.1038/nature11115.

(13) Borup, R.; Meyers, J.; Pivovar, B.; Kim, Y. S.; Mukundan, R.; Garland, N.; Myers, D.; Wilson, M.; Garzon, F.; Wood, D.; et al. Scientific aspects of polymer electrolyte fuel cell durability and degradation. *Chem. Rev.* **2007**, *107* (10), 3904–3951 DOI: 10.1021/cr050182l.

(14) Meyers, J. P.; Mcgrath, J. E.; Borup, R.; Meyers, J.; Pivovar, B.; Kim, Y. S.; Mukundan, R.; Garland, N.; Myers, D.; Wilson, M.; et al. Scientific Aspects of Polymer Electrolyte Fuel Cell Durability and Degradation . Chemical Scientific Aspects of Polymer Electrolyte Fuel Cell Durability and Degradation. **2007**, *107* (NOVEMBER), 3904–3951 DOI: 10.1021/cr050182l.

(15) Macauley, N.; Papadias, D. D.; Fairweather, J.; Spernjak, D.; Langlois, D.; Ahluwalia, R.; More, K. L.; Mukundan, R.; Borup, R. L. Carbon corrosion in PEM fuel cells and the development of accelerated stress tests. *J. Electrochem. Soc.* **2018**, *165* (6), F3148–F3160 DOI: 10.1149/2.0061806jes.

(16) Borup, R. L.; Davey, J. R.; Garzon, F. H.; Wood, D. L.; Inbody, M. A. PEM fuel cell electrocatalyst durability measurements. *J. Power Sources* **2006**, *163* (1 SPEC. ISS.), 76–81 DOI: 10.1016/j.jpowsour.2006.03.009.

(17) Yousfi-Steiner, N.; Moçotéguy, P.; Candusso, D.; Hissel, D. A review on polymer electrolyte membrane fuel cell catalyst degradation and starvation issues: Causes, consequences and diagnostic for mitigation. *J. Power Sources* **2009**, *194* (1), 130–145 DOI: 10.1016/j.jpowsour.2009.03.060.

(18) Yu, X.; Ye, S. Recent advances in activity and durability enhancement of Pt/C catalytic cathode in PEMFC. Part II: Degradation mechanism and durability enhancement of carbon supported platinum catalyst. *J. Power Sources* **2007**, *172* (1), 145–154 DOI: 10.1016/j.jpowsour.2007.07.048.

(19) Maass, S.; Finsterwalder, F.; Frank, G.; Hartmann, R.; Merten, C. Carbon support oxidation in PEM fuel cell cathodes. *J. Power Sources* **2008**, *176* (2), 444–451 DOI: 10.1016/j.jpowsour.2007.08.053.

(20) Wang, X.; Kumar, R.; Myers, D. J. Effect of Voltage on Platinum Dissolution. *Electrochem. Solid-State Lett.* **2006**, *9* (5), A225 DOI: 10.1149/1.2180536.

(21) Shao, Y.; Yin, G.; Gao, Y. Understanding and approaches for the durability issues of Pt-based catalysts for PEM fuel cell. *J. Power Sources* **2007**, *171* (2), 558–566 DOI: 10.1016/j.jpowsour.2007.07.004.

(22) Wu, J.; Yuan, X. Z.; Martin, J. J.; Wang, H.; Zhang, J.; Shen, J.; Wu, S.; Merida, W. A review of PEM fuel cell durability: Degradation mechanisms and mitigation strategies. *J. Power Sources* **2008**, *184* (1), 104–119 DOI: 10.1016/j.jpowsour.2008.06.006.

(23) de Bruijn, F. A.; Dam, V. A. T.; Janssen, G. J. M. Review: Durability and Degradation Issues of PEM Fuel Cell Components. *Fuel Cells* **2008**, *8* (1), 3–22 DOI:

10.1002/fuce.200700053.

(24) Virkar, A. V.; Zhou, Y. Mechanism of Catalyst Degradation in Proton Exchange Membrane Fuel Cells. *J. Electrochem. Soc.* **2007**, *154* (6), B540 DOI: 10.1149/1.2722563.

(25) Roen, L. M.; Paik, C. H.; Jarvi, T. D. Electrocatalytic Corrosion of Carbon Support in PEMFC Cathodes. *Electrochem. Solid-State Lett.* **2004**, *7* (1), A19 DOI: 10.1149/1.1630412.

(26) Laconti, A.; Liu, H.; Mittelsteadt, C.; McDonald, R. Polymer Electrolyte Membrane Degradation Mechanisms in Fuel Cells - Findings Over the Past 30 Years and Comparison with Electrolyzers. In *ECS Transactions*; ECS, 2006; Vol. 1, pp 199–219.

(27) Tang, H.; Peikang, S.; Jiang, S. P.; Wang, F.; Pan, M. A degradation study of Nafion proton exchange membrane of PEM fuel cells. *J. Power Sources* **2007**, *170* (1), 85–92 DOI: 10.1016/j.jpowsour.2007.03.061.

(28) Ouyang, R.; Liu, J.-X.; Li, W.-X. Atomistic Theory of Ostwald Ripening and Disintegration of Supported Metal Particles under Reaction Conditions. *J. Am. Chem. Soc.* **2013**, *135* (5), 1760–1771 DOI: 10.1021/ja3087054.

(29) Hansen, T. W.; DeLaRiva, A. T.; Challa, S. R.; Datye, A. K. Sintering of Catalytic Nanoparticles: Particle Migration or Ostwald Ripening? *Acc. Chem. Res.* **2013**, *46* (8), 1720–1730 DOI: 10.1021/ar3002427.

(30) Wettergren, K.; Schweinberger, F. F.; Deiana, D.; Ridge, C. J.; Crampton, A. S.; Rötzer, M. D.; Hansen, T. W.; Zhdanov, V. P.; Heiz, U.; Langhammer, C. High sintering resistance of size-selected platinum cluster catalysts by suppressed ostwald ripening. *Nano Lett.* **2014**,

14 (10), 5803–5809 DOI: 10.1021/nl502686u.

(31) Parker, S. C.; Campbell, C. T. Kinetic model for sintering of supported metal particles with improved size-dependent energetics and applications to Au on TiO2 (110). *Phys. Rev. B - Condens. Matter Mater. Phys.* **2007**, *75* (3), 1–15 DOI: 10.1103/PhysRevB.75.035430.

(32) Campbell, C. T. The energetics of supported metal nanoparticles: relationships to sintering rates and catalytic activity. *Acc. Chem. Res.* **2013**, *46* (8), 1712–1719 DOI: 10.1021/ar3003514.

(33) Wang, Y.-J.; Fang, B.; Li, H.; Bi, X. T.; Wang, H. Progress in modified carbon support materials for Pt and Pt-alloy cathode catalysts in polymer electrolyte membrane fuel cells. *Prog. Mater. Sci.* **2016**, *82*, 445–498 DOI: 10.1016/j.pmatsci.2016.06.002.

(34) Wang, Y.-J.; Wilkinson, D. P.; Zhang, J. Noncarbon support materials for polymer electrolyte membrane fuel cell electrocatalysts. *Chem. Rev.* **2011**, *111* (12), 7625–7651 DOI: 10.1021/cr100060r.

(35) Zhou, X.; Qiao, J.; Yang, L.; Zhang, J. A review of graphene-based nanostructural materials for both catalyst supports and metal-free catalysts in PEM fuel cell oxygen reduction reactions. *Adv. Energy Mater.* **2014**, *4* (8), 1–25 DOI: 10.1002/aenm.201301523.

(36) Yang, Z.; Yao, Z.; Li, G.; Fang, G.; Nie, H.; Liu, Z.; Zhou, X.; Chen, X.; Huang, S. Sulfur-Doped Graphene as an Efficient Metal-free Cathode Catalyst for Oxygen Reduction. *ACS Nano* **2012**, *6* (1), 205–211 DOI: 10.1021/nn203393d.

(37) Higgins, D.; Zamani, P.; Yu, A.; Chen, Z. The application of graphene and its composites in oxygen reduction electrocatalysis: A perspective and review of recent progress. *Energy*

Environ. Sci. **2016**, *9* (2), 357–390 DOI: 10.1039/c5ee02474a.

(38) Dreyer, D. R.; Park, S.; Bielawski, C. W.; Ruoff, R. S. The chemistry of graphene oxide. *Chem. Soc. Rev.* **2010**, *39* (1), 228–240 DOI: 10.1039/b917103g.

(39) Li, D.; Kaner, R. B. Graphene-Based Materials. **2008**, *320* (May).

(40) Hoque, M. A.; Hassan, F. M.; Seo, M. H.; Choi, J. Y.; Pritzker, M.; Knights, S.; Ye, S.; Chen, Z. Optimization of sulfur-doped graphene as an emerging platinum nanowires support for oxygen reduction reaction. *Nano Energy* **2016**, *19*, 27–38 DOI: 10.1016/j.nanoen.2015.11.004.

(41) Chen, D.; Feng, H.; Li, J. Graphene oxide: Preparation, functionalization, and electrochemical applications. *Chem. Rev.* **2012**, *112* (11), 6027–6053 DOI: 10.1021/cr300115g.

(42) Li, Y.; Zhou, W.; Wang, H.; Xie, L.; Liang, Y.; Wei, F.; Idrobo, J.-C.; Pennycook, S. J.; Dai, H. An oxygen reduction electrocatalyst based on carbon nanotube–graphene complexes. *Nat. Nanotechnol.* **2012**, *7* (6), 394–400 DOI: 10.1038/nnano.2012.72.

(43) Novoselov, K. S.; Fal′ko, V. I.; Colombo, L.; Gellert, P. R.; Schwab, M. G.; Kim, K. A roadmap for graphene. *Nature*. Nature Publishing Group 2012, pp 192–200.

(44) Zhang, Z.; Deng, Y.-P.; Xing, Z.; Luo, D.; Sy, S.; Cano, Z. P.; Liu, G.; Jiang, Y.; Chen, Z. “Ship in a Bottle” Design of Highly Efficient Bifunctional Electrocatalysts for Long-Lasting Rechargeable Zn–Air Batteries. *ACS Nano* **2019**, *13* (6), 7062–7072 DOI: 10.1021/acsnano.9b02315.

(45) Galeano, C.; Meier, J. C.; Peinecke, V.; Bongard, H.; Katsounaros, I.; Topalov, A. A.; Lu,

A.; Mayrhofer, K. J. J.; Schüth, F. Toward highly stable electrocatalysts via nanoparticle pore confinement. *J. Am. Chem. Soc.* **2012**, *134* (50), 20457–20465 DOI: 10.1021/ja308570c.

(46) Knossalla, J.; Paciok, P.; Göhl, D.; Jalalpoor, D.; Pizzutilo, E.; Mingers, A. M.; Heggen, M.; Dunin-Borkowski, R. E.; Mayrhofer, K. J. J.; Schüth, F.; et al. Shape-Controlled Nanoparticles in Pore-Confined Space. *J. Am. Chem. Soc.* **2018**, *140* (46), 15684–15689 DOI: 10.1021/jacs.8b07868.

(47) Baldizzone, C.; Mezzavilla, S.; Carvalho, H. W. P.; Meier, J. C.; Schuppert, A. K.; Heggen, M.; Galeano, C.; Grunwaldt, J.-D.; Schüth, F.; Mayrhofer, K. J. J. Confined-Space Alloying of Nanoparticles for the Synthesis of Efficient PtNi Fuel-Cell Catalysts. *Angew. Chemie Int. Ed.* **2014**, *53* (51), 14250–14254 DOI: 10.1002/anie.201406812.

(48) Banham, D.; Feng, F.; Fürstenhaupt, T.; Ye, S.; Birss, V. First time investigation of Pt nanocatalysts deposited inside carbon mesopores of controlled length and diameter. *J. Mater. Chem.* **2012**, *22* (15), 7164 DOI: 10.1039/c2jm00137c.

(49) Aijaz, A.; Karkamkar, A.; Choi, Y. J.; Tsumori, N.; Rönnebro, E.; Autrey, T.; Shioyama, H.; Xu, Q. Immobilizing highly catalytically active Pt nanoparticles inside the pores of metal-organic framework: A double solvents approach. *J. Am. Chem. Soc.* **2012**, *134* (34), 13926–13929 DOI: 10.1021/ja3043905.

(50) Ma, Z.; Li, S.; Wu, L.; Song, L.; Jiang, G.; Liang, Z.; Su, D.; Zhu, Y.; Adzic, R. R.; Wang, J. X.; et al. NbOx nano-nail with a Pt head embedded in carbon as a highly active and durable oxygen reduction catalyst. *Nano Energy* **2020**, *69* (January), 104455 DOI:

10.1016/j.nanoen.2020.104455.

(51) Hayashi, A.; Kimijima, K.; Miyamoto, J.; Yagi, I. Direct Observation of Well-dispersed Pt Nanoparticles inside the Pores of Mesoporous Carbon through the Cross Section of Pt/Mesoporous Carbon Particles. *Chem. Lett.* **2009**, *38* (4), 346–347 DOI: 10.1246/cl.2009.346.

(52) National institute of standards and technology https://physics.nist.gov/MajResFac/NIF/pemFuelCells.html.

(53) De Bruijn, F. A.; Dam, V. A. T.; Janssen, G. J. M. Review: Durability and degradation issues of PEM fuel cell components. *Fuel Cells* **2008**, *8* (1), 3–22 DOI: 10.1002/fuce.200700053.

(54) Shao, M.; Chang, Q.; Dodelet, J.-P.; Chenitz, R. Recent Advances in Electrocatalysts for Oxygen Reduction Reaction. *Chem. Rev.* **2016**, *116* (6), 3594–3657 DOI: 10.1021/acs.chemrev.5b00462.

(55) Shinozaki, K.; Zack, J. W.; Richards, R. M.; Pivovar, B. S.; Kocha, S. S. Oxygen Reduction Reaction Measurements on Platinum Electrocatalysts Utilizing Rotating Disk Electrode Technique. *J. Electrochem. Soc.* **2015**, *162* (10), F1144–F1158 DOI: 10.1149/2.1071509jes.

(56) Zhang, S.; Yuan, X.; Wang, H.; Mérida, W.; Zhu, H.; Shen, J.; Wu, S.; Zhang, J. A review of accelerated stress tests of MEA durability in PEM fuel cells. *Int. J. Hydrogen Energy* **2009**, *34* (1), 388–404 DOI: 10.1016/j.ijhydene.2008.10.012.

(57) Hartl, K.; Hanzlik, M.; Arenz, M. IL-TEM investigations on the degradation mechanism of Pt/C electrocatalysts with different carbon supports. *Energy Environ. Sci.* **2011**, *4* (1), 234–

238 DOI: 10.1039/C0EE00248H.

(58) Roduner, E. Size matters: why nanomaterials are different. *Chem. Soc. Rev.* **2006**, *35* (7), 583 DOI: 10.1039/b502142c.

(59) Goodman, E. D.; Schwalbe, J. A.; Cargnello, M. Mechanistic Understanding and the Rational Design of Sinter-Resistant Heterogeneous Catalysts. *ACS Catal.* **2017**, *7* (10), 7156–7173 DOI: 10.1021/acscatal.7b01975.

(60) Shao, Y.; Zhang, S.; Wang, C.; Nie, Z.; Liu, J.; Wang, Y.; Lin, Y. Highly durable graphene nanoplatelets supported Pt nanocatalysts for oxygen reduction. *J. Power Sources* **2010**, *195* (15), 4600–4605 DOI: 10.1016/j.jpowsour.2010.02.044.

(61) Hoque, M. A.; Hassan, F. M.; Seo, M.-H.; Choi, J.-Y.; Pritzker, M.; Knights, S.; Ye, S.; Chen, Z. Optimization of sulfur-doped graphene as an emerging platinum nanowires support for oxygen reduction reaction. *Nano Energy* **2016**, *19*, 27–38 DOI: 10.1016/j.nanoen.2015.11.004.

(62) Liang, J.; Du, X.; Gibson, C.; Du, X. W.; Qiao, S. Z. N-doped graphene natively grown on hierarchical ordered porous carbon for enhanced oxygen reduction. *Adv. Mater.* **2013**, *25* (43), 6226–6231 DOI: 10.1002/adma.201302569.

(63) Sun, S.; Zhang, G.; Geng, D.; Chen, Y.; Banis, M. N.; Li, R.; Cai, M.; Sun, X. Direct growth of single-crystal Pt nanowires on Sn@CNT Nanocable: 3D electrodes for highly active electrocatalysts. *Chemistry* **2010**, *16* (3), 829–835 DOI: 10.1002/chem.200902320.

(64) LUO, Z.; LI, D.; TANG, H.; PAN, M.; RUAN, R. Degradation behavior of membrane–electrode-assembly materials in 10-cell PEMFC stack. *Int. J. Hydrogen Energy* **2006**, *31*

(13), 1831–1837 DOI: 10.1016/j.ijhydene.2006.02.029.

(65) Li, W.; Wang, X.; Chen, Z.; Waje, M.; Yan, Y. Pt-Ru supported on double-walled carbon nanotubes as high-performance anode catalysts for direct methanol fuel cells. *J. Phys. Chem. B* **2006**, *110* (31), 15353–15358 DOI: 10.1021/jp0623443.

(66) Dicks, A. L. The role of carbon in fuel cells. *J. Power Sources* **2006**, *156* (2), 128–141 DOI: 10.1016/j.jpowsour.2006.02.054.

(67) Wei, W.; Liang, H.; Parvez, K.; Zhuang, X.; Feng, X.; Müllen, K. Nitrogen-doped carbon nanosheets with size-defined mesopores as highly efficient metal-free catalyst for the oxygen reduction reaction. *Angew. Chemie - Int. Ed.* **2014**, *53* (6), 1570–1574 DOI: 10.1002/anie.201307319.

(68) Hoque, M. A.; Higgins, D. C.; Hassan, F. M.; Choi, J.-Y.; Pritzker, M. D.; Chen, Z. Tin oxide - mesoporous carbon composites as platinum catalyst supports for ethanol oxidation and oxygen reduction. *Electrochim. Acta* **2014**, *121*, 421–427 DOI: 10.1016/j.electacta.2013.12.075.

(69) Antolini, E. Carbon supports for low-temperature fuel cell catalysts. *Appl. Catal. B Environ.* **2009**, *88* (1–2), 1–24 DOI: 10.1016/j.apcatb.2008.09.030.

(70) Song, S.; Liang, Y.; Li, Z.; Wang, Y.; Fu, R.; Wu, D.; Tsiakaras, P. Effect of pore morphology of mesoporous carbons on the electrocatalytic activity of Pt nanoparticles for fuel cell reactions. *Appl. Catal. B Environ.* **2010**, *98* (3–4), 132–137 DOI: 10.1016/j.apcatb.2010.05.021.

(71) Kim, N. I.; Cheon, J. Y.; Kim, J. H.; Seong, J.; Park, J. Y.; Joo, S. H.; Kwon, K. Impact of

framework structure of ordered mesoporous carbons on the performance of supported Pt catalysts for oxygen reduction reaction. *Carbon N. Y.* **2014**, *72*, 354–364 DOI: 10.1016/j.carbon.2014.02.023.

(72) Ryoo, R.; Joo, S. H.; Jun, S. Synthesis of Highly Ordered Carbon Molecular Sieves via Template-Mediated Structural Transformation. *J. Phys. Chem. B* **1999**, *103* (37), 7743–7746 DOI: 10.1021/jp991673a.

(73) Salgado, J. R. C.; Alcaide, F.; Álvarez, G.; Calvillo, L.; Lázaro, M. J.; Pastor, E. Pt-Ru electrocatalysts supported on ordered mesoporous carbon for direct methanol fuel cell. *J. Power Sources* **2010**, *195* (13), 4022–4029 DOI: 10.1016/j.jpowsour.2010.01.001.

(74) Novoselov, K. S.; Geim, A. K.; Morozov, S. V.; Jiang, D.; Katsnelson, M. I.; Grigorieva, I. V.; Dubonos, S. V.; Firsov, A. A. Two-dimensional gas of massless Dirac fermions in graphene. *Nature* **2005**, *438* (7065), 197–200 DOI: 10.1038/nature04233.

(75) Guo, H.; Wang, X.-F.; Qian, Q.; Wang, F.; Xia, X. A Green Approach to the Synthesis of Graphene Nanosheets. *ACS Nano* **2009**, *3* (9), 2653–2659 DOI: 10.1021/nn900227d.

(76) Wang, Y.-J.; Wilkinson, D. P.; Zhang, J. Noncarbon support materials for polymer electrolyte membrane fuel cell electrocatalysts. *Chem. Rev.* **2011**, *111* (12), 7625–7651 DOI: 10.1021/cr100060r.

(77) Qu, L.; Liu, Y.; Baek, J.-B.; Dai, L. Nitrogen-Doped Graphene as Efficient Metal-Free Electrocatalyst for Oxygen Reduction in Fuel Cells. *ACS Nano* **2010**, *4* (3), 1321–1326 DOI: 10.1021/nn901850u.

(78) Lv, R.; Terrones, M. Towards new graphene materials: Doped graphene sheets and

nanoribbons. *Mater. Lett.* **2012**, *78*, 209–218 DOI: 10.1016/j.matlet.2012.04.033.

(79) Hummers, W. S.; Offeman, R. E. Preparation of Graphitic Oxide. *J. Am. Chem. Soc.* **1958**, *80* (6), 1339–1339 DOI: 10.1021/ja01539a017.

(80) Meng, L.; Fu, C.; Lu, Q. Advanced technology for functionalization of carbon nanotubes. *Prog. Nat. Sci.* **2009**, *19* (7), 801–810 DOI: 10.1016/j.pnsc.2008.08.011.

(81) Sun, S.; Zhang, G.; Zhong, Y.; Liu, H.; Li, R.; Zhou, X.; Sun, X. Ultrathin single crystal Pt nanowires grown on N-doped carbon nanotubes. *Chem. Commun.* **2009**, No. 45, 7048 DOI: 10.1039/b916080a.

(82) Chen, Z.; Chen, Z.; Higgins, D. Nitrogen doped carbon nanotubes and their impact on the oxygen reduction reaction in fuel cells. *Carbon N. Y.* **2010**, *48* (11), 3057–3065 DOI: 10.1016/j.carbon.2010.04.038.

(83) Wepasnick, K. A.; Smith, B. A.; Bitter, J. L.; Howard Fairbrother, D. Chemical and structural characterization of carbon nanotube surfaces. *Anal. Bioanal. Chem.* **2010**, *396* (3), 1003–1014 DOI: 10.1007/s00216-009-3332-5.

(84) VanBruinessen, A.; Karan, K. Development of Pt/CNT catalyst and transport-kinetic characterization of PEMFC catalyst layer. **2009**.

(85) Li, H.; Cheng, X.; Weng, F.-B.; Su, A.; Chiang, Y.-C. Nitrogen-Doped Carbon Nanotubes Prepared at Different Temperatures for Oxygen Reduction Reaction. *J. Electrochem. Soc.* **2014**, *161* (12), F1140–F1145 DOI: 10.1149/2.0171412jes.

(86) Mawhinney, D. B.; Naumenko, V.; Kuznetsova, A.; Yates, J. T.; Liu, J.; Smalley, R. E. Infrared Spectral Evidence for the Etching of Carbon Nanotubes: Ozone Oxidation at 298

K. *J. Am. Chem. Soc.* **2000**, *122* (10), 2383–2384 DOI: 10.1021/ja994094s.

(87) Ebbesen, T. W.; Hiura, H.; Bisher, M. E.; Treacy, M. M. J.; Shreeve-Keyer, J. L.; Haushalter, R. C. Decoration of carbon nanotubes. *Adv. Mater.* **1996**, *8*, 155–157 DOI: DOI 10.1002/adma.19960080212.

(88) Coloma, F.; Sepulveda-Escribano, A.; Fierro, J. L. G.; Rodriguez-Reinoso, F. Preparation of Platinum Supported on Pregraphitized Carbon Blacks. *Langmuir* **1994**, *10* (3), 750–755 DOI: 10.1021/la00015a025.

(89) Sa, Y. J.; Park, C.; Jeong, H. Y.; Park, S.-H.; Lee, Z.; Kim, K. T.; Park, G.-G.; Joo, S. H. Carbon Nanotubes/Heteroatom-Doped Carbon Core-Sheath Nanostructures as Highly Active, Metal-Free Oxygen Reduction Electrocatalysts for Alkaline Fuel Cells. *Angew. Chemie* **2014**, *126* (16), 4186–4190 DOI: 10.1002/ange.201307203.

(90) Guo, L.; Jiang, W. J.; Zhang, Y.; Hu, J. S.; Wei, Z. D.; Wan, L. J. Embedding Pt Nanocrystals in N-Doped Porous Carbon/Carbon Nanotubes toward Highly Stable Electrocatalysts for the Oxygen Reduction Reaction. *ACS Catal.* **2015**, *5* (5), 2903–2909 DOI: 10.1021/acscatal.5b00117.

(91) Chen, Y.; Wang, J.; Liu, H.; Li, R.; Sun, X.; Ye, S.; Knights, S. Enhanced stability of Pt electrocatalysts by nitrogen doping in CNTs for PEM fuel cells. *Electrochem. commun.* **2009**, *11* (10), 2071–2076 DOI: 10.1016/j.elecom.2009.09.008.

(92) Zhang, W.; Sherrell, P.; Minett, A. I.; Razal, J. M.; Chen, J. Carbon nanotube architectures as catalyst supports for proton exchange membrane fuel cells. *Energy Environ. Sci.* **2010**, *3* (9), 1286–1293 DOI: 10.1039/c0ee00139b.

(93) Higgins, D.; Hoque, M. A.; Seo, M. H.; Wang, R.; Hassan, F.; Choi, J. Y.; Pritzker, M.; Yu, A.; Zhang, J.; Chen, Z. Development and simulation of sulfur-doped graphene supported platinum with exemplary stability and activity towards oxygen reduction. *Adv. Funct. Mater.* **2014**, *24* (27), 4325–4336 DOI: 10.1002/adfm.201400161.

(94) Stamenkovic, V. R.; Fowler, B.; Mun, B. S.; Wang, G.; Ross, P. N.; Lucas, C. A.; Markovic, N. M. Improved Oxygen Reduction Activity on Pt3Ni(111) via Increased Surface Site Availability. *Science (80-.).* **2007**, *315* (5811), 493–497 DOI: 10.1126/science.1135941.

(95) Park, S.-A.; Kim, D.-S.; Kim, T.-J.; Kim, Y.-T. Strong Interaction between Pt and Thiolated Carbon for Electrocatalytic Durability Enhancement. *ACS Catal.* **2013**, *3* (12), 3067–3074 DOI: 10.1021/cs400649n.

(96) Perini, L.; Durante, C.; Favaro, M.; Perazzolo, V.; Agnoli, S.; Schneider, O.; Granozzi, G.; Gennaro, A. Metal-support interaction in platinum and palladium nanoparticles loaded on nitrogen-doped mesoporous carbon for oxygen reduction reaction. *ACS Appl. Mater. Interfaces* **2015**, *7* (2), 1170–1179 DOI: 10.1021/am506916y.

(97) Kumar, A.; Ramani, V. Strong Metal–Support Interactions Enhance the Activity and Durability of Platinum Supported on Tantalum-Modified Titanium Dioxide Electrocatalysts. *ACS Catal.* **2014**, *4* (5), 1516–1525 DOI: 10.1021/cs500116h.

(98) Yu, X.; Ye, S. Recent advances in activity and durability enhancement of Pt/C catalytic cathode in PEMFC. Part I. Physico-chemical and electronic interaction between Pt and carbon support, and activity enhancement of Pt/C catalyst. *J. Power Sources* **2007**, *172* (1), 133–144 DOI: 10.1016/j.jpowsour.2007.07.049.

(99) Ma, J.; Habrioux, A.; Luo, Y.; Ramos-Sanchez, G.; Calvillo, L.; Granozzi, G.; Balbuena, P. B.; Alonso-Vante, N. Electronic interaction between platinum nanoparticles and nitrogen-doped reduced graphene oxide: Effect on the oxygen reduction reaction. *J. Mater. Chem. A* **2015**, *3* (22), 11891–11904 DOI: 10.1039/c5ta01285f.

(100) KIM, Y.; MITANI, T. Surface thiolation of carbon nanotubes as supports: A promising route for the high dispersion of Pt nanoparticles for electrocatalysts. *J. Catal.* **2006**, *238* (2), 394–401 DOI: 10.1016/j.jcat.2005.12.020.

(101) Denis, P. A.; Faccio, R.; Mombru, A. W. Is it possible to dope single-walled carbon nanotubes and graphene with sulfur? *Chemphyschem* **2009**, *10* (4), 715–722 DOI: 10.1002/cphc.200800592.

(102) Kwak, J. H.; Hu, J.; Mei, D.; Yi, C.-W.; Kim, D. H.; Peden, C. H. F.; Allard, L. F.; Szanyi, J. Coordinatively Unsaturated Al3+ Centers as Binding Sites for Active Catalyst Phases of Platinum on -Al2O3. *Science (80-.).* **2009**, *325* (5948), 1670–1673 DOI: 10.1126/science.1176745.

(103) Liu, H.; Liu, Y.; Zhu, D. Chemical doping of graphene. *J. Mater. Chem.* **2011**, *21* (10), 3335–3345 DOI: 10.1039/C0JM02922J.

(104) Liu, R.; Wu, D.; Feng, X.; Müllen, K. Nitrogen-doped ordered mesoporous graphitic arrays with high electrocatalytic activity for oxygen reduction. *Angew. Chemie - Int. Ed.* **2010**, *49* (14), 2565–2569 DOI: 10.1002/anie.200907289.

(105) Sheng, Z. H.; Shao, L.; Chen, J. J.; Bao, W. J.; Wang, F. Bin; Xia, X. H. Catalyst-free synthesis of nitrogen-doped graphene via thermal annealing graphite oxide with melamine

and its excellent electrocatalysis. *ACS Nano* **2011**, *5* (6), 4350–4358 DOI: 10.1021/nn103584t.

(106) Vinayan, B. P.; Nagar, R.; Rajalakshmi, N.; Ramaprabhu, S. Novel Platinum-Cobalt Alloy Nanoparticles Dispersed on Nitrogen-Doped Graphene as a Cathode Electrocatalyst for PEMFC Applications. *Adv. Funct. Mater.* **2012**, *22* (16), 3519–3526 DOI: 10.1002/adfm.201102544.

(107) Paraknowitsch, J. P.; Thomas, A.; Schmidt, J. Microporous sulfur-doped carbon from thienyl-based polymer network precursors. *Chem. Commun. (Camb).* **2011**, *47* (29), 8283–8285 DOI: 10.1039/c1cc12272j.

(108) Higgins, D.; Hoque, M. A.; Seo, M. H.; Wang, R.; Hassan, F.; Choi, J.-Y.; Pritzker, M.; Yu, A.; Zhang, J.; Chen, Z. Development and Simulation of Sulfur-doped Graphene Supported Platinum with Exemplary Stability and Activity Towards Oxygen Reduction. *Adv. Funct. Mater.* **2014**, *24* (27), 4325–4336 DOI: 10.1002/adfm.201400161.

(109) Higgins, D. C.; Choi, J.-Y.; Wu, J.; Lopez, A.; Chen, Z. Titanium nitride–carbon nanotube core–shell composites as effective electrocatalyst supports for low temperature fuel cells. *J. Mater. Chem.* **2012**, *22* (9), 3727 DOI: 10.1039/c2jm15014j.

(110) Goldstein, J. I.; Newbury, D. E.; Echlin, P.; Joy, D. C.; Lyman, C. E.; Lifshin, E.; Sawyer, L.; Michael, J. R. *Scanning Electron Microscopy and X-ray Microanalysis*; Springer US: Boston, MA, 2003.

(111) Seiler, H. Secondary electron emission in the scanning electron microscope. *J. Appl. Phys.* **1983**, *54* (11), R1–R18 DOI: 10.1063/1.332840.

(112) Williams, D. B.; Carter, C. B. *Transmission Electron Microscopy*; Springer US: Boston, MA, 2009.

(113) Alnot, P.; Olivier, J.; Wyczisk, F.; Fadley, C. S. Angle-resolved X-Ray photoelectron spectroscopy for the characterization of GaAs(OO1) surfaces. *J. Electron Spectros. Relat. Phenomena* **1987**, *43* (3), 263–286 DOI: 10.1016/0368-2048(87)80006-3.

(114) Brunauer, S.; Emmett, P. H.; Teller, E. Adsorption of Gases in Multimolecular Layers. *J. Am. Chem. Soc.* **1938**, *60* (2), 309–319 DOI: 10.1021/ja01269a023.

(115) Schmickler, W.; Santos, E. Experimental techniques for electrode kinetics – non-stationary methods. In *Interfacial Electrochemistry*; Springer Berlin Heidelberg: Berlin, Heidelberg, 2010; pp 235–257.

(116) John W. Weidner, Vijay A. Sethuraman, and J. W. V. Z. Engineering a Membrane Electrode Assembly. *Electrochem. Soc. Interface* **2003**, 41–47.

(117) Rossmeisl, J.; Karlberg, G. S.; Jaramillo, T.; Nørskov, J. K. Steady state oxygen reduction and cyclic voltammetry. *Faraday Discuss.* **2008**, *140*, 337–346; discussion 417-37.

(118) Tang, W.; Henkelman, G. Charge redistribution in core-shell nanoparticles to promote oxygen reduction. *J. Chem. Phys.* **2009**, *130* (19), 194504 DOI: 10.1063/1.3134684.

(119) Sasaki, K.; Naohara, H.; Cai, Y.; Choi, Y. M.; Liu, P.; Vukmirovic, M. B.; Wang, J. X.; Adzic, R. R. Core-protected platinum monolayer shell high-stability electrocatalysts for fuel-cell cathodes. *Angew. Chem. Int. Ed. Engl.* **2010**, *49* (46), 8602–8607 DOI: 10.1002/anie.201004287.

(120) Chen, Z.; Waje, M.; Li, W.; Yan, Y. Supportless Pt and PtPd nanotubes as electrocatalysts

for oxygen-reduction reactions. *Angew. Chem. Int. Ed. Engl.* **2007**, *46* (22), 4060–4063 DOI: 10.1002/anie.200700894.

(121) Koenigsmann, C.; Santulli, A. C.; Gong, K.; Vukmirovic, M. B.; Zhou, W. P.; Sutter, E.; Wong, S. S.; Adzic, R. R. Enhanced electrocatalytic performance of processed, ultrathin, supported Pd-Pt core-shell nanowire catalysts for the oxygen reduction reaction. *J. Am. Chem. Soc.* **2011**, *133* (25), 9783–9795 DOI: 10.1021/ja111130t.

(122) Xia, B. Y.; Ng, W. T.; Wu, H. Bin; Wang, X.; Lou, X. W. D. Self-supported interconnected Pt nanoassemblies as highly stable electrocatalysts for low-temperature fuel cells. *Angew. Chem. Int. Ed. Engl.* **2012**, *51* (29), 7213–7216 DOI: 10.1002/anie.201201553.

(123) Porter, N. S.; Wu, H.; Quan, Z.; Fang, J. Shape-control and electrocatalytic activity-enhancement of Pt-based bimetallic nanocrystals. *Acc. Chem. Res.* **2013**, *46* (8), 1867–1877 DOI: 10.1021/ar3002238.

(124) Guo, S.; Zhang, S.; Su, D.; Sun, S. Seed-Mediated Synthesis of Core / Shell FePtM / FePt (M = Pd , Au) Nanowires and Their Electrocatalysis for Oxygen Reduction Reaction. **2013**.

(125) Wang, R.; Higgins, D. C.; Hoque, M. A.; Lee, D.; Hassan, F.; Chen, Z. Controlled Growth of Platinum Nanowire Arrays on Sulfur Doped Graphene as High Performance Electrocatalyst. *Sci. Rep.* **2013**, *3*, 1–7 DOI: 10.1038/srep02431.

(126) Sun, S.; Zhang, G.; Geng, D.; Chen, Y.; Li, R.; Cai, M.; Sun, X. A highly durable platinum nanocatalyst for proton exchange membrane fuel cells: Multiarmed starlike nanowire single crystal. *Angew. Chemie - Int. Ed.* **2011**, *50* (2), 422–426 DOI: 10.1002/anie.201004631.

(127) Zhou, Y.; Neyerlin, K.; Olson, T. S.; Pylypenko, S.; Bult, J.; Dinh, H. N.; Gennett, T.; Shao,

Z.; O'Hayre, R. Enhancement of Pt and Pt-alloy fuel cell catalyst activity and durability via nitrogen-modified carbon supports. *Energy Environ. Sci.* **2010**, *3* (10), 1437 DOI: 10.1039/c003710a.

(128) Shao, Y.; Sui, J.; Yin, G.; Gao, Y. Nitrogen-doped carbon nanostructures and their composites as catalytic materials for proton exchange membrane fuel cell. *Appl. Catal. B Environ.* **2008**, *79* (1), 89–99 DOI: 10.1016/j.apcatb.2007.09.047.

(129) Zhang, L.; Zhu, S.; Chang, Q.; Su, D.; Yue, J.; Du, Z.; Shao, M. Palladium–Platinum Core–Shell Electrocatalysts for Oxygen Reduction Reaction Prepared with the Assistance of Citric Acid. *ACS Catal.* **2016**, *6* (6), 3428–3432 DOI: 10.1021/acscatal.6b00517.

(130) Wang, D.; Yu, Y.; Zhu, J.; Liu, S.; Muller, D. A.; Abruña, H. D. Morphology and activity tuning of Cu_3Pt/C ordered intermetallic nanoparticles by selective electrochemical dealloying. *Nano Lett.* **2015**, *15* (2), 1343–1348 DOI: 10.1021/nl504597j.

(131) Wang, X.; Choi, S.-I.; Roling, L. T.; Luo, M.; Ma, C.; Zhang, L.; Chi, M.; Liu, J.; Xie, Z.; Herron, J. a.; et al. Palladium–platinum core-shell icosahedra with substantially enhanced activity and durability towards oxygen reduction. *Nat. Commun.* **2015**, *6* (May), 7594 DOI: 10.1038/ncomms8594.

(132) Mullin, J. W. Crystal growth. In *Crystallization*; Elsevier, 2001; pp 216–288.

(133) Fievet, F.; Lagier, J. P.; Figlarz, M. Preparing Monodisperse Metal Powders in Micrometer and Submicrometer Sizes by the Polyol Process. *MRS Bull.* **1989**, *14* (12), 29–34 DOI: 10.1557/S0883769400060930.

(134) Xiong, Y.; Xia, Y. Shape-controlled synthesis of metal nanostructures: The case of

palladium. *Adv. Mater.* **2007**, *19* (20), 3385–3391 DOI: 10.1002/adma.200701301.

(135) Hoque, M. A.; Hassan, F. M.; Higgins, D.; Choi, J.-Y.; Pritzker, M.; Knights, S.; Ye, S.; Chen, Z. Multigrain platinum nanowires consisting of oriented nanoparticles anchored on sulfur-doped graphene as a highly active and durable oxygen reduction electrocatalyst. *Adv. Mater.* **2015**, *27* (7), 1229–1234 DOI: 10.1002/adma.201404426.

(136) Herrmann, I.; Kramm, U. I.; Radnik, J.; Fiechter, S.; Bogdanoff, P. Influence of Sulfur on the Pyrolysis of CoTMPP as Electrocatalyst for the Oxygen Reduction Reaction. *J. Electrochem. Soc.* **2009**, *156* (10), B1283 DOI: 10.1149/1.3185852.

(137) Yang, S.; Zhi, L.; Tang, K.; Feng, X.; Maier, J.; Müllen, K. Efficient Synthesis of Heteroatom (N or S)-Doped Graphene Based on Ultrathin Graphene Oxide-Porous Silica Sheets for Oxygen Reduction Reactions. *Adv. Funct. Mater.* **2012**, *22* (17), 3634–3640 DOI: 10.1002/adfm.201200186.

(138) Shrestha, S.; Liu, Y.; Mustain, W. E. Electrocatalytic Activity and Stability of Pt clusters on State-of-the-Art Supports: A Review. *Catal. Rev. Sci. Eng.* **2011**, *53* (1), 256–336 DOI: 10.1080/01614940.2011.596430.

(139) Yang, X. H.; Guo, J. W.; Yang, S.; Hou, Y.; Zhang, B.; Yang, H. G. A free radical assisted strategy for preparing ultra-small Pt decorated CNTs as a highly efficient counter electrode for dye-sensitized solar cells. *J. Mater. Chem. A* **2014**, *2* (3), 614–619 DOI: 10.1039/C3TA13986G.

(140) Best, S. A.; Brant, P.; Feltham, R. D.; Rauchfuss, T. B.; Roundhill, D. M.; Walton, R. A. X-ray photoelectron spectra of inorganic molecules. 18. Observations on sulfur 2p binding

energies in transition metal complexes of sulfur-containing ligands. *Inorg. Chem.* **1977**, *16* (8), 1976–1979 DOI: 10.1021/ic50174a030.

(141) Travlou, N. A.; Kyzas, G. Z.; Lazaridis, N. K.; Deliyanni, E. A. Functionalization of graphite oxide with magnetic chitosan for the preparation of a nanocomposite dye adsorbent. *Langmuir* **2013**, *29* (5), 1657–1668 DOI: 10.1021/la304696y.

(142) Okpalugo, T. I. T.; Papakonstantinou, P.; Murphy, H.; McLaughlin, J.; Brown, N. M. D. High resolution XPS characterization of chemical functionalised MWCNTs and SWCNTs. *Carbon N. Y.* **2005**, *43* (1), 153–161 DOI: 10.1016/j.carbon.2004.08.033.

(143) Barrie, A.; Drummond, I. W.; Herd, Q. C. Correlation of calculated and measured 2p spin-orbit splitting by electron spectroscopy using monochromatic x-radiation. *J. Electron Spectros. Relat. Phenomena* **1974**, *5* (1), 217–225 DOI: 10.1016/0368-2048(74)85013-9.

(144) Choi, C. H.; Park, S. H.; Woo, S. I. Heteroatom doped carbons prepared by the pyrolysis of bio-derived amino acids as highly active catalysts for oxygen electro-reduction reactions. *Green Chem.* **2011**, *13* (2), 406–412 DOI: 10.1039/C0GC00384K.

(145) Liu, Z.; Nie, H.; Yang, Z.; Zhang, J.; Jin, Z.; Lu, Y.; Xiao, Z.; Huang, S. Sulfur-nitrogen co-doped three-dimensional carbon foams with hierarchical pore structures as efficient metal-free electrocatalysts for oxygen reduction reactions. *Nanoscale* **2013**, *5* (8), 3283–3288 DOI: 10.1039/c3nr34003a.

(146) Qiao, B.; Liang, J.-X.; Wang, A.; Xu, C.-Q.; Li, J.; Zhang, T.; Liu, J. J. Ultrastable single-atom gold catalysts with strong covalent metal-support interaction (CMSI). *Nano Res.* **2015**, *8* (9), 2913–2924 DOI: 10.1007/s12274-015-0796-9.

(147) Labib, M. E.; Thomas, J. H.; Embert, D. D. The effect of heat treatment on sulfur in an electrically-conductive carbon black. *Carbon N. Y.* **1984**, *22* (4–5), 445–451 DOI: 10.1016/0008-6223(84)90018-6.

(148) Chang, Y.; Hong, F.; He, C.; Zhang, Q.; Liu, J. Nitrogen and sulfur dual-doped non-noble catalyst using fluidic acrylonitrile telomer as precursor for efficient oxygen reduction. *Adv. Mater.* **2013**, *25* (34), 4794–4799 DOI: 10.1002/adma.201301002.

(149) Shao-Horn, Y.; Sheng, W. C.; Chen, S.; Ferreira, P. J.; Holby, E. F.; Morgan, D. Instability of Supported Platinum Nanoparticles in Low-Temperature Fuel Cells. *Top. Catal.* **2007**, *46* (3–4), 285–305 DOI: 10.1007/s11244-007-9000-0.

(150) Gasteiger, H. A.; Kocha, S. S.; Sompalli, B.; Wagner, F. T. Activity benchmarks and requirements for Pt, Pt-alloy, and non-Pt oxygen reduction catalysts for PEMFCs. *Appl. Catal. B Environ.* **2005**, *56* (1-2 SPEC. ISS.), 9–35 DOI: 10.1016/j.apcatb.2004.06.021.

(151) Ferreira, P. J.; la O', G. J.; Shao-Horn, Y.; Morgan, D.; Makharia, R.; Kocha, S.; Gasteiger, H. A. Instability of Pt/C Electrocatalysts in Proton Exchange Membrane Fuel Cells. *J. Electrochem. Soc.* **2005**, *152* (11), A2256 DOI: 10.1149/1.2050347.

(152) Fu, J.; Hou, M.; Du, C.; Shao, Z.; Yi, B. Potential dependence of sulfur dioxide poisoning and oxidation at the cathode of proton exchange membrane fuel cells. *J. Power Sources* **2009**, *187* (1), 32–38 DOI: 10.1016/j.jpowsour.2008.10.103.

(153) van der Vliet, D. F.; Wang, C.; Tripkovic, D.; Strmcnik, D.; Zhang, X. F.; Debe, M. K.; Atanasoski, R. T.; Markovic, N. M.; Stamenkovic, V. R. Mesostructured thin films as electrocatalysts with tunable composition and surface morphology. *Nat. Mater.* **2012**, *11*

(12), 1051–1058 DOI: 10.1038/nmat3457.

(154) Markovic, N. Kinetics of Oxygen Reduction on Pt(hkl) Electrodes: Implications for the Crystallite Size Effect with Supported Pt Electrocatalysts. *J. Electrochem. Soc.* **1997**, *144* (5), 1591 DOI: 10.1149/1.1837646.

(155) Zhang, J.; Vukmirovic, M. B.; Xu, Y.; Mavrikakis, M.; Adzic, R. R. Controlling the catalytic activity of platinum-monolayer electrocatalysts for oxygen reduction with different substrates. *Angew. Chemie - Int. Ed.* **2005**, *44* (14), 2132–2135 DOI: 10.1002/anie.200462335.

(156) Vukmirovic, M. B.; Zhang, J.; Sasaki, K.; Nilekar, A. U.; Uribe, F.; Mavrikakis, M.; Adzic, R. R. Platinum monolayer electrocatalysts for oxygen reduction. *Electrochim. Acta* **2007**, *52* (6), 2257–2263 DOI: 10.1016/j.electacta.2006.05.062.

(157) Wang, J. X.; Zhang, J.; Adzic, R. R. Double-trap kinetic equation for the oxygen reduction reaction on Pt(111) in acidic media. *J. Phys. Chem. A* **2007**, *111* (49), 12702–12710 DOI: 10.1021/jp076104e.

(158) Nilekar, A. U.; Mavrikakis, M. Improved oxygen reduction reactivity of platinum monolayers on transition metal surfaces. *Surf. Sci.* **2008**, *602* (14), L89–L94 DOI: 10.1016/j.susc.2008.05.036.

(159) Hu, P.; Huang, Z.; Amghouz, Z.; Makkee, M.; Xu, F.; Kapteijn, F.; Dikhtiarenko, A.; Chen, Y.; Gu, X.; Tang, X. Electronic metal-support interactions in single-atom catalysts. *Angew. Chemie - Int. Ed.* **2014**, *53* (13), 3418–3421 DOI: 10.1002/anie.201309248.

(160) Stamenkovic, V.; Mun, B. S.; Mayrhofer, K. J. J.; Ross, P. N.; Markovic, N. M.; Rossmeisl,

J.; Greeley, J.; Nørskov, J. K. Changing the Activity of Electrocatalysts for Oxygen Reduction by Tuning the Surface Electronic Structure. *Angew. Chemie Int. Ed.* **2006**, *45* (18), 2897–2901 DOI: 10.1002/anie.200504386.

(161) Stamenkovic, V. R.; Mun, B. S.; Arenz, M.; Mayrhofer, K. J. J.; Lucas, C. A.; Wang, G.; Ross, P. N.; Markovic, N. M. Trends in electrocatalysis on extended and nanoscale Pt-bimetallic alloy surfaces. *Nat. Mater.* **2007**, *6* (3), 241–247 DOI: 10.1038/nmat1840.

(162) Greeley, J.; Stephens, I. E. L.; Bondarenko, A. S.; Johansson, T. P.; Hansen, H. A.; Jaramillo, T. F.; Rossmeisl, J.; Chorkendorff, I.; Nørskov, J. K. Alloys of platinum and early transition metals as oxygen reduction electrocatalysts. *Nat. Chem.* **2009**, *1* (7), 552–556 DOI: 10.1038/nchem.367.

(163) Hu, J.; Wu, L.; Kuttiyiel, K. A.; Goodman, K. R.; Zhang, C.; Zhu, Y.; Vukmirovic, M. B.; White, M. G.; Sasaki, K.; Adzic, R. R. Increasing Stability and Activity of Core-Shell Catalysts by Preferential Segregation of Oxide on Edges and Vertexes: Oxygen Reduction on Ti-Au@Pt/C. *J. Am. Chem. Soc.* **2016**, *138* (29), 9294–9300 DOI: 10.1021/jacs.6b04999.

(164) Newman, R.; Corcoran, S.; Erlebacher, J.; Aziz, M. J.; Sieradzki, K. Alloy Corrosion. *MRS Bull.* **1999**, *24* (07), 24–28 DOI: 10.1557/S0883769400052660.

(165) Kulkarni, A.; Siahrostami, S.; Patel, A.; Nørskov, J. K. Understanding Catalytic Activity Trends in the Oxygen Reduction Reaction. *Chem. Rev.* **2018**, *118* (5), 2302–2312 DOI: 10.1021/acs.chemrev.7b00488.

(166) Chu, S.; Cui, Y.; Liu, N. The path towards sustainable energy. *Nat. Mater.* **2017**, *16* (1), 16–22 DOI: 10.1038/nmat4834.

(167) Seh, Z. W.; Kibsgaard, J.; Dickens, C. F.; Chorkendorff, I.; Nørskov, J. K.; Jaramillo, T. F. Combining theory and experiment in electrocatalysis: Insights into materials design. *Science* **2017**, *355* (6321) DOI: 10.1126/science.aad4998.

(168) Brankovic, S. R.; Wang, J. X.; Adžić, R. R. Metal monolayer deposition by replacement of metal adlayers on electrode surfaces. *Surf. Sci.* **2001**, *474* (1–3), L173–L179 DOI: 10.1016/S0039-6028(00)01103-1.

(169) Zhang, J.; Lima, F. H. B.; Shao, M. H.; Sasaki, K.; Wang, J. X.; Hanson, J.; Adzic, R. R. Platinum monolayer on nonnoble metal-noble metal core-shell nanoparticle electrocatalysts for O2 reduction. *J. Phys. Chem. B* **2005**, *109* (48), 22701–22704 DOI: 10.1021/jp055634c.

(170) Esposito, D. V.; Hunt, S. T.; Stottlemyer, A. L.; Dobson, K. D.; McCandless, B. E.; Birkmire, R. W.; Chen, J. G. Low-cost hydrogen-evolution catalysts based on monolayer platinum on tungsten monocarbide substrates. *Angew. Chem. Int. Ed. Engl.* **2010**, *49* (51), 9859–9862 DOI: 10.1002/anie.201004718.

(171) Fukamori, Y.; König, M.; Yoon, B.; Wang, B.; Esch, F.; Heiz, U.; Landman, U. Fundamental Insight into the Substrate-Dependent Ripening of Monodisperse Clusters. *ChemCatChem* **2013**, *5* (11), 3330–3341 DOI: 10.1002/cctc.201300250.

(172) Reitz, W. Handbook of Fuel Cells: Fundamentals, Technology, and Applications , (Volume 2) W. Vielstich, A. Lamm, and H. A. Gasteiger (editors). *Mater. Manuf. Process.* **2007**, *22* (6), 789–789 DOI: 10.1080/10426910701416336.

(173) Campbell, C. T.; Sellers, J. R. V. Anchored metal nanoparticles: Effects of support and size on their energy, sintering resistance and reactivity. *Faraday Discuss.* **2013**, *162*, 9–30 DOI:

10.1039/c3fd00094j.

(174) Debe, M. K. Electrocatalyst approaches and challenges for automotive fuel cells. *Nature* **2012**, *486* (7401), 43–51 DOI: 10.1038/nature11115.

(175) Hoque, M. A.; Hassan, F. M.; Jauhar, A. M.; Jiang, G.; Pritzker, M.; Choi, J.-Y.; Knights, S.; Ye, S.; Chen, Z. Web-like 3D Architecture of Pt Nanowires and Sulfur-Doped Carbon Nanotube with Superior Electrocatalytic Performance. *ACS Sustain. Chem. Eng.* **2018**, *6* (1), 93–98 DOI: 10.1021/acssuschemeng.7b03580.

(176) Higgins, D. C.; Ye, S.; Knights, S.; Chen, Z. Highly Durable Platinum-Cobalt Nanowires by Microwave Irradiation as Oxygen Reduction Catalyst for PEM Fuel Cell. *Electrochem. Solid-State Lett.* **2012**, *15* (6), B83 DOI: 10.1149/2.018206esl.

(177) Higgins, D. C.; Hoque, M. A.; Hassan, F.; Choi, J. Y.; Kim, B.; Chen, Z. Oxygen reduction on graphene-carbon nanotube composites doped sequentially with nitrogen and sulfur. *ACS Catal.* **2014**, *4* (8), 2734–2740 DOI: 10.1021/cs5003806.

(178) Yano, H.; Watanabe, M.; Iiyama, A.; Uchida, H. Particle-size effect of Pt cathode catalysts on durability in fuel cells. *Nano Energy* **2016**, *29*, 323–333 DOI: 10.1016/j.nanoen.2016.02.016.

(179) Farmer, J. A.; Campbell, C. T. Ceria Maintains Smaller Metal Catalyst Particles by Strong Metal-Support Bonding. *Science (80-.).* **2010**, *329* (5994), 933–936 DOI: 10.1126/science.1191778.

(180) Xiong, Y.; McLellan, J. M.; Chen, J.; Yin, Y.; Li, Z.; Xia, Y. Kinetically Controlled Synthesis of Triangular and Hexagonal Nanoplates of Palladium and Their SPR/SERS

Properties. *J. Am. Chem. Soc.* **2005**, *127* (48), 17118–17127 DOI: 10.1021/ja056498s.

(181) Tursun, H.; Liu, R.; Li, J.; Abro, R.; Wang, X.; Gao, Y.; Li, Y. Carbon Material Optimized Biocathode for Improving Microbial Fuel Cell Performance. *Front. Microbiol.* **2016**, *7* (JAN), 1–9 DOI: 10.3389/fmicb.2016.00006.

(182) Yu, P. T.; Gu, W.; Zhang, J.; Makharia, R.; Wagner, F. T.; Gasteiger, H. A. Carbon-Support Requirements for Highly Durable Fuel Cell Operation. In *Polymer Electrolyte Fuel Cell Durability*; Springer New York: New York, NY, 2009; pp 29–53.

(183) Xia, B. Y.; Wang, J. N.; Teng, S. J.; Wang, X. X. Durability Improvement of a Pt Catalyst with the Use of a Graphitic Carbon Support. *Chem. - A Eur. J.* **2010**, *16* (28), 8268–8274 DOI: 10.1002/chem.201000758.

(184) Aijaz, A.; Karkamkar, A.; Choi, Y. J.; Tsumori, N.; Rönnebro, E.; Autrey, T.; Shioyama, H.; Xu, Q. Immobilizing highly catalytically active Pt nanoparticles inside the pores of metal-organic framework: a double solvents approach. *J. Am. Chem. Soc.* **2012**, *134* (34), 13926–13929 DOI: 10.1021/ja3043905.

(185) Romanchenko, A.; Likhatski, M.; Mikhlin, Y. X-ray Photoelectron Spectroscopy (XPS) Study of the Products Formed on Sulfide Minerals Upon the Interaction with Aqueous Platinum (IV) Chloride Complexes. *Minerals* **2018**, *8* (12), 578 DOI: 10.3390/min8120578.

(186) Lewera, A.; Timperman, L.; Roguska, A.; Alonso-Vante, N. Metal–Support Interactions between Nanosized Pt and Metal Oxides (WO 3 and TiO 2) Studied Using X-ray Photoelectron Spectroscopy. *J. Phys. Chem. C* **2011**, *115* (41), 20153–20159 DOI: 10.1021/jp2068446.

(187) Aricò, A. S.; Shukla, A. K.; Kim, H.; Park, S.; Min, M.; Antonucci, V. XPS study on oxidation states of Pt and its alloys with Co and Cr and its relevance to electroreduction of oxygen. *Appl. Surf. Sci.* **2001**, *172* (1–2), 33–40 DOI: 10.1016/S0169-4332(00)00831-X.

(188) Ho, V. T. T.; Pan, C.-J.; Rick, J.; Su, W.-N.; Hwang, B.-J. Nanostructured Ti 0.7 Mo 0.3 O 2 Support Enhances Electron Transfer to Pt: High-Performance Catalyst for Oxygen Reduction Reaction. *J. Am. Chem. Soc.* **2011**, *133* (30), 11716–11724 DOI: 10.1021/ja2039562.

(189) Debe, M. K. Electrocatalyst approaches and challenges for automotive fuel cells. *Nature* **2012**, *486* (7401), 43–51 DOI: 10.1038/nature11115.

(190) Sui, S.; Wang, X.; Zhou, X.; Su, Y.; Riffat, S.; Liu, C. A comprehensive review of Pt electrocatalysts for the oxygen reduction reaction: Nanostructure, activity, mechanism and carbon support in PEM fuel cells. *J. Mater. Chem. A* **2017**, *5* (5), 1808–1825 DOI: 10.1039/C6TA08580F.

(191) Shao, M.; Peles, A.; Shoemaker, K. Electrocatalysis on platinum nanoparticles: Particle size effect on oxygen reduction reaction activity. *Nano Lett.* **2011**, *11* (9), 3714–3719 DOI: 10.1021/nl2017459.

(192) Ahluwalia, R. K.; Arisetty, S.; Peng, J.-K.; Subbaraman, R.; Wang, X.; Kariuki, N.; Myers, D. J.; Mukundan, R.; Borup, R.; Polevaya, O. Dynamics of Particle Growth and Electrochemical Surface Area Loss due to Platinum Dissolution. *J. Electrochem. Soc.* **2014**, *161* (3), F291–F304 DOI: 10.1149/2.051403jes.

(193) Mezzavilla, S.; Baldizzone, C.; Swertz, A. C.; Hodnik, N.; Pizzutilo, E.; Polymeros, G.;

Keeley, G. P.; Knossalla, J.; Heggen, M.; Mayrhofer, K. J. J.; et al. Structure-Activity-Stability Relationships for Space-Confined PtxNiy Nanoparticles in the Oxygen Reduction Reaction. *ACS Catal.* **2016**, *6* (12), 8058–8068 DOI: 10.1021/acscatal.6b02221.

(194) Zhang, C.; Xu, L.; Shan, N.; Sun, T.; Chen, J.; Yan, Y. Enhanced Electrocatalytic Activity and Durability of Pt Particles Supported on Ordered Mesoporous Carbon Spheres. *ACS Catal.* **2014**, *4* (6), 1926–1930 DOI: 10.1021/cs500107t.

(195) Wang, J.; Yin, G.; Liu, H.; Li, R.; Flemming, R. L.; Sun, X. Carbon nanotubes supported Pt–Au catalysts for methanol-tolerant oxygen reduction reaction: A comparison between Pt/Au and PtAu nanoparticles. *J. Power Sources* **2009**, *194* (2), 668–673 DOI: 10.1016/j.jpowsour.2009.06.040.

(196) Dai, L.; Xue, Y.; Qu, L.; Choi, H.-J.; Baek, J.-B. Metal-Free Catalysts for Oxygen Reduction Reaction. *Chem. Rev.* **2015**, *115* (11), 4823–4892 DOI: 10.1021/cr5003563.

(197) Yu, D.; Nagelli, E.; Du, F.; Dai, L. Metal-Free Carbon Nanomaterials Become More Active than Metal Catalysts and Last Longer. *J. Phys. Chem. Lett.* **2010**, *1* (14), 2165–2173 DOI: 10.1021/jz100533t.

(198) Geng, D.; Hu, Y.; Li, Y.; Li, R.; Sun, X. One-pot solvothermal synthesis of doped graphene with the designed nitrogen type used as a Pt support for fuel cells. *Electrochem. commun.* **2012**, *22* (1), 65–68 DOI: 10.1016/j.elecom.2012.05.033.

(199) Sahoo, M.; Ramaprabhu, S. Nitrogen and sulfur co-doped porous carbon – is an efficient electrocatalyst as platinum or a hoax for oxygen reduction reaction in acidic environment PEM fuel cell? *Energy* **2017**, *119*, 1075–1083 DOI: 10.1016/j.energy.2016.11.066.

(200) Jauhar, A. M.; Hassan, F. M.; Cano, Z. P.; Hoque, M. A.; Chen, Z. Platinum-Palladium Core-Shell Nanoflower Catalyst with Improved Activity and Excellent Durability for the Oxygen Reduction Reaction. *Adv. Mater. Interfaces* **2018**, *5* (7), 1701508 DOI: 10.1002/admi.201701508.

(201) Liang, J.; Jiao, Y.; Jaroniec, M.; Qiao, S. Z. Sulfur and nitrogen dual-doped mesoporous graphene electrocatalyst for oxygen reduction with synergistically enhanced performance. *Angew. Chem. Int. Ed. Engl.* **2012**, *51* (46), 11496–11500 DOI: 10.1002/anie.201206720.

(202) Kiciński, W.; Szala, M.; Bystrzejewski, M. Sulfur-doped porous carbons: Synthesis and applications. *Carbon N. Y.* **2014**, *68*, 1–32 DOI: 10.1016/j.carbon.2013.11.004.

(203) Garlyyev, B.; Kratzl, K.; Rück, M.; Michalička, J.; Fichtner, J.; Macak, J. M.; Kratky, T.; Günther, S.; Cokoja, M.; Bandarenka, A. S.; et al. Optimizing the Size of Platinum Nanoparticles for Enhanced Mass Activity in the Electrochemical Oxygen Reduction Reaction. *Angew. Chemie Int. Ed.* **2019**, *58* (28), 9596–9600 DOI: 10.1002/anie.201904492.

(204) Litster, S.; McLean, G. PEM fuel cell electrodes. *J. Power Sources* **2004**, *130* (1–2), 61–76 DOI: 10.1016/j.jpowsour.2003.12.055.